Chip production rate and tool wear estimation

in micro-endmilling

by

Jue-Hyun Lee

A Dissertation Presented in Partial Fulfillment
Of the Requirements for the Degree
Doctor of Philosophy

Approved April 2019 by the
Graduate Supervisory Committee

Angela A. Sodemann, Chair
Abdelrahman Shuaib
Keng Hsu
Panagiotis Artemiadis
Yongming Liu

ARIZONA STATE UNIVERSITY

May 2019

ABSTRACT

In this research, a new cutting edge wear estimator for micro-endmilling is developed and the reliabillity of the estimator is evaluated. The main concept of this estimator is the minimum chip thickness effect. This estimator predicts the cutting edge radius by detecting the drop in the chip production rate as the cutting edge of a micro-endmill slips over the workpiece when the minimum chip thickness becomes larger than the uncut chip thickness, thus transitioning from the shearing to the ploughing dominant regime. The chip production rate is investigated through simulation and experiment. The simulation and the experiment show that the chip production rate decreases when the minimum chip thickness becomes larger than the uncut chip thickness. Also, the reliability of this estimator is evaluated. The probability of correct estimation of the cutting edge radius is more than 80%. This cutting edge wear estimator could be applied to an online tool wear estimation system. Then, a large number of cutting edge wear data could be obtained. From the data, a cutting edge wear model could be developed in terms of the machine control parameters so that the optimum control parameters could be applied to increase the tool life and the machining quality as well by minimizing the cutting edge wear rate.

In addition, in order to find the stable condition of the machining, the stabillity lobe of the system is created by measuring the dynamic parameters. This process is needed prior to the cutting edge wear estimation since the chatter would affect the cutting edge wear and the chip production rate. In this research, a new experimental set-up for measuring the dynamic parameters is developed by using a high speed camera with microscope lens and a loadcell. The loadcell is used to measure the stiffness of the tool-holder assembly of the machine and the high speed camera is used to measure the

natural frequency and the damping ratio. From the measured data, a stability lobe is created. Even though this new method needs further research, it could be more cost-effective than the conventional methods in the future.

DEDICATION

To God

To my parents and brother

ACKNOWLEDGEMENTS

TABLE OF CONTENTS

LIST OF TABLES

LIST OF FIGURES

xiii

CHAPTER 1

INTRODUCTION

Section 1. Overview

This dissertation covers two research topics on micro-milling. First, a study is conducted to estimate tool wear rate from measuring chip production rate in micro-endmilling. Next, the dynamic properties of a micro-endmilling system are investigated so that the tool wear estimation research could be conducted in stable cutting conditions.

A new method for estimating tool wear rates by detecting changes in the chip production rate due to changes in the minimum chip thickness (MCT) is described first. The proposed method has the potential to overcome the shortcomings of existing tool wear measuring methods including the lack of time efficiency and a defined physical link between the state of wear and the wear signature. This new method ameliorate both of these shortcomings.

Based on the MCT effect, the changes in the number of chips are simulated using the relationship between the uncut chip thickness (UCT) and the MCT. The MCT effect occurs when the sharpness of the cutting edge of the tool becomes comparable to the thickness of the material being cut in the micro-milling process. That is, depending on the sharpness of the tip of the micro-sized tool, the chips will not be produced by showing a ploughing effect on the cutting surface when the edge is blunt, or the chip will be produced when the edge is sufficiently sharp.

Next, the actual number of chips produced during a set of cutting experiments is counted and analyzed to validate the simulation results. In order to induce under experimental conditions a ploughing effect known to occur when the cutting edge is worn, the experiment was conducted by adjusting the UCT assuming that the sharpness

of the cutting edge does not change.

In milling, a single chip should be generated once the cutting edge passes through the cutting surface as the tool rotates. However, if the UCT is small enough so that the cutting edge slides on the surface, one chip will not be produced once the cutting edge passes, but one chip will be created when the next cutting edge passes. Thus, if a change in the number of chips is detected, then the sharpness of the cutting edge can be estimated at that time.

We propose the following procedure to estimate the sharpness of the cutting edge during a cutting process. Typically, during a cutting operation, the UCT is maintained at a constant level in micro-milling. Under these circumstances, we hypothesize that the number of chips will decrease if the cutting edge becomes blunt enough to cause the cutting edge to slip relative to the cutting surface. At that time, the feedrate should be increased in order to increase the UCT high enough to increase the number of chips produced per unit time to the original level during the operation. Then, when the cutting edge wears further and the number of chips decreases again, the sharpness of the cutting edge can be estimated again. If these operations are repeated, it will be possible to estimate the sharpness of the cutting edge over time.

This cutting edge radius estimation must be conducted in the stable cutting conditions. The chatter occurs in the unstable cutting conditions which might affect the chip production rate. Chatter is one of the phenomena that impedes machining accuracy. Chatter occurs when the vibration frequency of the tool generated by the cutting edge passing through the varying periodic UCT is similar to the resonance frequency of the tool and the tool holder assembly. Here, a study is conducted to identify the dynamic characteristics of the tool and the tool holder assembly of the micro-milling machine.

2

In order to identify the dynamic characteristics described above, a transfer function of the tool and the tool holder assembly must be determined which is consisted of natural frequency, stiffness, and damping ratio. The conventional method to carry out this process is through impact tests using impact hammers and accelerometers. However, for micro-milling, it is difficult to attach an accelerometer because the tool is small in size. Also, the equipments are expensive. To compensate for these shortcomings, this research suggests using a load cell and a high-speed camera. Instead of using the accelerometer, a load cell is used to measure the stiffness of the tool-holder assembly. A high-speed camera is used to measure the natural frequency and damping ratio of the tool-holder assembly. Based on these, a chatter stability lobe is generated.

The stability lobe is divided into the conditions under which the chatter takes place and does not. The cutting conditions where chatter takes place should be avoided.

This section provides an overview of the entire study. The ideas of estimating tool wear by measuring chip production rate and investigating the dynamic characteristics of the micro-milling system using a vision sensor begin with efforts to overcome the disadvantages of existing methods. Through this study, the feasibility of the proposed methods are demonstrated.

Section 2. Statement of problem: Chip production rate & tool wear estimation

The demand for miniaturized components is increasing in the fields of aerospace, electronics, optics, and biomedical engineering [1]. For example, market research indicates that the microfluidic chip used in the biochemical industry has formed $2.9 B in the global market in 2016 and is expected to increase up to $11 B in 2026[2]. As a result, micro-manufacturing technology is actively being developed. As

an alternative to various non-mechanical micro-manufacturing processes which are limited in terms of workpiece material selection, high cost and poor productivity, micro-milling is well suited for machining micro parts with the required accuracy while compensating for these limitations. The micro-milling process is a miniaturized version of conventional milling [3]. However, the machining theories for the conventional milling, such as the orthogonal cutting model, have failed to successfully explain the micro-milling process due to the small size of the tool [4].

One such characteristic is the unpredictable nature of tool wear. Micro-endmills have a diameter of 1 mm and can be as small as 50 μm. Therefore, the spindle speed required is very high, in order to achieve the necessary cutting speed and develop enough cutting force. The process also requires high feedrate to successfully produce a cut [5]. The tools are small and have significantly lower strength compared to a macro-size tool; this makes tool wear and breakage a very severe problem. Thus, tool wear in micro-milling is an important area of research. Chae et al. [6] suggest that tool wear caused by the inherently high cutting forces and small tool size is a major challenge in micro-milling.

Machining with a worn tool leads to poor workpiece surface finish and dimensional accuracy. There is a large cost benefit that can be availed by monitoring and predicting tool wear to improve tool life and lower rejection of workpieces. These factors have made the tool wear a crucial area of interest.

In order to measure the amount of tool wear, tool condition monitoring systems have been developed. There are two types of methods: direct and indirect.

A direct measure of tool wear is a measurement which is directly related to at least one aspect of tool wear. This measure is not affected by external conditions and

4

hence can provide consistent information for a Tool Condition Monitoring (TCM) system. Direct measures have been used at the macro-scale. For example, a machine-vision based system is used to obtain images of the tool flank surface [7]. A scanning electron microscope or a high-resolution optical microscope is needed to take the images of the cutting edge as shown in Fig. 1(a)&(b). However, the tool has to be uninstalled from the machine to take an image resulting in a tedious and time-consuming procedure. Also, this method cannot be used as an online system which will be needed in the future to achieve better quality and time-saving.

'Indirect' means that the parameter being measured can be correlated to tool wear, but does not reflect the ground truth of the tool or is not a parameter that can be measured on the tool. Cutting force, acoustic emissions (AE), and vibration are some examples. Fig. 1(c) shows the AE signal from the tool breakage. The downfall of this type is that indirect measures could be influenced by non-wear related phenomena.

Tool runout, spindle vibrations, and external conditions can adversely affect the AE sensing and cutting force sensing, which in-turn affects the effectiveness and capability of the TCM system. Also, the indirect measurements do not explain the physical relationship between the tool and the cutting parameters.

In this research, we propose a new tool wear data collecting and monitoring system by measuring the chip production rate in micro-endmilling. Our method explains the physical relationship between the tool and the cutting parameters and could perform as an online or real-time system which is more efficient and time-saving.

Types of tool wear include crater wear, flank wear, and cutting edge wear, etc. as shown in Fig. 1(d). The crater wear occurs on the rake face of the cutting tooth of an endmill due to the sliding chip on the surface. The flank wear appears on the outer

surface of the cutting tooth as a result of friction between the machined surface of the workpiece and the flank. The cutting edge wear can be seen on the edge of the cutting tooth. Fig. 1(e) & (f) shows the flank wear and the cutting edge wear.
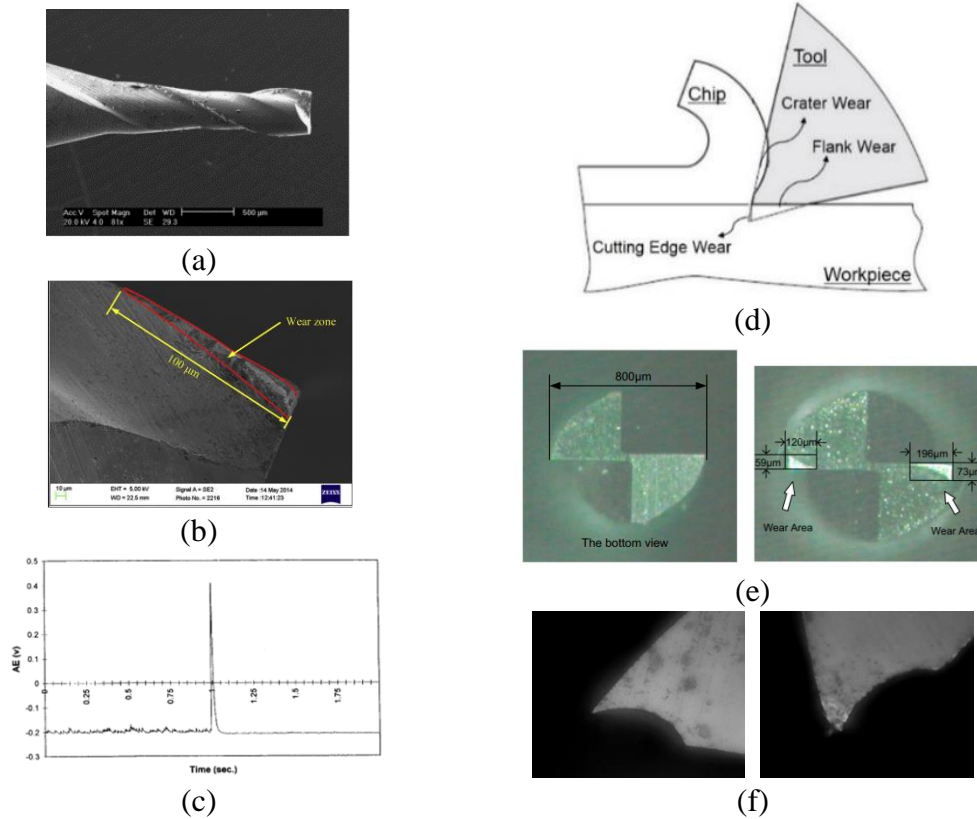
Figure 1. Micro-endmill and tool conditions(a)2-flute 500 µm Micro-endmill [8], (b)tool wear along the flute of the micro-endmill [9], (c)AE signal from tool breakage [10], (d)schematic of tool wear, (e)flank wear [11], (f)cutting edge wear.

The flank wear is generally quantified by measuring the size of the wear land at the bottom of the tool and the reduction in the diameter of the tool. Crater wear does not occur at the cutting edge of the tool but on the rake face slightly above the cutting edge, because crater wear occurs due to the friction between the chip and the rake face before the perfect disposal of the chip. Therefore, we focus on the cutting edge wear which causes more changes to the cutting-edge radius of the endmill more than other types of wear. Micro-milling studies have focused on incorporating the round-edge

model to understand the mechanics of cutting. The cutting edge radius and edge wear are important factors in governing the cutting forces and the thrust force acting on the tool. This in-turn governs the cutting parameters of the process. A large edge radius causes an effective negative rake angle and the small clearance angle [12]. Additionally, changes in the cutting edge substantially increase the cutting forces due to ploughing, friction and elastic recovery of the material. Wang et al. stated the reason for this force increase is the reduced ratio of the UCT to the cutting edge radius [13]. Cutting edge radius has a direct effect on the chip formation process because of the MCT effect. For this reason, the cutting edge radius wear is a more meaningful measure of tool wear for micro-scale tool wear studies.

Many researchers have developed cutting models that incorporate the curved nature of the cutting edge and defined the parameter of MCT. Ikawa et al. [14] classified the MCT as the most critical parameter in micromachining. Their theory incorporated a round-edged tool and they defined MCT as the critical value of thickness below which no stable chip formation would take place. Aramcharoen and Mativenga [12] have termed this phenomenon as one of the many characteristics of the micro-scale referred to as "size-effects". According to them, when the UCT is below the MCT threshold, the cutting tooth begins to rub on the surface of the workpiece rather than creating a metal shearing plane. Thus, no cutting takes place and no chip is formed. This 'rubbing' of the tool is generally referred to as 'ploughing'. The workpiece material is compressed and then recovers after the cutting tooth passes. This is an 'elastic recovery' of the workpiece material. Only with UCT larger than MCT, chip formation is possible. Kim et al. [15] created a theoretical model to account for the lack of formation of chips on each pass of a cutting tooth, especially at lower feedrates. When the UCT is sufficiently

high, each cutting pass produces a chip and the cutting is termed as a "steady cutting regime". This is the theoretical prediction based on the round-edged cutting model which shows that the feedrate per tooth of the tool is significant in determining the chance of production of a chip. Similar studies have been done to derive and establish theories of micro-machining and chip formation [15, 18]. It was found that as the tool wears out, the minimum feed per tooth required increases which should cause intermittent chip formation.

The value of MCT is not constant for all cases. It varies based on the cutting edge radius of the tool used and also on the type of workpiece material being machined. Kim et al. [15] experimentally found the MCT to be 22-25% of the cutting edge radius of 3 μm for a 600 μm micro-endmill. In [17], Yuan et al. experimentally observed a similar result. The MCT is approximated as 25-30% of the cutting edge radius. In this study, we begin by introducing a theoretical correlation between the number of chips produced during machining and the condition of the tool. We have published the development of this relationship in [18].

Using the MCT effect, the number of chips is considered as a new parameter that is directly affected by the tool wear, especially the cutting edge wear. Therefore, by counting the number of chips during cutting, we can determine whether the MCT is below or above the UCT. At the moment that the MCT crosses the UCT, the value of the cutting edge radius can be directly determined. Since the value of the UCT can be directly controlled by the feedrate, an experiment can be designed in which the feedrate is varied, and the number of chips is measured to determine when the UCT has crossed the MCT. By repeating this experiment many times during cutting over the life of an endmill, the rate of endmill wear can be determined, and a large amount of data relating

8

cutting-edge wear to machining parameters can be gathered automatically, without human intervention.

As a first step, we present a cutting simulation of the micro-endmilling process based on the geometry of the trochoidal path of the cutting tooth and the MCT effect to investigate the relationship between the chip production rate and the state of the interaction at the tool-workpiece interface. Also, experimental validation is performed to verify our proposed method. It is found that the number of chips produced drops with respect to the feedrate of the cutting process when the UCT is below the theoretical MCT. Then, the reliability of the proposed method is evaluated.

In this section, the need for this new tool wear estimating method and the feasibility of this method is discussed.

Section 3. Statement of problem: Dynamic characteristics of micro-milling

In micro-milling, it is important to understand the dynamic characteristics of the system prior to the cutting edge radius estimation research, because the unstable cutting conditions which generate chatter would influence the chip production rate in micro-endmilling. But, chatter is not considered in this cutting edge radius estimation research. Therefore, the stable cutting conditions should be found and applied to the cutting process.

However, in micro-endmilling, it is not possible to use the existing method, such as using an accelerometer and impact hammer, due to the small tool size. In this research, we propose a new experimental method to generate the stability lobes in micro-milling using a vision sensor: a high-speed camera with a microscope lens. A 2-DOF dynamic structural transfer function of micro-endmill is obtained by measuring

the stiffness, the natural frequency and the damping ratio of the tool tip for the 1st mode shape. The high-speed camera is used to measure the displacement of the tool tip under the constant input force and the natural frequency and the damping ratio are obtained by tracking the points in the selected feature on the tip of tool while it is having free vibration with damping generated by an impact on the tool shank using an impacting device. The chatter stability lobes are generated based on the dynamic transfer function.

This section briefly explains the necessity of the newly proposed method of examining the dynamic characteristics of the micro-milling system using vision sensor by comparing to the existing methods.

Section 4. Expected impact on micro-milling field

The development of the cutting edge wear estimator studied in this research will have a positive impact on micro-milling field. The cutting edge wear estimator enables the real-time data collection for modeling and evaluation of models of the cutting edge wear rate. By modeling and evaluating the cutting edge wear rate from the cutting process using different workpieces and micro-milling tools, the tools that are suitable for a specific workpiece can be found. Also, by comparing the change in cutting edge wear rate with the presence or absence of coating on a micro-mill, it is possible to determine which coating material minimizes the wear rate. Prior to this research, this data could only be collected through a time and human-labor intensive process. This research enables fast and automated tool wear data collection. Thus, this cutting edge wear estimator can be used not only for finding the optimum tool materials but also for designing a tool that minimizes the wear rate.

In the next chapter, literature reviews on related studies are explained.

CHAPTER 2

BACKGROUND

In this chapter, the literature review is represented with the topics that are closely related to the main research topics of this dissertation. The types of tool wear and the existing tool wear models are explained. Then, the reviews on the tool condition monitoring system is followed. This chapter also includes explanation on the important concepts in the micro-cutting mechanism such as UCT, MCT, and cutting edge radius. Since the chips play a key role in this research, the chip formation and the related studies are explained. In addition, the influences of microstructure of the workpiece material on micro-machining are reviewed. In the last section, the existing studies on chatter are included.

Section 1. Tool Wear

Tool wear has a significant impact on the machining process. Worn tools reduce the quality of machined parts as well as the life of the tool. The measure of the quality of the machined parts can be divided into the roughness of the surface and machining accuracy. Worn tool shortens the life of the tool itself as well. This is because the worn tool increases the cutting force, which increases the tool wear rate. Here we describe the types of milling tool wear and the impact on the quality of the machined parts and the endmill.

For milling tools, tool wear can be largely divided into three types: flank wear, crater wear, and cutting edge wear.

Flank wear is caused by friction between the side of the tool and the cutting surface, when the side of the tool and the cutting surface make contact during a tooth

pass. Flank wear is known to be more prominent towards the bottom of the tool, causing a decrease in the diameter of the bottom of the toolrelative to the top of the tool. Active research is underway to identify the cause of this phenomenon. For example, when cutting a single straight channel, when cutting with a tool with flank wear, the width of the bottom of the channel is less than the width of the top of the channel. Flank wear also affects the sharpness of the cutting edge. Particularly in the lower part of the tool where the diameter of the tool decreases, the machining characteristic can be changed by the increased or decreased sharpness of the cutting edge due to the combined effect of crater wear and flank wear. However, it is not yet clearly determined whether the cutting edge becomes sharper or duller. Flank wear, which has these effects, is directly related to the quality of the machining. Therefore, many studies have been conducted to quantify the amount of wear. Typical methods include measurement using image processing, measurement using cutting force, and measuring the width of the bottom part and the upper part of the channel after at the straight channel cutting process as shown in Fig. 2[19, 20, 9, 21]

For image processing methods of measuring tool wear, the image of the tool is taken using a microscope. Then, the worn area is visualized and separated from the other parts of the tool on the image. The wear is then calculated by obtaining the size of the area as shown in Fig. 2(a)[22].

The flank wear has an effect on cutting forces. If the flank surface is in contact with the cutting surface and wear occurs during cutting, the cutting force also increases because of friction increase. Research has also been conducted to estimate how much wear has progressed through analyzing the changes in the cutting force as shown in Fig. 2(b)[20].
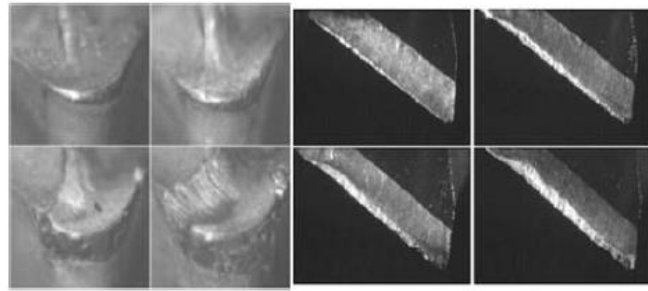
(a)
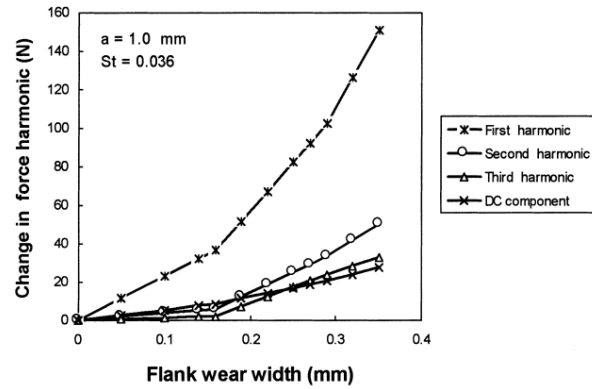
(b)

(c)
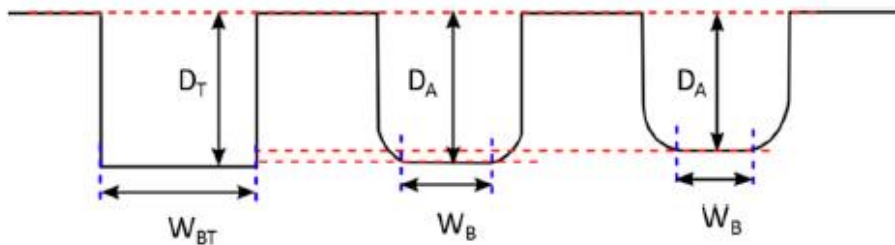
(d)

Figure 2. Flank wear (a)Worn tool examples. Left (clockwise from top left): turning inserts after 6, 18, 28 and 33 minutes use. Right (clockwise from top left): milling cutter face after 6, 19, 25 and 27 minutes of use[22], (b)The relation between change in force harmonics and tool flank wear [20], (c)Image of slot cross section, and (d)slot profile measurement parameters[21].

In addition, when wear occurs, the audio signal generated during cutting also changes. Measurement of the amount of wear by analyzing the sound signal has also been investigated [24].

13

In micro-milling, the size of the tool is so small that it is difficult to measure or estimate the flank wear by any of the conventional methods used at the macroscale. Visual methods are time-consuming because the images of the worn tool should be taken by a microscope. Therefore, studies were conducted to overcome this limitation. Online flank wear estimating system was developed by using the experimental milling force model as shown in Fig. 3.[23].
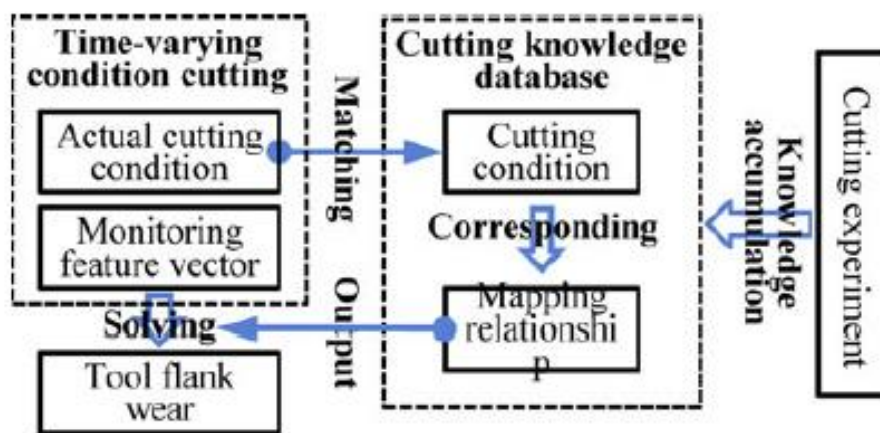
Figure 3. Flow chart of tool flank wear online recognition method in time-varying cutting condition by using the cutting force[23]

Unlike the flank wear, the interest in crater wear is not very high, but some studies has also been done. Crater wear occurs at the inner surface of the cutter blade in milling, which is the part where the chip being cut slides up on it as shown in Fig. 1(d) & Fig. 5. Therefore, the crater wear is caused by the friction between the chip and the rake face. Depending on the design of the tool, the crater part has a different design. The reason for this is that the crater portion is closely related to the formation of the chip, and the design that smooths the chip discharge has been studied and the groove design is different accordingly. Crater wear appears to affect chip formation as shown in Fig. 4&6. [27, 28].
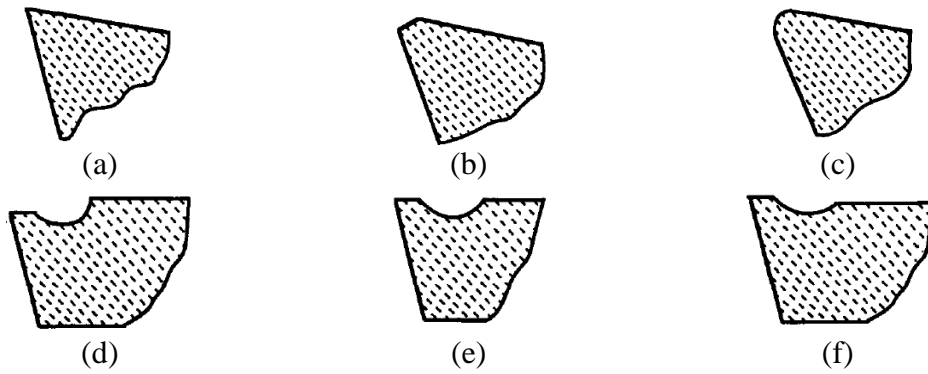
Figure 4. Cutting edge/chip former configurations (a)straight cutting edge, (b)chamfered cutting edge, (c)round cutting edge with flat rake face, (d) raised back –wall chip groove, (e)standard chip groove, (f)reduced back-wall chip groove[27]
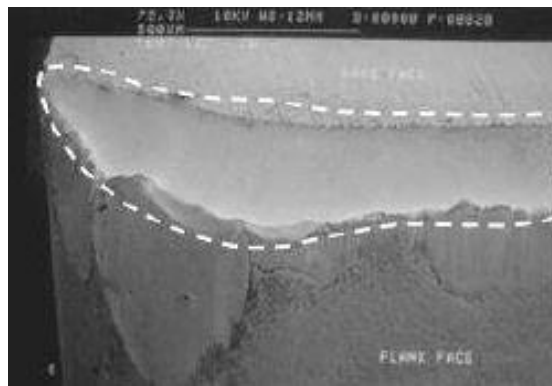
Figure 5. Rake face wear overview of an ISO K20 cemented carbide cutting tool after machining Ti-6Al-4V[29]
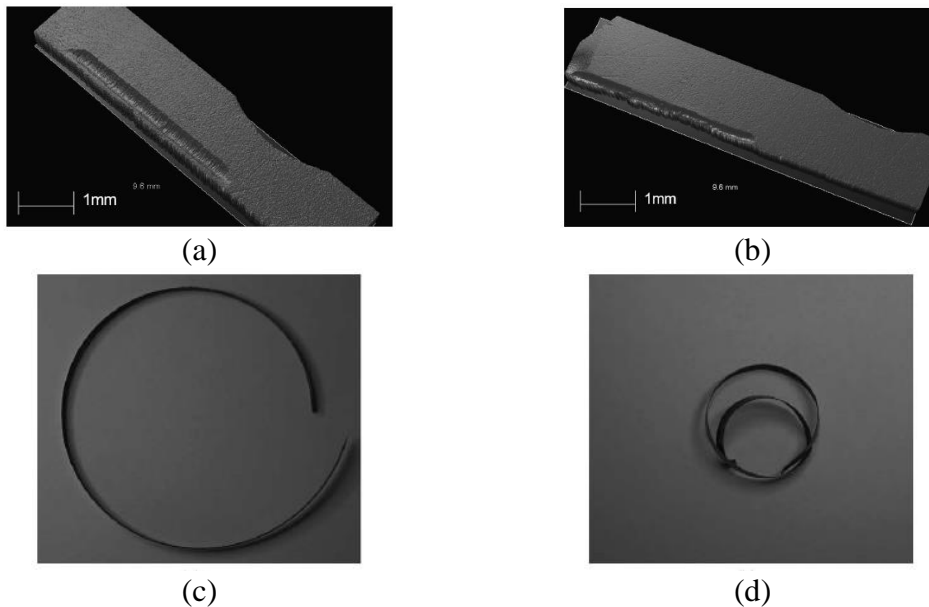
Figure 6. Crater wear and chip formation(a)craters for 480 m/min and 0.25 mm/rev, (b)craters for 960 m/min and 0.25 mm/rev, (c)chips for 60 m/min and 0.15 mm/rev, (d)chips for 240 m/min and 0.15 mm/rev[28].

Particularly, in the case of micro-milling, since the size of the tool is very small, there is a possibility that the process of forming the chip will be changed according to the shape of the part where the crater and the cutting edge are connected. Since the interest in crater wear is not so high, research on the measuring method has not been studied as much as the measurement of flank wear. However, this crater wear measuring method was also done through image processing and analysis of cutting sound.

Cutting edge wear refers to the reduction in sharpness due to friction that occurs on the cutting edge. It is known from the FEM simulation results that the cutting edge radius increases as the cutting edge wear increases[9].

Cutting edges are very important because they are directly involved in chip formation. If the cutting edge is round as in the case of micro-milling, the material to be cut starting from the stagnation point will split under and over the cutting edge as shown in Fig. 7&8[30, 31]. If the workpiece material goes to the lower side of the cutting edge, it passes through the flank surface. When it goes up, it becomes a chip and passes through the crater surface. At this time, the elasto-plastic behavior of the workpiece material moving along the rounded surface of the cutting edge can be said to be the key to chip formation. And, it is the cutting edge wear that largely affects this part.

Typically, a microscope is used to measure the cutting edge. An image of the cutting edge is taken by a microscope and the image processing is applied to find the radius of the round cutting edge by drawing a circle as shown in Fig. 9(c)&(e)[32–34]. The radius is a measure of the sharpness of the edge. In micro-milling, a high-resolution microscope or a scanning electron microscope should be used. Sometimes a surface profilometer can be used, which measures the radius from a three-dimensional image.

(a)

(b)
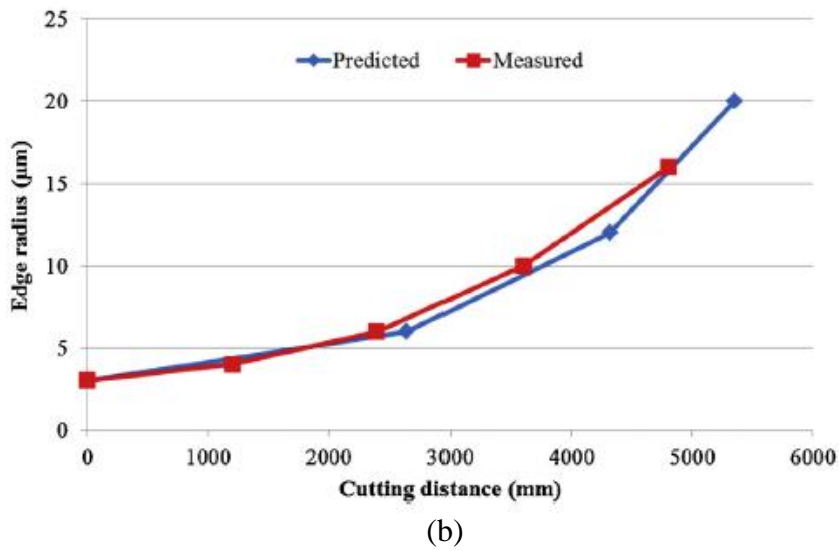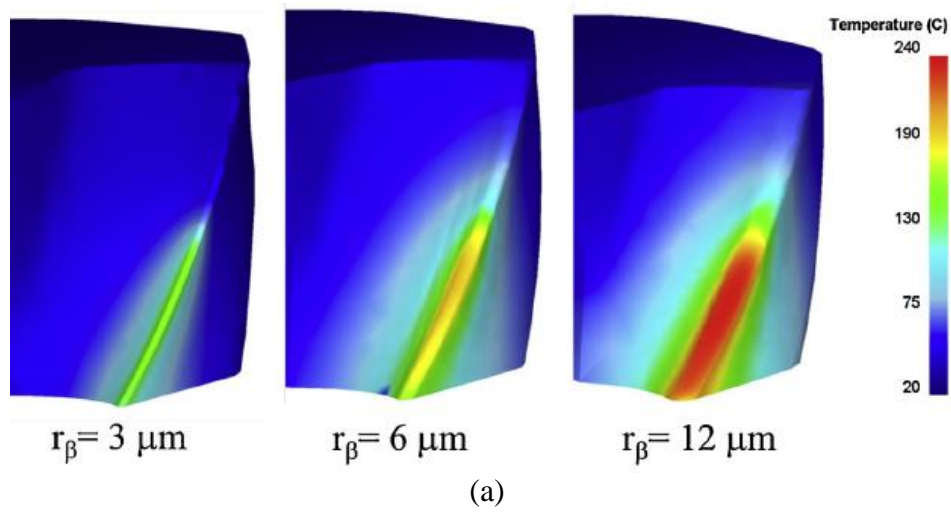
Figure 7. Cutting edge wear of micro-endmill(a)Tool wear depth distributions along the flute of the micro-endmill, (b)a comparison of measured tool wear against predicted tool wear[9].
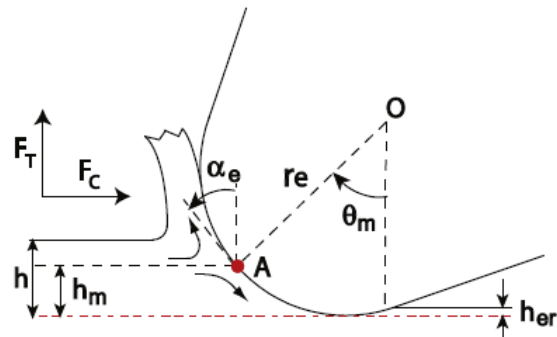
Figure 8. Cutting mechamism using an edge radius tool[31].
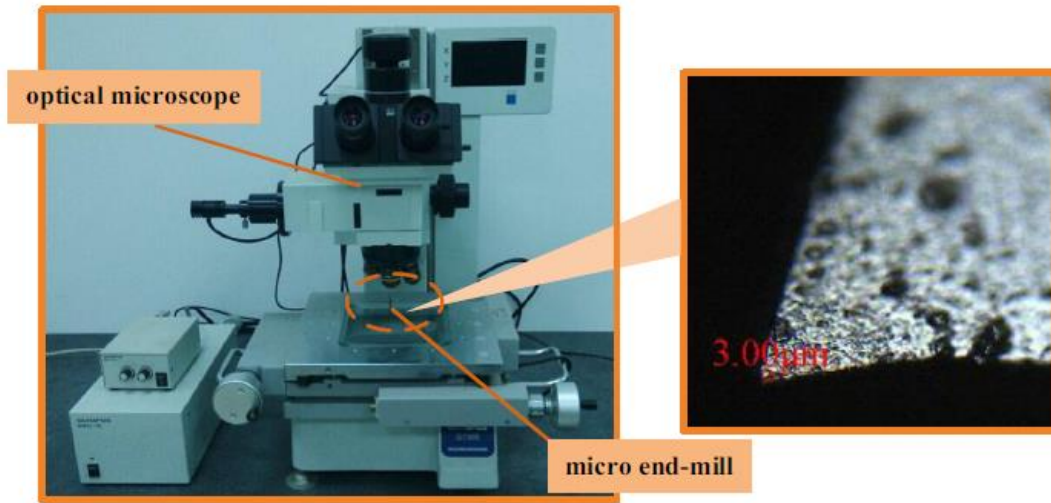
(a)
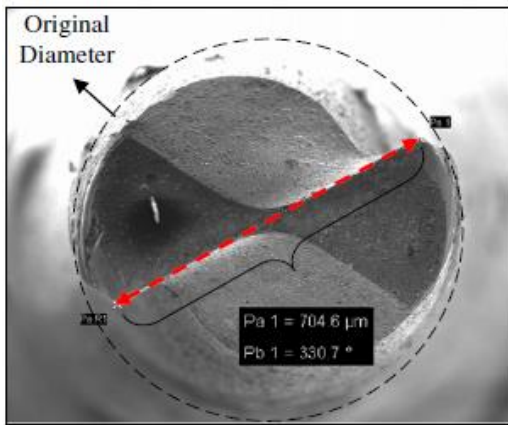
(b)
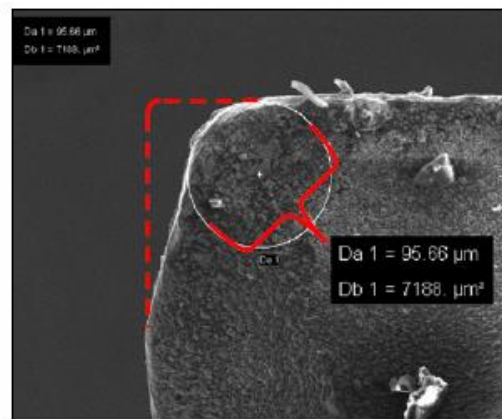
(c)
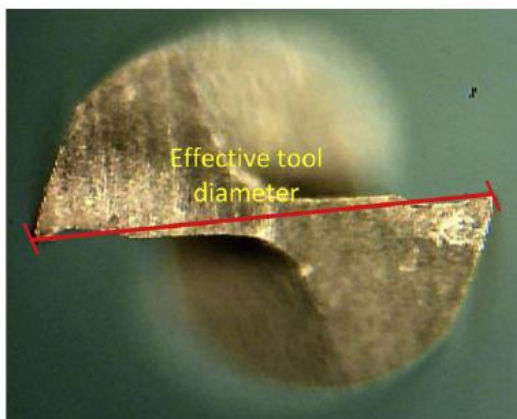
(d)
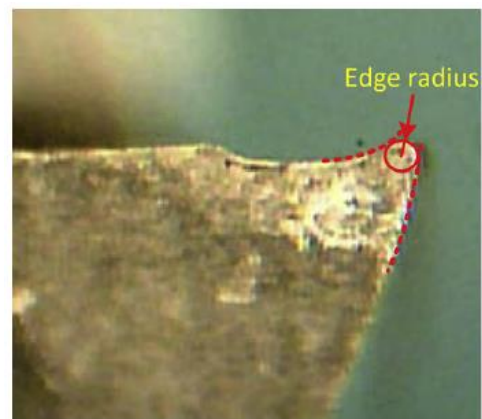
(e)

Figure 9. Measurement of cutting edge radius(a)Experiment set-up to measure edge radius, (b),(c)measurement of tool wear: effective tool diameter(left) and tool edge radius (right)[32–34].

The measurement of the cutting edge requires a very long time and effort. First, the cutting operation must be stopped and the tool removed from the spindle. An image is taken by a microscope and the image is analyzed through image processing. A circle is drawn on the cutting edge during this process. When drawing a circle, a person looks at the edge with the eyes and draws it. Repeat measurements must be made because accuracy can be poor.

So far, the tool wear have been classified according to the location where the tool wear occurs. However, there are various kinds of wear mechanisms. Only one wear mechanism may appear or multiple wear mechanisms may appear at once. From now on, a description of the wear mechanism follows.

There are four types of wear mechanisms as shown in Fig.10 & 11 & 12. The first is the abrasive wear, which causes the surface of the tool to be worn by small particles generated during cutting. Second, the adhesive wear occurs when the tool surface and the workpiece material stick together due to heat generated by the friction.
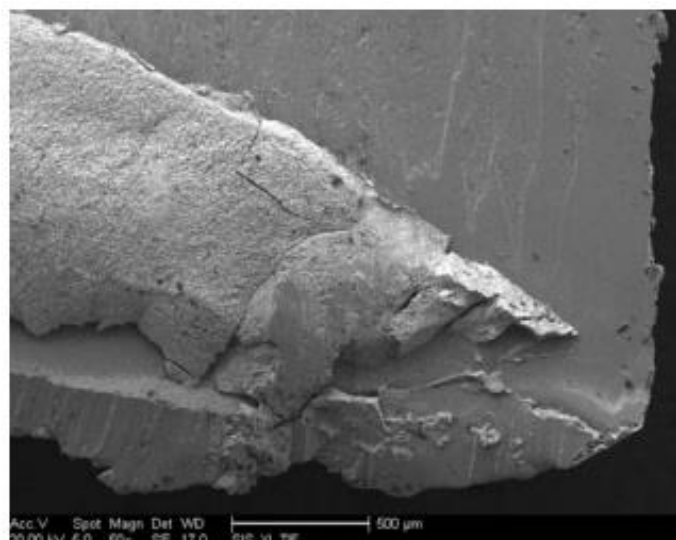
Figure 10. Adhered chip on the cutting edge from the tool-chip adhesion[35]
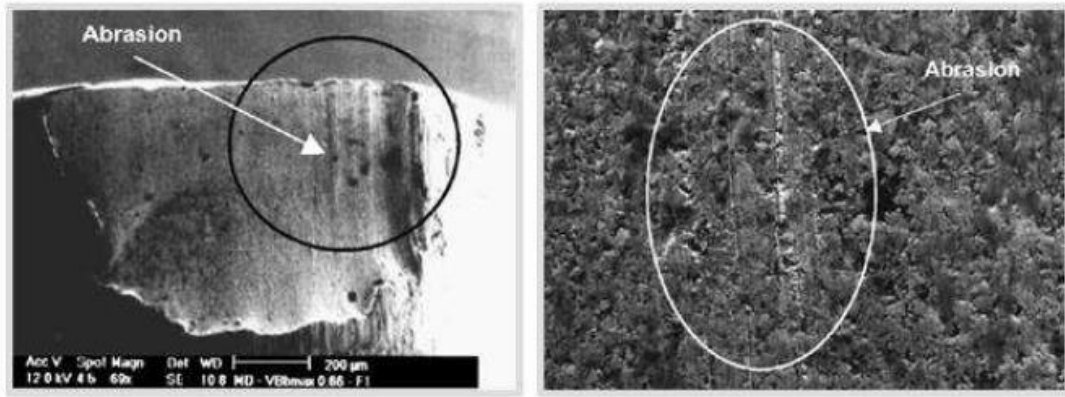
Figure 11. Evidence of abrasion on a cemented carbide tool[29].
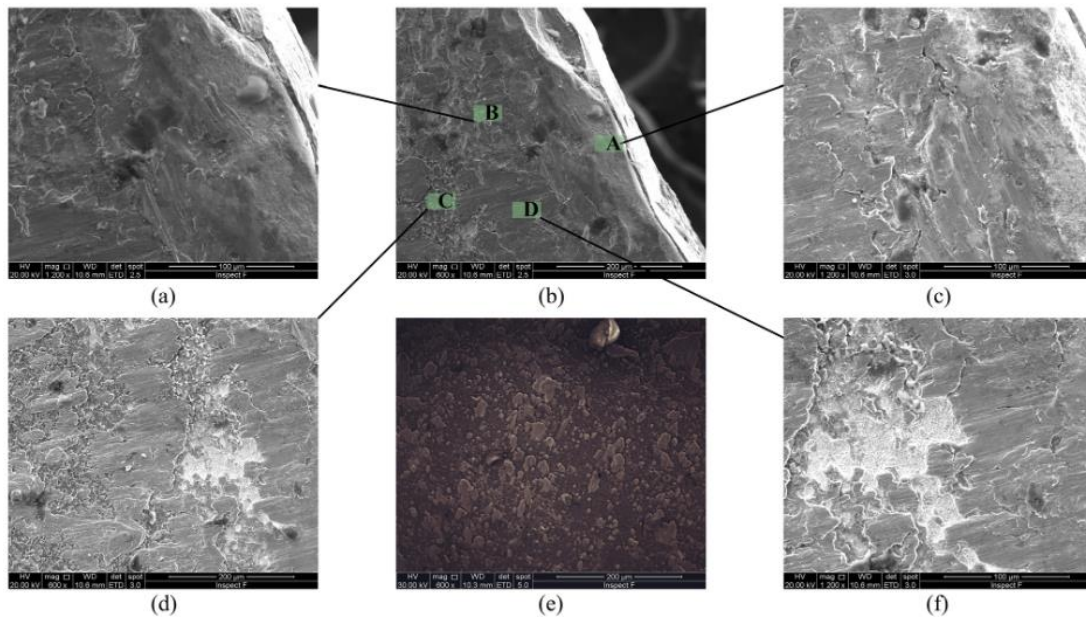
Figure 12. SEM images of rake face (a)oxidation and diffusion wear, (b) distribution graph, (c)mechanical and thermal cracking, (d)oxidation and diffusion wear, (e) original component of the tool coating and (f)adhesive wear[36].

The diffusion wear results from the transfer of atoms from the tool material to the workpiece material when they are in contact. This wear changes the chemical composition of the tool and workpiece material. Lastly, the oxidation wear reduces the tool wear. The presence of a small oxide film on the surface of the tool helps to reduce the tool wear, but at high temperature, the film quickly disappears[37].

This section explains the three main types of tool wear: flank wear, crater wear,

and cutting edge wear. Also, the tool wear mechanisms are described. The following section includes the tool wear models.

Section 2. Tool wear modeling

Tool wear measurement useful for understanding the current state of wear of an endmill, but modeling of tool wear can be useful to predict and reduce tool wear. Therefore, in order to understand the tool wear, many studies have been done on the modeling of tool wear.

The modeling based on the experimental data is carried out after obtaining data by measuring tool wear through the methods described previously. However, empirical modeling is not necessarily physically meaningful. Analytical modeling is performed to understand the physical sources and causes of tool wear. There are many variables needed in analytical tool wear modeling because of the multiple interactions involved. These tool wear models are described.

First, Taylor[38] modeled tool life based on tool wear. The relationship between the area of the flank wear, the cutting time and the cutting speed was experimentally determined as shown in Fig. 13. Based on this, a formula for predicting tool life was proposed. Shaw and Dirke [39] modeled the wear on sliding surfaces when two surfaces were in contact as shown in Fig. 14. They applied the model to the cutting mechanism.

An equation representing the relationship between the area of the flank wear(w) and the cutting distance(L) was proposed as Eq. (1) with a constant number (c).

$$L = c\,w^2 \qquad (1)$$

21
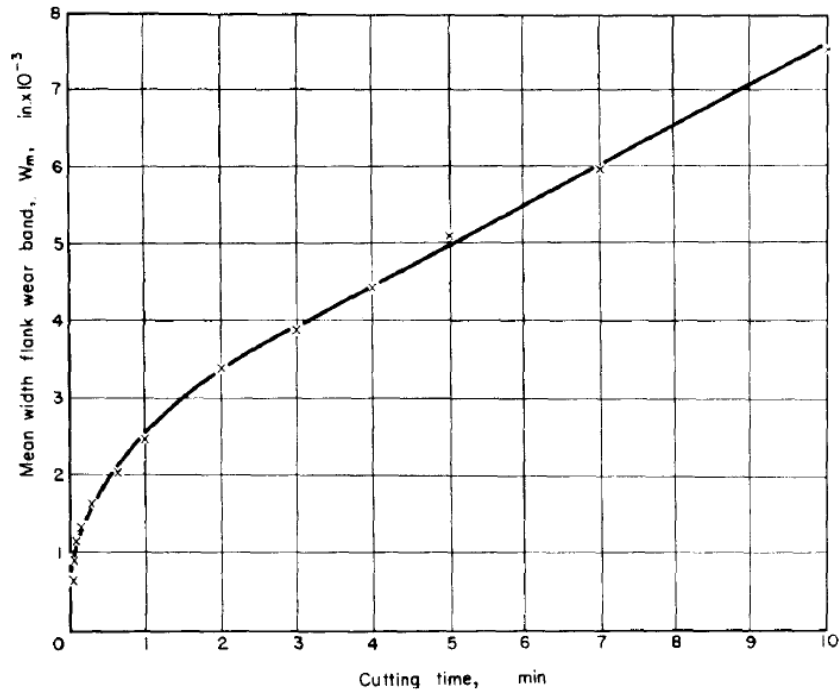
Figure 13. Graph of flank wear vs cutting time[40].

| (a) | (b) |
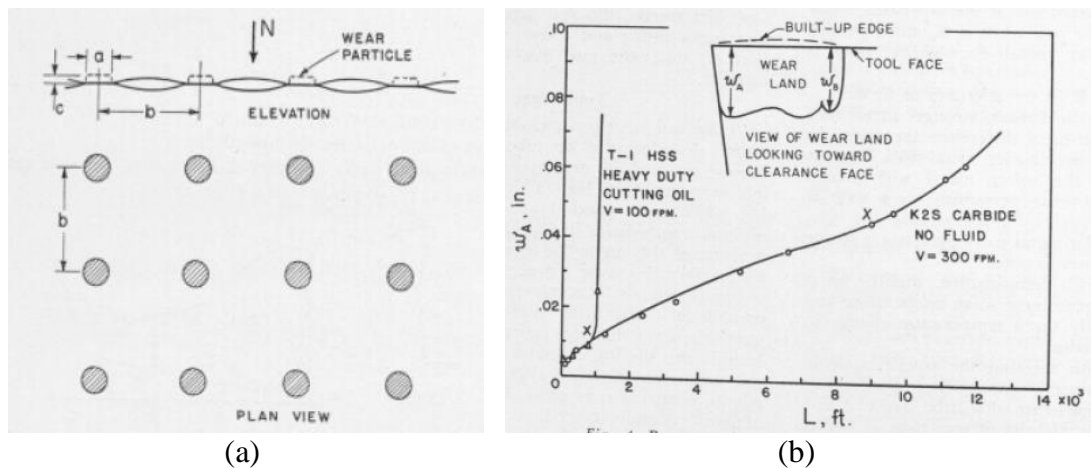
Figure 14. Tool wear from the contanct between surfaces(a)Statistical picture of points of contact between surfaces in contact, (b) representative wear land curves for carbide and HSS tools cutting M-2 tool steel of 220 Brinell hardness[39].

Usui et al. [41] proposed the relationship between flank wear and cutting time by applying variables such as diffusive wear, adhesive wear, temperature and strain to the models of Shaw and Sirke. The result is shown in Fig. 15(a).

22

(a)   (b)
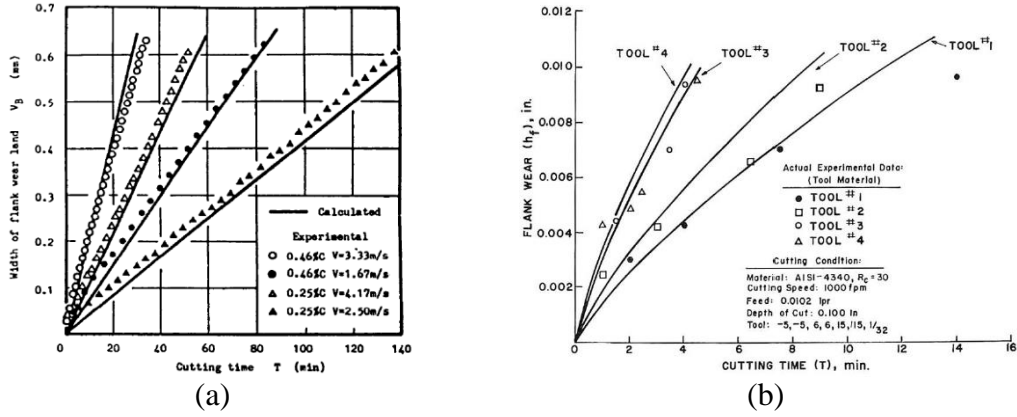
Figure 15. Flank wear model(a)Comparison between predicted and measured progress curves for flank[42], (b)theoretical flank wear rate curves of four tools of different compositions with actual experimental data[43].

Takeyama et al.[44] suggested that the total amount of tool wear is assumed to be the addition of the terms due to brittle fracture, mechanical abrasion, physicochemical mechanism or rate process, and other mechanisms.

Bhattacharyya and Ham [43] studied a statistical model for the mechanical wear process. The increment in the flank wear is calculated based on the number of wear particles produced in a certain amount of time, and the rate of wear mass is obtained as a result. The result is shown in Fig. 15(b).

Kannatey-Asibu [45] developed the flank wear rate equation with the consideration of the effects of diffusion and adhesion.

Only a few studies have been done on the analytical modeling of tool wear in micro-milling.

Jun et al. [46] proposed a new wear parameter in terms of the difference in edge radius(r_e) and the decrease(δ_t) in the tool diameter(D_t) as Eq. (2).

$$\Delta r_e = \frac{1}{2}\left[\left(r_{e1,worn} - r_{e1,new}\right) + \left(r_{e2,worn} - r_{e2,new}\right)\right]$$

(2)

$$\% \, \delta_t = \frac{100(\delta_{t1} + \delta_{t2})}{D_t}$$

23

Bao and Tansel[47] introduced the analytical cutting force(F_u) model in micro-endmilling process with the tool wear representation (K_w: wear coefficient) capability as Eq. (3) and the model is shown in Fig. 16(c).

$$F_u = \frac{K_w K_m r f_t}{2 \tan \beta}$$

(3)

$$K_w = 1 + (C_1 L)^{C_2}$$

(a)   (b)

(c)
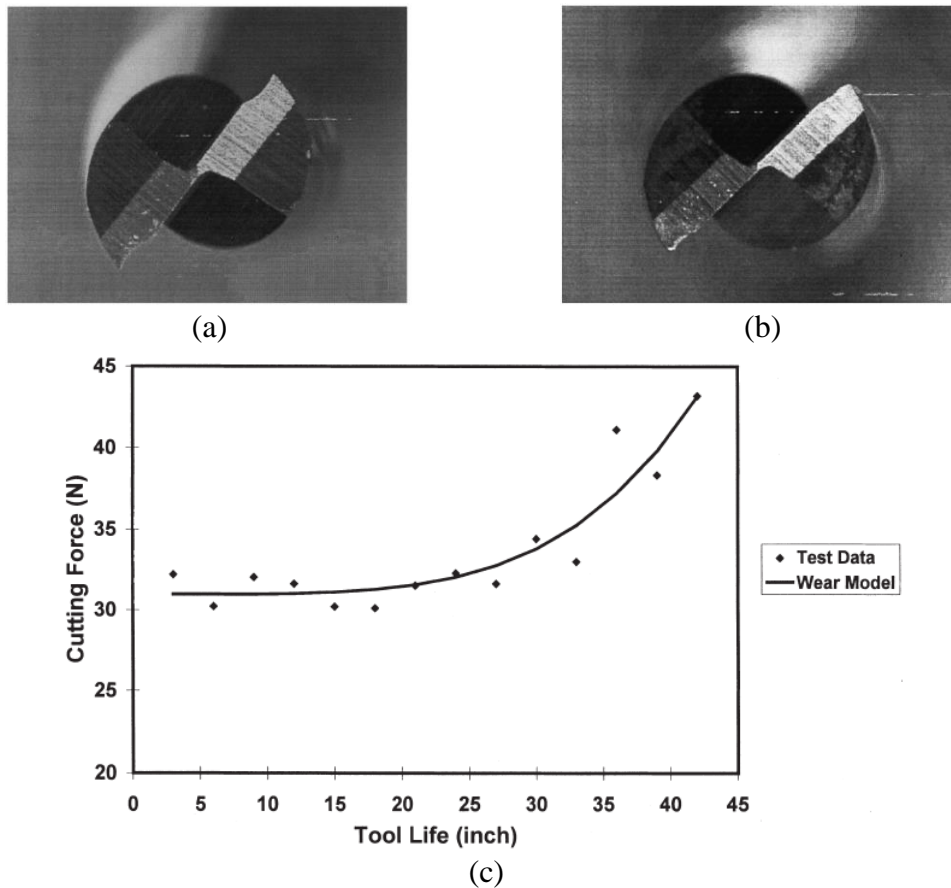
Figure 16. Micro-endmill and wear model (a)new tool, (b)worn tool, (c)wear model of the NAK-55 steel wear[47].

In this section, the existing tool wear models are described. In order to develop a Tool wear model, it requires tool wear measurements. Thus, the next section presents

a study on the measurement of tool wear. And, because the state of the tool including tool wear has a large effect on the machining performance, methods of monitoring the condition of the tool are also included in the next section.

Section 3. Tool condition monitoring system

A tool condition monitoring system refers to a system that monitors tool condition offline or online. The condition of the tool includes not only tool wear but also tool breakage. Tool wear monitoring can be divided into direct monitoring and indirect monitoring approaches. Here, the types of monitoring and the existing studies are explained in chronological order.

In the 1960's, the research on the tool condition monitoring starts to increase.

Keiji and Katsundo[48] found that the relationship between the cutting force and the flank wear is almost linear in the turning process. They discovered that when the flank wear increases the cutting force increases in almost linearly. Iwata [49] proposed a flank wear monitoring method using acoustic emission (AE) signal by counting the number of the signal which has the amplitude that exceeds the predetermined threshold as shown in Fig. 17.

(a)   (b)
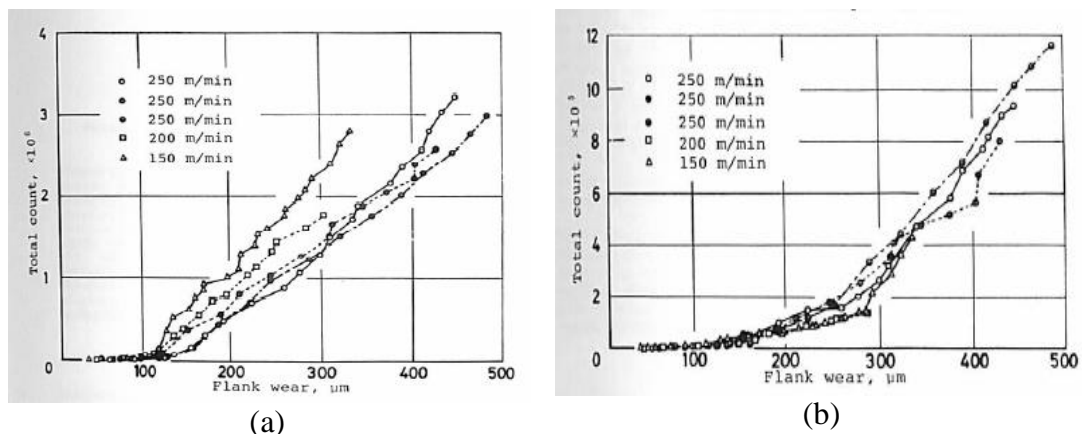
Figure 17. Total count of acoustic emission versus flank wear (a)threshold voltage=50 mV, (b)threshold voltage=100 mV[49].

25

Rao[50] proposed a Wear Index(WI) which increases with the increasing flank wear-land. This WI is derived based on the relationship between the dynamic behavior of the tool and the flank wear which is the ratio of the force amplitude at first natural frequency of tool holder to vibration amplitude at the same frequency. The results are shown in Fig. 18
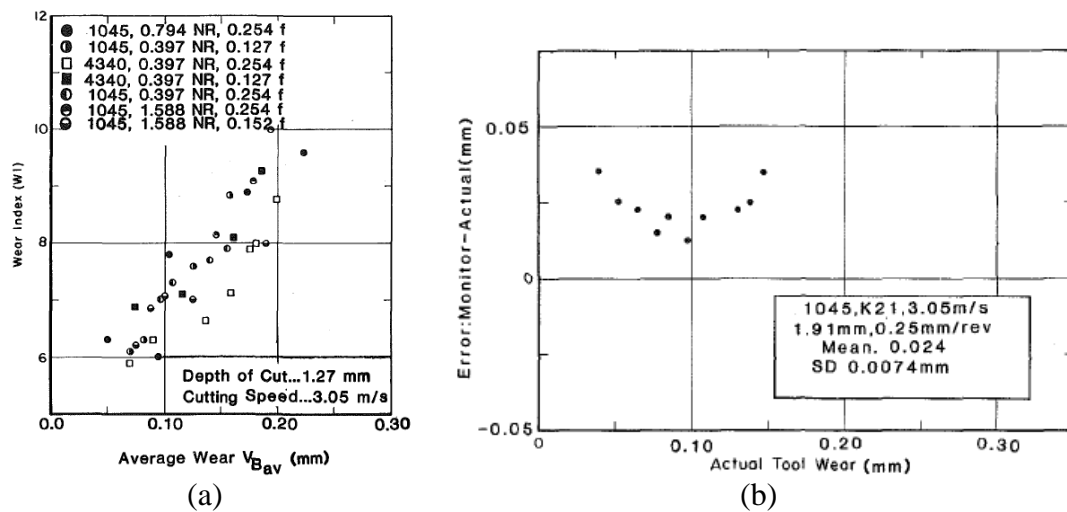
Figure 18. Wear Index of flank wear(a)wear index versus wear, (b)monitoring errors versus tool wear[50].

Diei and Dornfeld[51] conducted research on sensing the tool wear from the AE signal in Face milling. They found that the AE root mean squared (RMS) value and the specific cutting force have good correlation. These values tend to increase with the increase of the flank wear. Jeon and Kim [52] developed an optoelectronic method to monitor the flank wear of cutting tool by using image processing. They measured the wear land width from the image which shows the illumination of the laser beam from the wear zone.

In the 1990's, the interest in the Neural Network increased. Rangwala and Dornfeld [53] applied Neural Network to the AE signal and the cutting force to be able

26

to classify the tool condition into two, new and worn. In Fig. 19(a), the fresh and worn tool clusters are clearly separated. Purushothaman and Srinivasa[54] proposed the back-propagation algorithm to the tool wear monitoring system to be able to distinguish between the fresh tool and worn tool. They used the cutting operation control parameters as the input and predicted the output which is the flank wear-land width. Lim [55] investigated the relationship between the vibration amplitude and the flank wear in the turning process. Prior to the tool wear, the vibration acceleration amplitude generates two peak amplitudes. And the signal can be used as a tool wear indication as shown in Fig. 19(b).
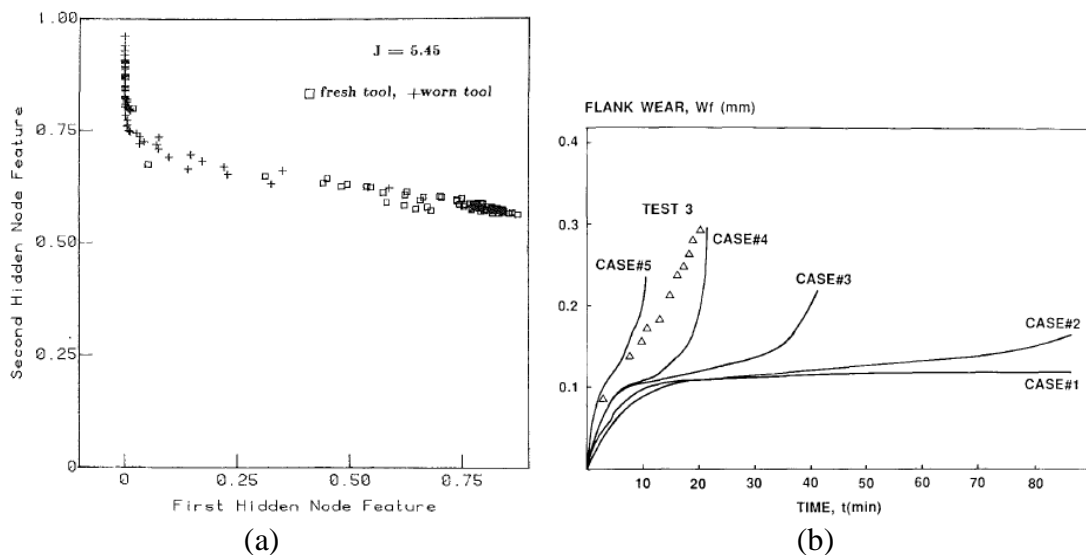
Figure 19. Tool wear monitoring system using difference sensor signals(a) AE signal : Two dimensional feature space(hidden node features)[53], (b)Vibration : Flank wear wear model in turning process[55].

Lin and Lin [56] applied the Neural Networks and estimated the average flank wear in face milling. Xiaoli and Zhejun [57] proposed the tool wear monitoring method by applying the fuzzy clustering method. They classified the tool wear into 4 classifications: initial, normal, acceptable and severe wear. Li et al. [58] developed a

tool condition monitoring system based on the adaptive neuro-fuzzy method. The current from the feed motor is measured and the feed cutting force is estimated from the measured values. The feed cutting force is used to determine when to replace the tool. Ertunc et al. [59] proposed two online tool wear identification method based on the cutting forces and the spindle power signals in drilling. They applied Hidden Markov Models and classified the tool wear into three conditions, sharp, workable, and dull as shown in Fig. 20.

(a)

(b)
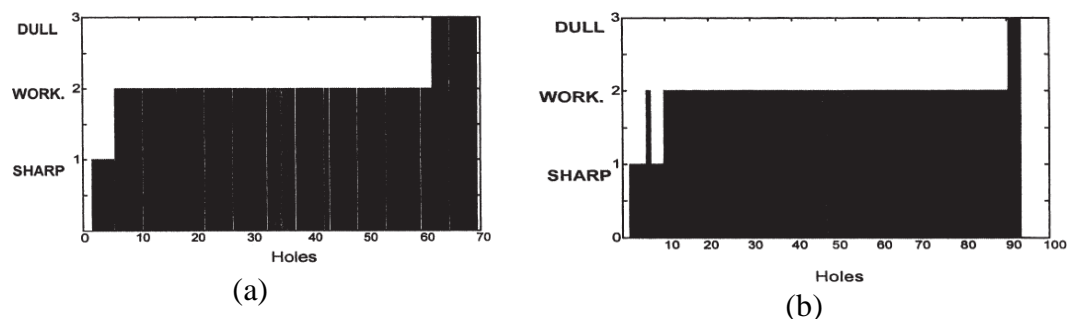
Figure 20. Spindle power vs. tool wear(a)experiment 1, and (b)experiment 2[59].

Moriwaki et al. [60] suggested that the nominal specific cutting resistance which can be obtained from the cutting force at smaller feedrates is expected to increase as the tool wears through an exponential decay function. They found out that the index value which is in the exponential decay function is used to estimate the tool wear. There has been more research on the tool condition monitoring system for the macro-sized cutting tools.

However, as the size of the cutting tools becomes smaller, the studies on the tool condition monitoring system for the micro-tools starts to increase from the late 1990s.

Tansel et al. [61] conducted research on how to predict the tool breakage before

28

the tool fails. They investigated the cutting force variation patterns during micro-endmilling process and developed the tool breakage predicting method as shown in Fig. 21(a). Tansel et al. [62] applied the Genetic Algorithm to estimate the cutting force coefficient which indicates the dullness of the cutting edge for micro-endmilling as shown in Fig. 21(b). Jemielniak and Arrazola [63] showed that the acoustic emission signal and the cutting force in micro-endmilling are largely influenced by the tool wear.

Malekian et al. [8] used accelerometers, force and acoustic emission sensors for the tool wear monitoring in micro-endmilling. The classification of the tool wear is conducted by applying the neuro-fuzzy method to the sensor signals. And the monitoring method is verified through the cutting test as shown in Fig. 22(a)

(a)

(b)
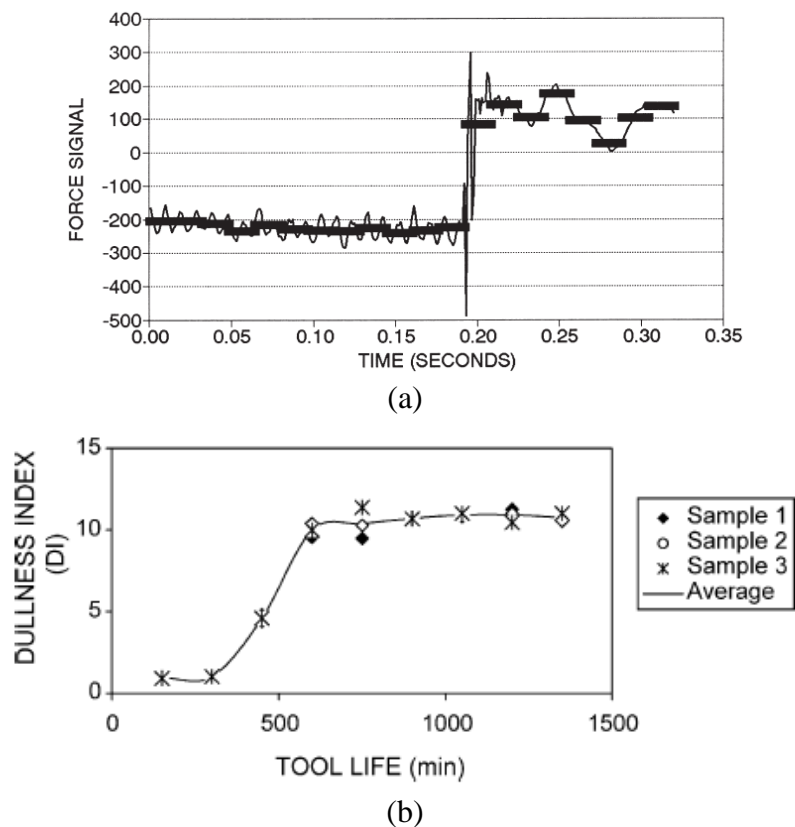
Figure 21. Cutting force and tool breakage/wear(a)Original data and the reconstructed waveform are presented just before and after breakage takes place[61], (b)variation of the dullness index while the tool wears out[62].

29

Hsieh et al. [64] attached the accelerometer to the spindle holder and measured the vibration in micro-milling. They selected the vibration features that correlate with the tool wear in the frequency domain and applied the Backpropagation Neural Network to the features to classify the tool wear as shown in Fig. 22(b).
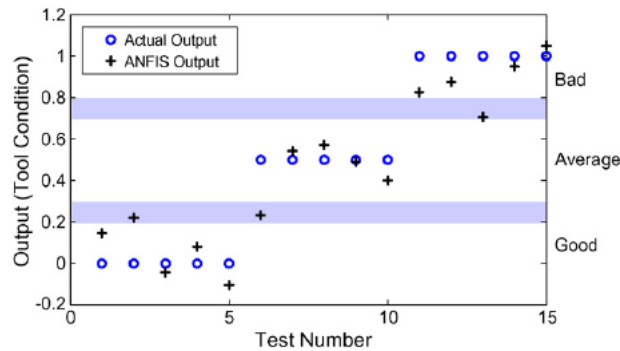
(a)
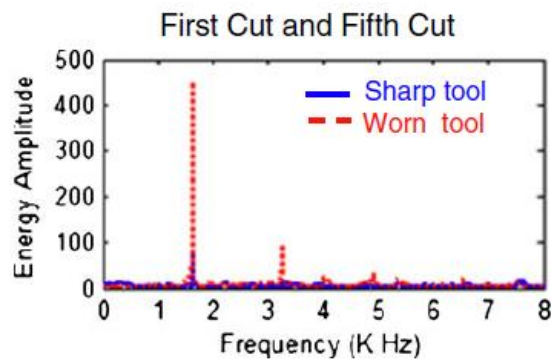
(b)

Figure 22. Tool wear classifications(a)results of the neuro-fuzzy method for tool state[8], (b)workpiece vibration signals for sharp and worn tool test in the frequency domain[64].

Ren et al. [65] applied a Type-2 fuzzy tool to the AE signal features and estimated tool wear in micro-milling.

Zhu et al. [66] measured Holder Exponent(HE) which represents the amount of singularity in the cutting force signal in micro-milling as shown in Fig. 23(a). They showed that the probability distributions of HE are different depending on the tool condition and it can be used as a tool wear classifier.
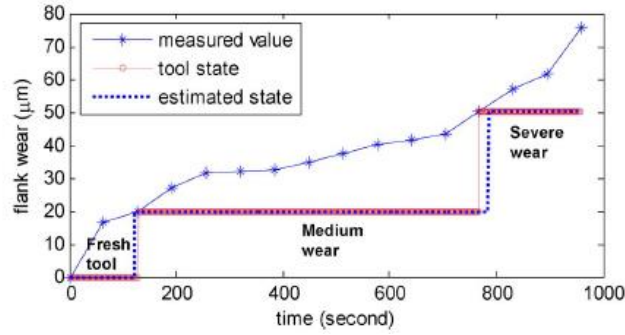
(a)
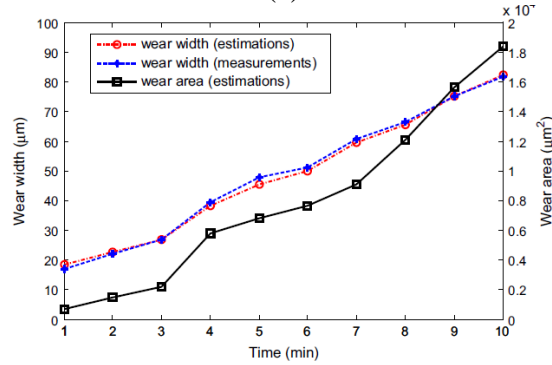
(b)

Figure 23. Online tool wear estimation and classifications(a)online state estimation of test[66], (b)tool wear width and area progression with time[11].

Zhu and Yu [11] proposed a tool wear surface area monitoring method using the image processing in micro-milling as shown in Fig 23(b). Most of these methods are indirect methods. Many studies have been done on the direct tool wear measuring method. But, it is mostly done by using a microscope or SEM to get an image of the tool and measure the tool wear through the image. In most cases, the measured values from the direct methods are used to verify the values from the indirect methods.

This section describes how to monitor tool conditions, including tool wear. The tool condition is monitored in a direct and indirect way. Unlike the direct method, the indirect method determines the state of the tool wear by applying signal processing algorithm to the measurement signals. So far, the contents that are related to tool wear have been explained. The following sections describe the terms for understanding this study, UCT, MCT, and cutting edge radius.

Section 4. Uncut chip thickness

The UCT is one of the major parameters of the cutting process. For turning, the UCT is equal to the depth of cut. For milling, the UCT is different from the depth of cut and it can be adjusted by changing the spindle speed and feedrate. It is important from the aspect of machining efficiency that the cutting time should be minimized. Especially, in the milling process, the tool cuts the workpiece while rotating and moving forward, simultaneously. The feedrate and spindle speed should be selected to minimize the operating time as much as possible. The UCT is also related to the chip load, which is directly related to the cutting force. If the UCT becomes thicker, the cutting force increases. If the thickness is too large at low cutting speeds, the tool will break due to the large cutting force. The UCT can be calculated by considering the path of the cutting edge during a cutting process.

In milling, the path of the cutting edge follows the trochoidal path as it translates and rotates at the same time. Thus, when cutting the workpiece, the UCT changes while the cutting edge passes. When the cutting edge enters the workpiece, it has a thickness of zero. But, in the middle of the tooth pass, the UCT becomes maximum. And, when the cutting edge exits from the workpiece, the UCT becomes zero again. So, the sine curve is usually used to model the UCT. But, it is not a perfect circle form because of the translation motion. The sine curve is applied to the model to simplify the calculation. This assumption can be applied in conventional milling.

The first flute will cut the thicker UCT than the original thickness. And the second flute will cut the thinner UCT. This would change the amount of the chip load in each flute. The larger cutting force will be applied on the first flute and the smaller cutting force will be applied on the other flute. This means that first cutting edge would

wear out more and the other cutting edge would wear out less during the same cutting time period. This would change the dynamic characteristics of the cutting operation.
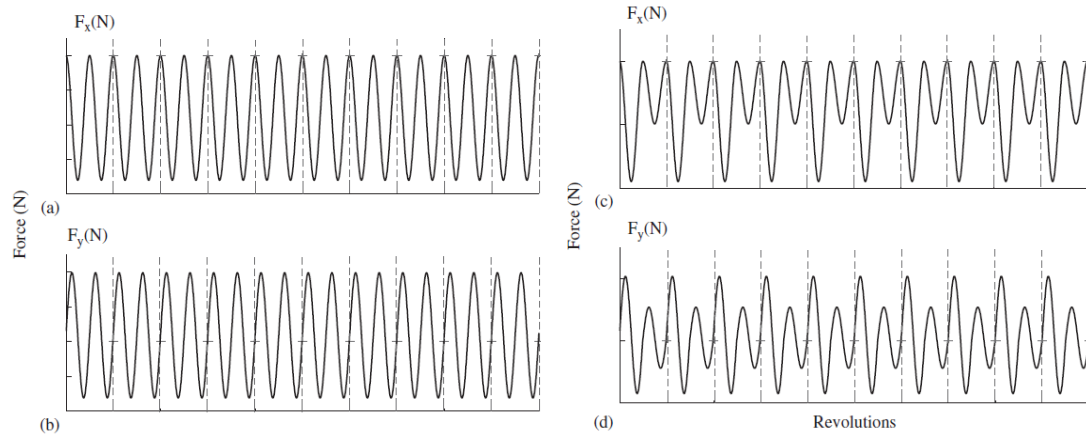
Figure 24. Simulation of the forces using conventional milling force model for 6 mm/flute feed rate without runout ((a) and (b)) and with 2 um runout ((c) and (d))[67]

This section describes the definition of UCT and the trochoidal path of the cutting tooth. Also, the influence of the UCT on the cutting process, such as cutting force, is explained.

In micro-milling, the UCT and the MCT are closely related since the chip formation depends on them. In the next section, the relationship between the UCT and the MCT is described.

Section 5. Minimum chip thickness

The MCT is better known as the MCT effect. This is one of the size effects generated as the size of the tool is reduced from macro to micro size, and it explains the cutting mechanism of micro-milling. The MCT refers to the smallest thickness that a round cutting edge can cut as shown in Fig. 25.

The MCT effect explains how the round edge behaves in the cutting process.

For example, if the UCT is larger than the MCT, then the cutting edge will cut the workpiece. This cutting mechanism is dominated by the shearing cutting regime. And if the UCT is smaller than the MCT, the cutting will not occur due to the sliding of the cutting edge on the cutting surface. This cutting mechanism is dominated by the ploughing cutting regime.

(a)   (b)

(c)
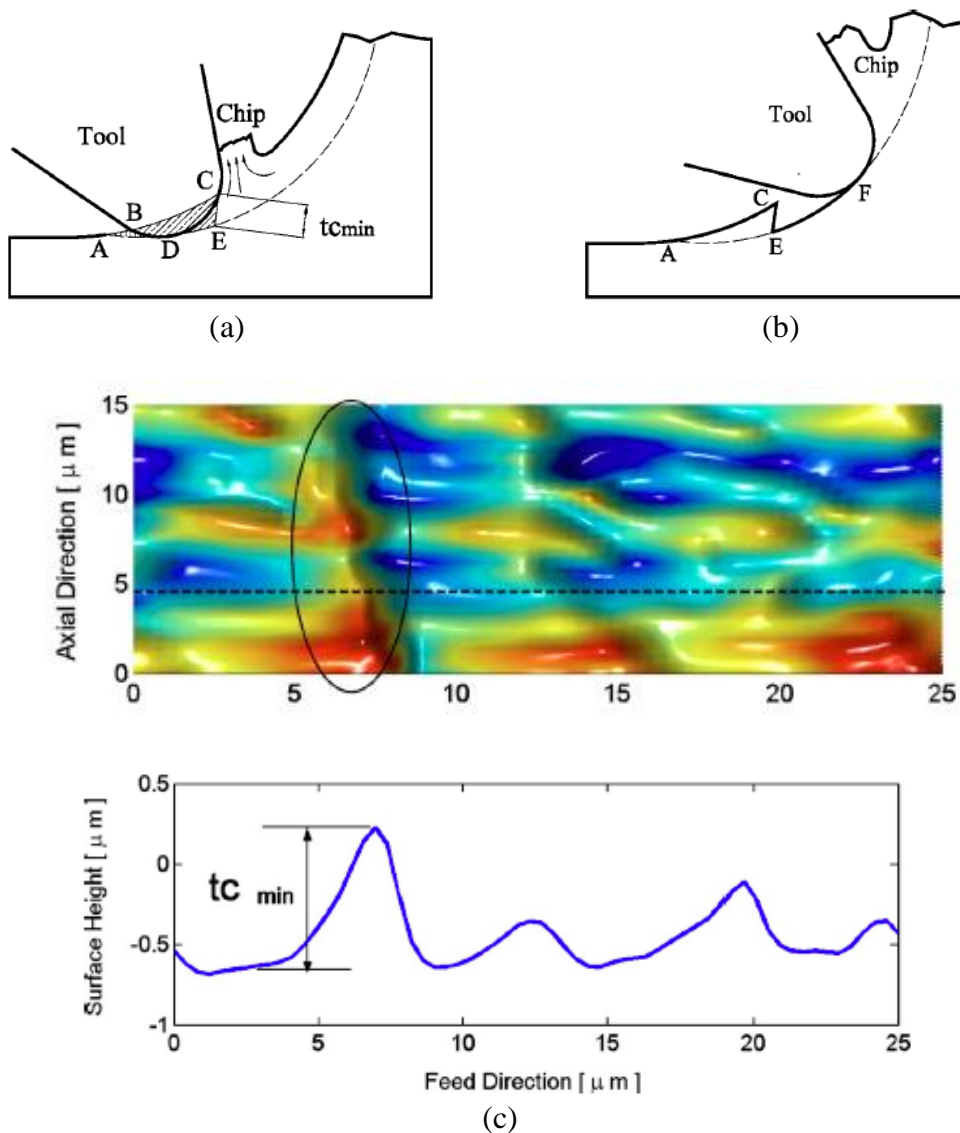
Figure 25. Minimum chip thickness (a)&(b)Sidewall surface generation taking into account the minimum chip thickness effect, (c)extraction of the MCT (tc_{min})from the surface profile measured by Wyko optical profiler[68].

34

The MCT has had a significant impact on micro-milling studies in particular. Many of the theories applied to conventional milling cannot be applied to micro-milling. One of these theories is the Merchant's Circle model which includes cutting, shearing, and friction. This theory assumes that the cutting edge is sharp. However, in micro-milling, the size of the cutting edge and the UCT become smaller so that they become comparable to each other.

Therefore, the cutting edge can not be assumed to be sharp anymore. Instead, it is assumed to be round having the radius which is called the cutting edge radius. The cutting edge radius will be explained more in the following section.

Many studies have been done to estimate the MCT. The MCT is not a thickness that can be adjusted with a feedrate, a spindle speed or other control parameters, but varies depending on how round the cutting edge is or what the cutting material is. The roundness of the cutting edge has a significant effect on the movement of the material that slides over the rounded edge surface when cutting the workpiece. It plays a crucial role in obtaining the MCT. The MCT can be estimated through experiments utilizing different materials and tools with different cutting edges, since how the material moves along the round edge depends on the cutting material and the round cutting edge. The movement of the material at the rounded surface has been studied through FEM simulations and it has been found that the material is divided at the stagnation point into two parts: a material that will be removed as a chip and a material that remains on the workpiece. The position of the stagnation point is similar to the MCT. These simulations are also closely related with the chip formation mechanism.

In order to find MCT value, many experiments have been done. The MCT -to-edge radius ratio was predicted between 0.205 and 0.43 in the previous research on

35

MCT [69]. L'Vov [70] estimated the MCT-to-edge radius ratio to 0.298 from the cutting experiments with a cemented carbide tool and the SAE1045 workpiece. Also, Yuan et al. [17] conducted the ultraprecision lathe experiments to find the ratio by cutting an aluminum alloy with a diamond tool. The measured cutting edge radius is 0.2~0.6 μm and the MCT is 0.05~0.2 μm indicating that the ratio is between 0.25~0.33. And, from the FE simulation by Vogler et al. [71], the ratio was 0.14~0.25 for the pearlite material and 0.29~0.43 for the ferrite material.

In this section, the definition of MCT is described. Then, the explanations are made on the efforts that have been made to investigate the MCT with experimental approaches as well as theoretical. Since the MCT can be approximated from the cutting edge radius, it is explained more thoroughly in the next section.

Section 6. Cutting edge radius

Generally, the sharpness of a rounded cutting edge is classified by its radius. Unfortunately, it has been measured in many different ways without defined measuring standards. The cutting edge radius can be obtained by measuring the radius of a circle drawn on a round cutting edge. In particular, the cutting edge radius is a measure of the cutting edge wear. To measure the cutting edge radius, an image of the edge is taken by a microscope or SEM and a circle is drawn on the edge. And then, the radius of the circle is measured. However, there is a drawback to this measurement method. Since the round part of the cutting edge does not exactly match the perfect circle, a measurement error occurs. Since the cutting edge is not always round, it also causes errors in drawing the circle. The cutting edge of the new tools can be seen clearly. However, for the used tools, the workpiece material or the chips can be attached to the

cutting edges after the cutting. In this case, when the circle is drawn on it, the edge radius can be bigger or smaller than the actual value. Also, the tool should be fixed at the position where the bottom of the tool can be exactly parallel with the microscope field of view. But, it is not easy to make them parallel since the height difference between the lowest part and the highest part on the bottom of the tool could be smaller than tens of microns. Therefore, it is also difficult to keep the same depth of focus which could change the size of the circle.

Efforts have been made to increase the accuracy of drawing the circle [72]. The method is as follows. From the bottom view of the tool, the flank and crater surfaces appear as two straight lines. Draw a straight line along the flank and crater surfaces and draw a circle that meets these two lines and a point at the end of the cutting edge that meets with the bisector of an angle between two lines. This process also has some error because the lines are drawn by looking at the flank and crater and the dot is picked by looking at the cutting edge. This method was chosen in this paper because it is more systematic than the conventional methods.

The UCT, MCT, and cutting edge radius are closely related to the chip formation. In micro-milling, when the MCT is above the UCT, the cutting occurs with generating a chip per cutting tooth pass. But, when the MCT is less than the UCT, the cutting edge will slip on the workpiece without generating one chip per cutting tooth pass.

This section describes what the cutting edge radius is and how to measure it. Also briefly describes the effect of the relationship between the UCT, MCT and cutting edge radius on chip formation. The chip formation and chip control are described in the next two sections.

Section 7. Chip formation

Understanding the chip formation process and chip control is important in all cutting processes. The reason for this is that it is possible to design the optimal tool or to find the optimum machining conditions based on many phenomena including the friction, force, etc. acting on the tool during chip formation. Chip control is the study of chip shape and chip disposal method after the chip formation. It has been studied to minimize the influence of chip on process quality.

Chip formation research started between the 1930's and 1950's by Piispanen and Merchant. In Piispanen's chip formation model, the chip is described as the stacked card being pushed forward by the rake surface of the tool as shown in Fig. 26(a)[73] [74]. Merchant proved this model both theoretically and experimentally[75]. And Merchant's force diagram is still very useful today. It is shown in Fig. 26(b).

(a)   (b)
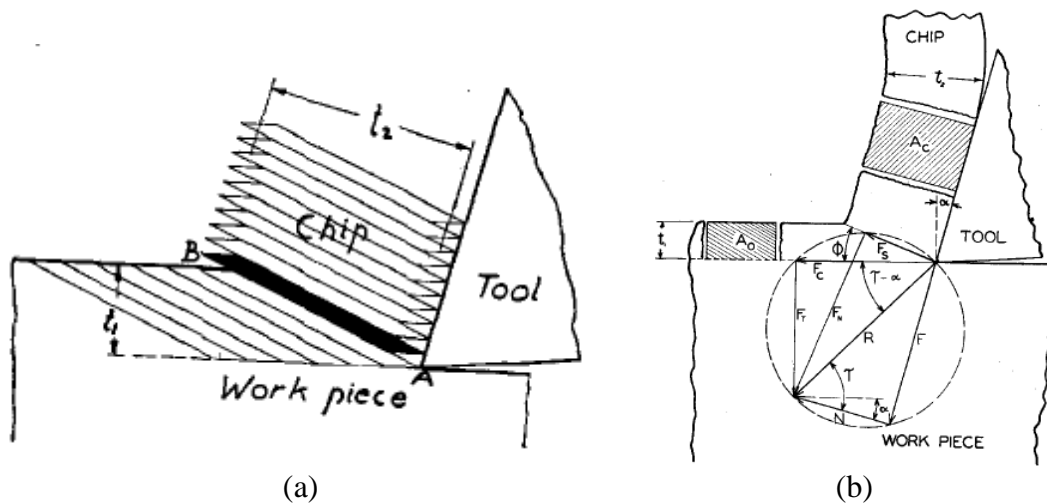
Figure 26. Early chip formation studies(a)Chip formation with the lamellas[73], (b)Merchant's force diagram showing relationships between components[75].

Between the 1950's and 1970's, not many studies were done on the chip formation. Connolly and Rubenstein[76] proposed a new lower boundary of the

primary deformation zone in orthogonal cutting and discussed the stresses acting on the new boundary and the influence of the finite radius of curvature of the cutting edge on the chip formation.

From the 1970s to the 1980s, the research on the chip formation was revitalized by the rapid development of SEM since the SEM was first commercialized in 1965. Ramalingam and Bell[77] realized that the development of SEM would enable a lot of data collection regarding chip formation. Doyle et al.[78] conducted an investigation on the friction between the chip and rake face in two conditions with and without air. They found that oxygen tends to increase the adhesion and friction. Hastings et al. [79] developed a theory that can predict the chip geometry and the cutting forces by taking into account the material properties such as the temperature and strain-rate of the workpiece. Komanduri and Brown [80] conducted cutting tests to investigate the mechanics of chip segmentation by using the high speed camera. They found that the chip segmentation occurs due to the stick-slip friction on the rake face. Lee [81] compared the chip formation experiments for three different materials. The continuous chips are generated from the two materials and the other one generated the segmented chip. Lee found that the conditions for discontinuous chip formation are low strain and strain rate hardening capability.

In addition, the finite element method developed in the aerospace industry in 1956 began to be applied to the metal cutting process in the 1970s. The finite element method has a great influence on the research on the metal cutting process. Tay et al. [82] applied 2-D FEM to the orthogonal machining with a continuous chip and obtained the temperature distribution in the primary and secondary zone. Strenkowski and Carroll [83] conducted the orthogonal metal cutting simulation using the finite element method

and applied Lagrangian formulation for the strain condition as shown in Fig. 27(a). Chip formation was simulated and the influence of the value of chip separation criterion on the chip geometry, tool forces, and the residual stress is investigated. Strenkowski and Moon [84] applied the Eulerian FEM to the orthogonal metal cutting simulation to predict the chip geometry and the temperature distribution in the workpiece, chip, and tool as shown in Fig. 27(b). They compared the Lagrangian and the Eulerian approach to show that the latter approach is better for the metal cutting simulation. Ceretti et al. [85] applied the FE code DEFORM 2D to simulate the continuous and the segmented chip formation in orthogonal cutting. The influence of cutting speed, tool geometry, and depth of cut on the cutting force, temperature etc. are investigated for the continuous chip flow. And, the segmented chip flow is also studied to see how the discontinuous chips are generated.

| (a) | (b) |
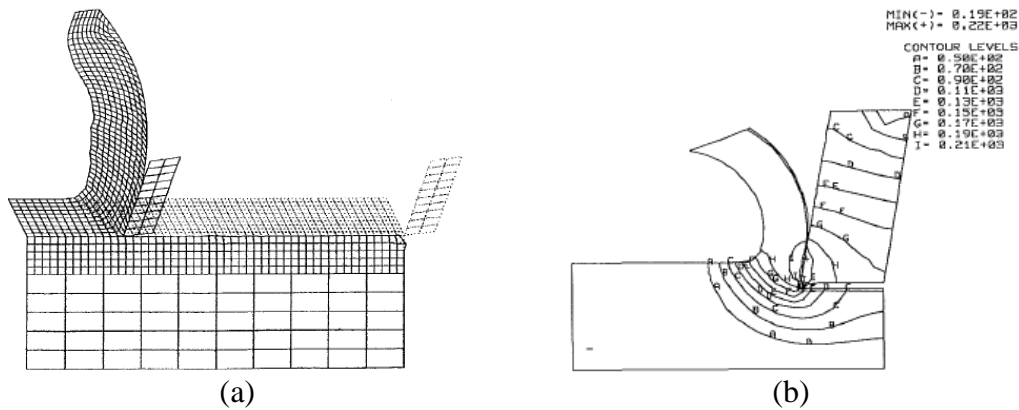
Figure 27. Numerical simulation of chip formation(a)Chip formation for final position of tool[83], (b)contours of predicted workpiece and tool termperatures[84]

In the 2000s, as interest in micro-machining increased, research on chip formation in micro-machining began. The theories that were not applied in conventional machinings, such as the size effect that arise due to the small size of the tool, were applied. Theories and experiments have been studied together, and finite

element method have been applied to the parts that are difficult to know from the experiments.

Kim et al. [86] conducted an experimental investigation on the chip formation in micro-milling as shown in Fig. 28. They concluded that the chip may not form when the feed per tooth is comparable to the cutting edge radius or when the stiffness of the system is small.

(a)   (b)
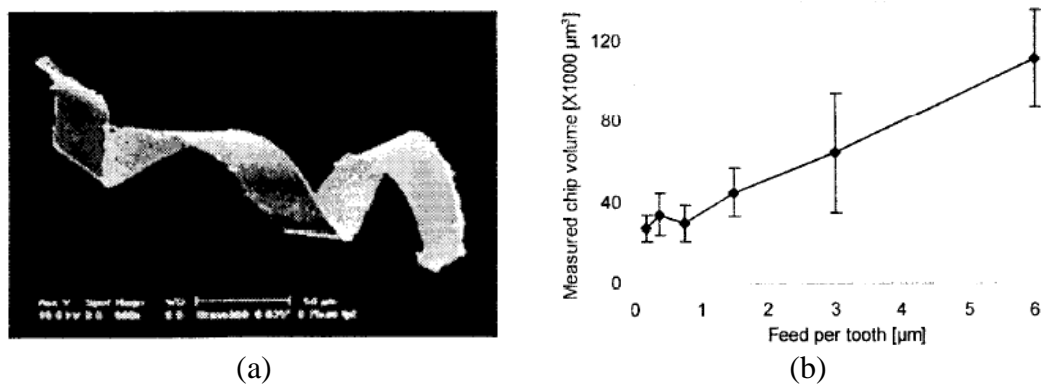
Figure 28. Experimental investigation on chip formation in micro-milling(a)Picture of a chip from micro-milling, (b)measured chip volume versus feed per tooth[86].

Kim et al. [15] studied the chip formation and cutting forces in micro-milling. They found that the chip may not be generated when the feed per tooth is smaller than the MCT due to the MCT effect. And, the upper and lower boundary of the appropriate feed per tooth for a given size tool is defined. The upper boundary guarantees stable machining with the consecutive chip formation and the lower boundary does not guarantees stable machining with the intermittent chip formation.

Özel et al.[87] predicted MCT through applying the Johnson-Cook(J-C) model to the analytical chip formation model and conducted FEM simulation based on the rigid-plastic deformations to predict the chip formation in micro-milling as shown in Fig. 29.

(a)   (b)
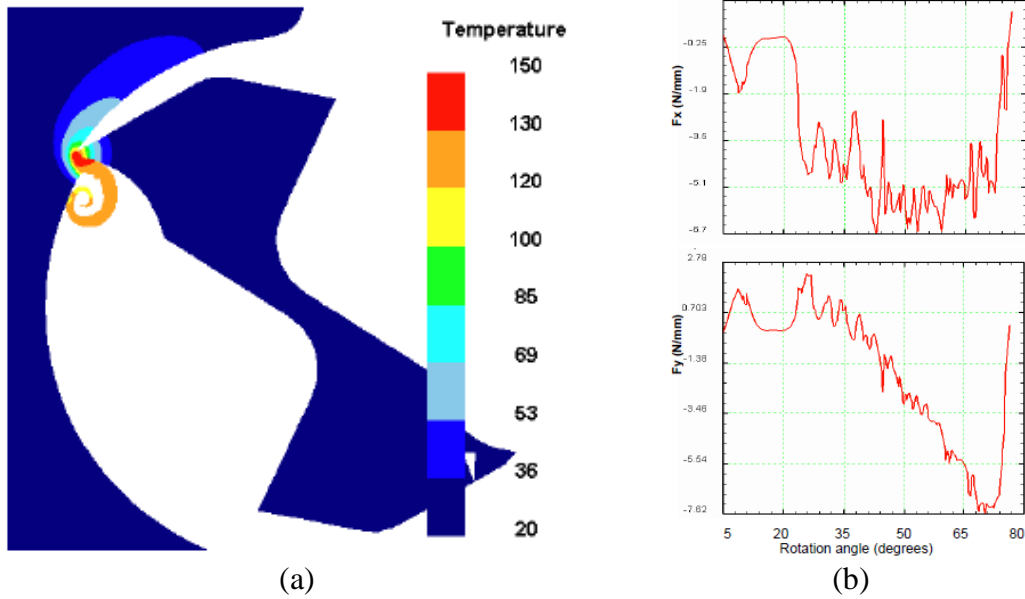
Figure 29. Finite element simulation and cutting force in micro-milling(a)Finite element simulation of micro-milling, (b)predicted forces in micro-milling[87]

Jin and Altintas [88] developed a slip-line field model of micro-cutting process to predict the total cutting forces as shown in Fig. 30. They applied the J-C model and the friction at the tool-chip contact to include the strain, strain-rate and temperature effects on the plastic deformation zones along the round edge surface. And validated through the cutting test.

(a)   (b)
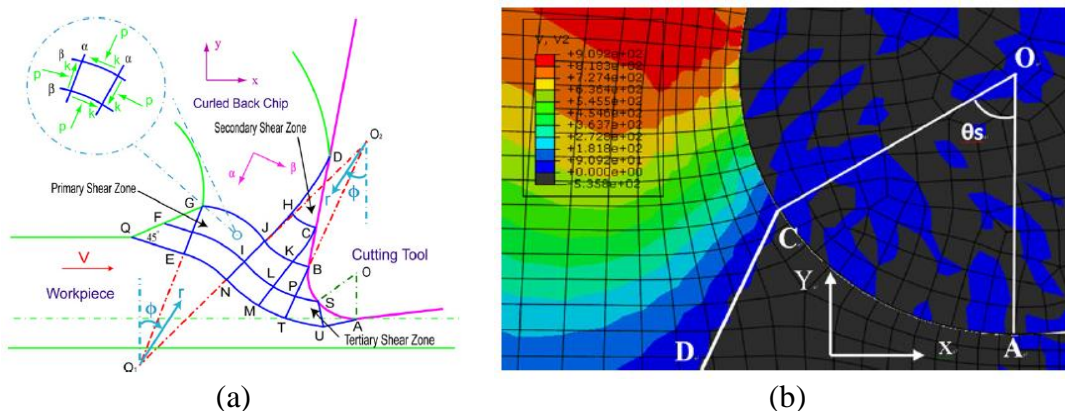
Figure 30.Slip-line field model(a) Slip-line field model of the orthogonal micro-cutting process with a round tool edge: primary shear zone [GJBTNEQ], secondary shear zone [BCDHJK], tertiary shear zone [BSAUTP], (b)material separation in the tertiary zone[88].

Thepsonthi and Özel [9] investigated the chip flow and the tool wear through the 3-D FEM simulation and the experiments in micro-endmilling of Ti-6Al-4V titanium alloy as shown in Fig. 31. Chip flow and shapes are compared with the chips obtained from the experiment, and the predicted tool wear is also compared with the experiment.
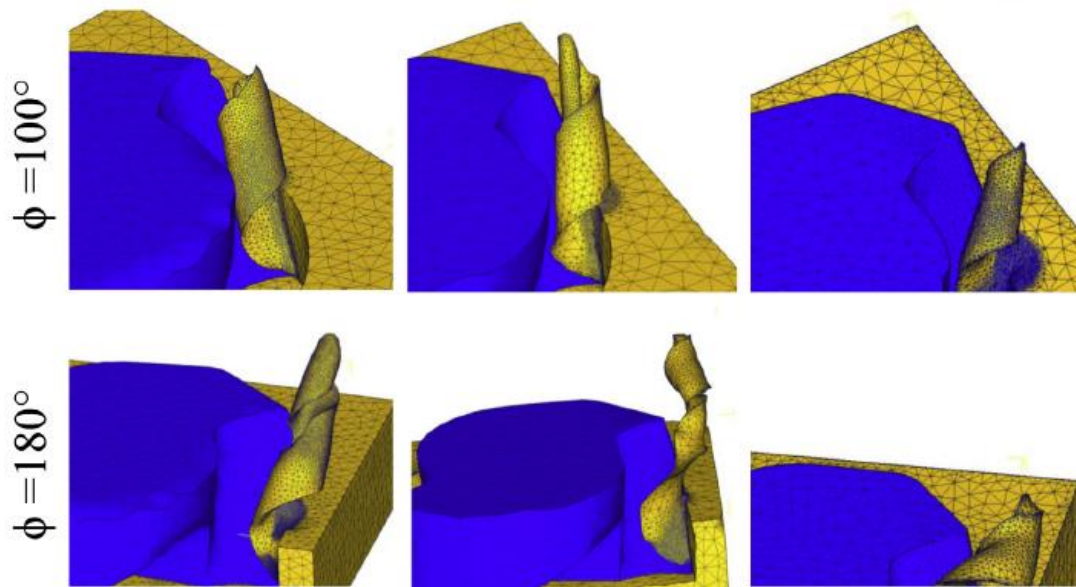
(a)
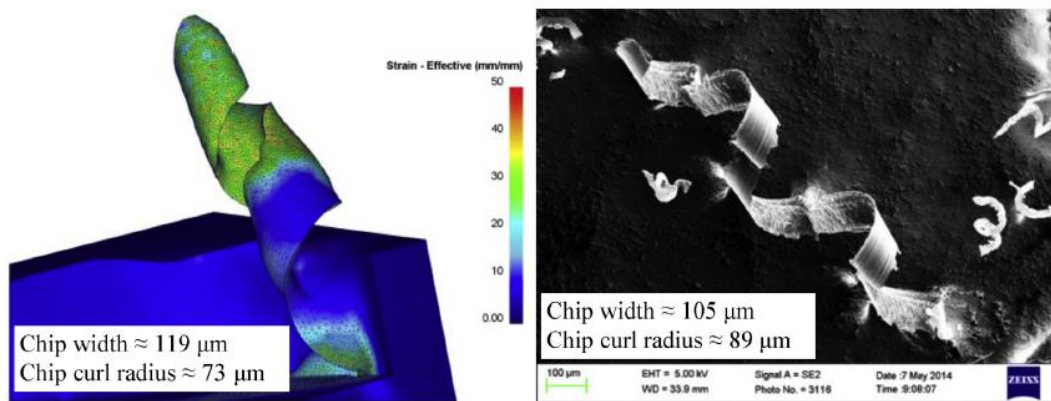
(b)

Figure 31. 3-D chips from FEM simulation vs. experiment(a)Predicted 3-D chip formation and chip flow, (b)Comparison of predicted and measured 3-D chip formation and chip flow for full-immersion micro-end milling [32]

As described in this section, research on chip formation plays an important role in understanding the cutting mechanism. Continuous research through simulations or experiments is needed to understand a variety of phenomena that occur between the cutting edge and the workpiece material.

The behavior of the chips beyond the chip formation is also an important issue since the chips affect on the machining quality. In the next section, the behavior of the chip after the chip formation is explained with the chip control studies.

Section 9. Chip control

The area of chip control has been studied for more than a hundred years in mechanical machining industry in order to improve the efficiency of the metal cutting process. The surface finish, machining accuracy, and tool-life are easily affected by the chip formation process. Thus, the chip control research such as chip breaking and chip evacuating methods have been done significantly [27]. As a major part of the chip control, the prediction of chip geometry corresponding to the tool design is necessary prior to the chip break and chip evacuation applications [89]. The chip geometry derived in [90, 91] is the most widely accepted analytical model which is composed of three geometrical parameters; chip flow angle, side-curl, and up-curl. Also, another geometrical analysis of 3-D helical chip is conducted in [92]. They developed 3-D helical chip geometry by finding the helical axis, radius, and pitch. In [93], the chip is analytically modeled as a 3-D spiral. These chip models are derived based on the orthogonal cutting. In [94], 3-D geometry of a chip is obtained based on [91, 95] and the model is compared to the chips from the cutting test.

But, only a few research studies has been published predicting the chip form in

micro-endmilling. In [96], the chip formation process with the size effect in micro-milling is discussed and the chip form is validated through examining the chips from the cutting test. The chip form is predicted by FEM and compared to the chips from micro-endmilling in [9, 97].

As shown in Fig. 32, the 3-D geometry of a chip derived in [91] is composed of three components; radius (ρ), pitch (p) and athe xis of a helix(θ) in terms of rathe dius of side-curl (ρ_s), up-curl (ρ_u) and chip flow angle (η) as Eq. (4)&(5)&(6).

$$\rho = \sqrt{\frac{1 - sin^2\eta\ cos^2\ \theta}{\left(\frac{cos\ \eta}{\rho_u}\right)^2 + \left(\frac{1}{\rho_s}\right)^2}} \qquad (4)$$

$$p = \frac{2\pi\rho\ sin\ \eta\ cos\theta}{\sqrt{1 - sin^2\ \eta\ cos^2\ \theta}} \qquad (5)$$

$$tan\theta = \frac{\rho_u}{\rho_s\ cos\ \eta} \qquad (6)$$

(a)

(b)

(c)

(d)
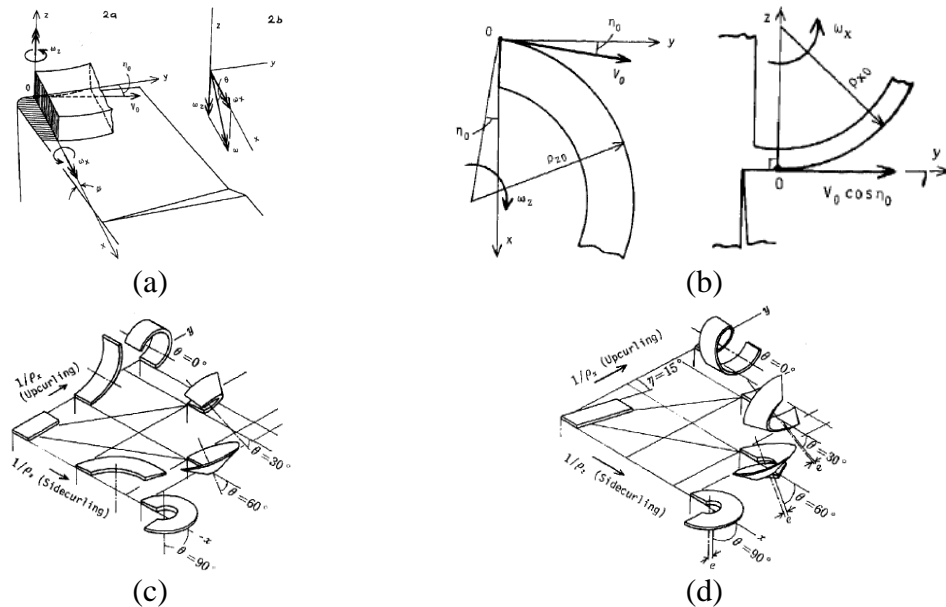
Figure 32. Chip shape formation (a)Motion of chip, (b)sidecurling (left) & upcurling (right), (c)variation of chip form by upcurling and sidecurling when the chip flow angle is 0(deg), (d)variation of chip form by upcurling and sidecurling when the chip flow angle is 15(deg).

45

The sidecurl, upcurl and the chip flow angle of a 3-D chip are as shown in Fig. 33. The chip curls upwards with respect to the axis of the upcurl of the x-axis and the chip curls to the side with respect to the z-axis which is the axis of the sidecurl. The angular velocity of the upcurl ω_x and the anglular velocity of the sidecurl ω_z generate the resultant angular velocity ω which is on the axis of the helical chip.

Figure 33. Comparison between the actual chips and the animated chips for different cutting conditions[94].

The 3-D chip geometry in oblique machining can be expressed in the Cartesian coordinate system as following equations [94]: where δ is the tool helix angle($\delta = \frac{\pi}{2} - \theta$), $t \in [0,2\pi)$ is used to determine the number of chips helix turns.

$$x = -\rho \cos \delta \cos t$$

$$y = -\rho \cos \delta \sin t$$

$$z = \rho \sin \delta + \frac{p}{2\pi} t$$

(7)

This section describes how to control chip movement after chip formation. Chip control is also an important part because it can affect machining quality if the chip remains on the workpiece.

The next section covers the microstructure of the workpiece, another factor that affects machining. Especially, the influence of the microstructure of workpiece material on the cutting force is explained.

Section 9. Microstructure of workpiece material

In conventional machining, the workpiece material can be assumed as isotropy. However, the size of the grain becomes comparable to the size of the cutting edge of the tool in the micro-machining. And each grain has different orientations with different material properties such as Young's modulus[98]. Therefore, the workpiece material cannot be considered as isotropy but anisotropy.

In Fig. 34, it compares the schematic diagram of the grains and the grain boundaries to the picture of pearlite steel grain and grain boundaries. Every grain has a different orientation. And the shape of the grains is all different.

47
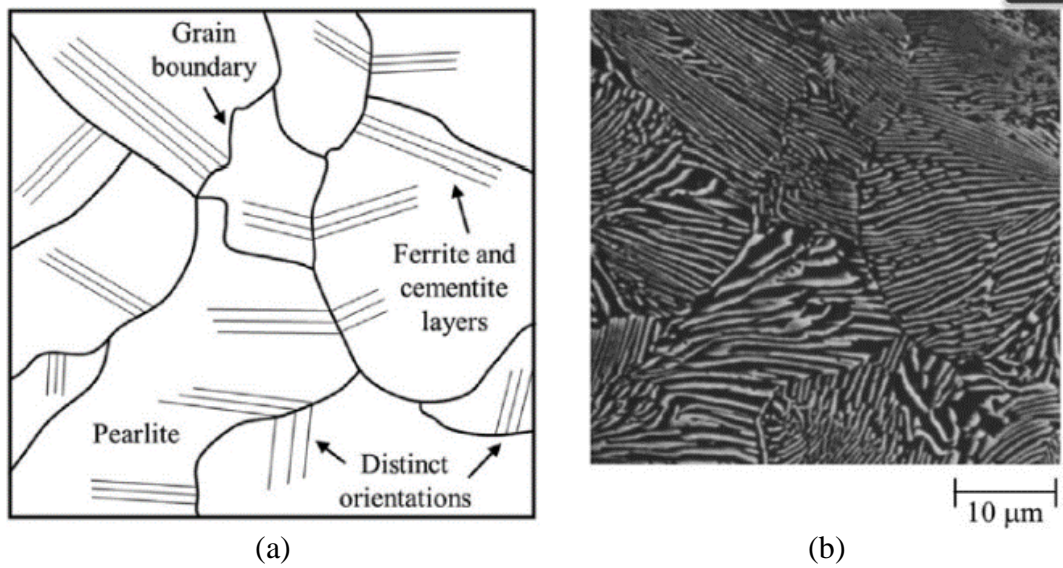
Figure 34. Microstructure of pearlite steel(a)schematic diagram of grains and grain boundaries, (b)pearlite steel grain and grain boundaries.

The influence of the grains on the micro-machining has been investigated. It affects the cutting force and the surface roughness which are related to the quality of the machining process.

The change in the cutting force due to the multi-phase grains including graphite, ferrite, and pearlite is investigated by modeling the workpiece material and by conducting the cutting force measuring experiment[99] as shown in Fig. 35.
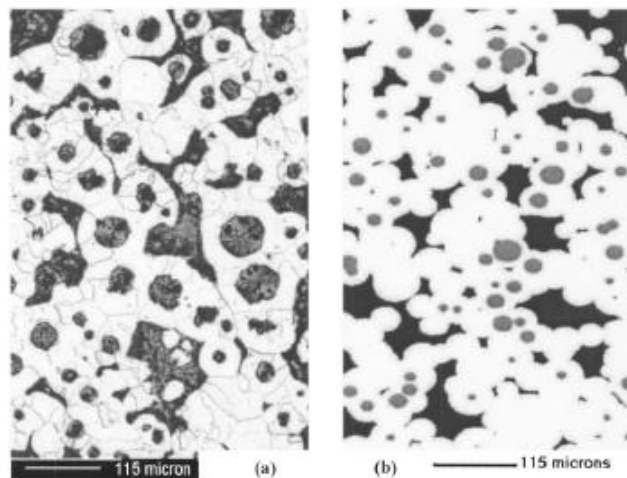
Figure 35. Microstructure of ferritic ductile iron(a)actual, and (b)simulated [99]

The result shows that the wavelength of the dominant vibration frequency in the cutting force signal occurred due to cutting the grains located on the cutting surface is highly close to the average size of the grains. And the cutting force is dependent on the UCT which determines the chip load as shown in Fig. 36.
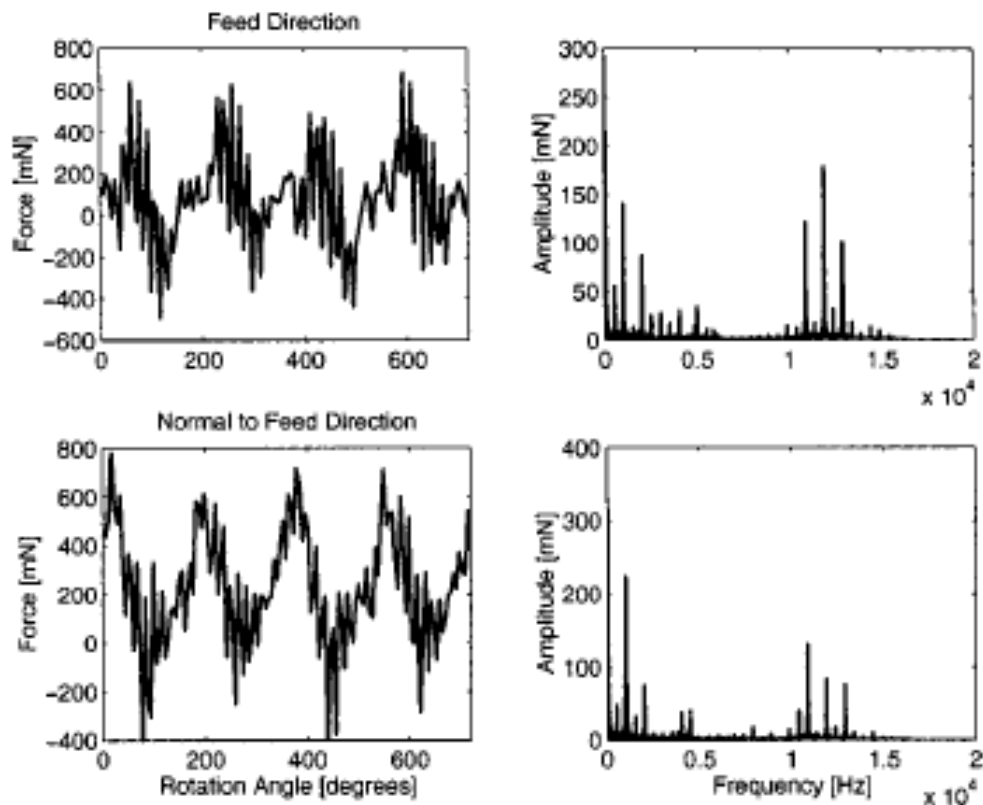
Figure 36. Experimental pearlitic ductile iron data (high feed)[99].

In this section, the influence of the microstructure on the cutting process is described. The size of the grains would affect the cutting force and the surface roughness, etc.

In the next section, the structural dynamics in the machining process is explained.

Section 10. Chatter

Chatter in the machining process has been studied for several decades. Tobias et al. [100] and Tlusty et al. [101] developed the chatter theory for the orthogonal cutting process by identifying the relationship between the tool and the cutting process as a structural dynamic function. Merritt [102] introduced the Nyquist stability criterion to the machine-tool system to find the chatter-free cutting conditions. Sridhar et al. [103, 104] studied the theoretical approach to developing a general dynamic model of the milling process using a cutter without helix through the numerical computation method in the time domain and applied the model to predict the stability. Hanna et al. [105] introduced nonlinearity into the machine-tool structure dynamics. The average periodic coefficients are used in the dynamic milling equation by Opitz et al. [106] to predict chatter in milling. Tlusty et al. [107] studied chatter in turning and milling with the basic nonlinearity caused by the tool jumping behavior due to the large vibration. Tlusty et al. [108] also analyzed the unique vibration characteristics of milling compared to continuous cutting. And, the influence of the damping effect on the high-speed milling stability was studied in [109]. Minis et al. [110, 111] tried to apply the single point cutting chatter mechanism to milling operation utilizing Floquet's theorem and Fourier Series and conducted Nyquist stability analysis of chatter in milling. Altintas & Budak [112–114] proposed a new analytical method that is able to predict the stability lobes in milling without the numerical computation and verified through the experiments as shown in Fig. 37. Their method can be conducted by scanning the chatter frequency around the system modes of the machine-tool structure in milling.
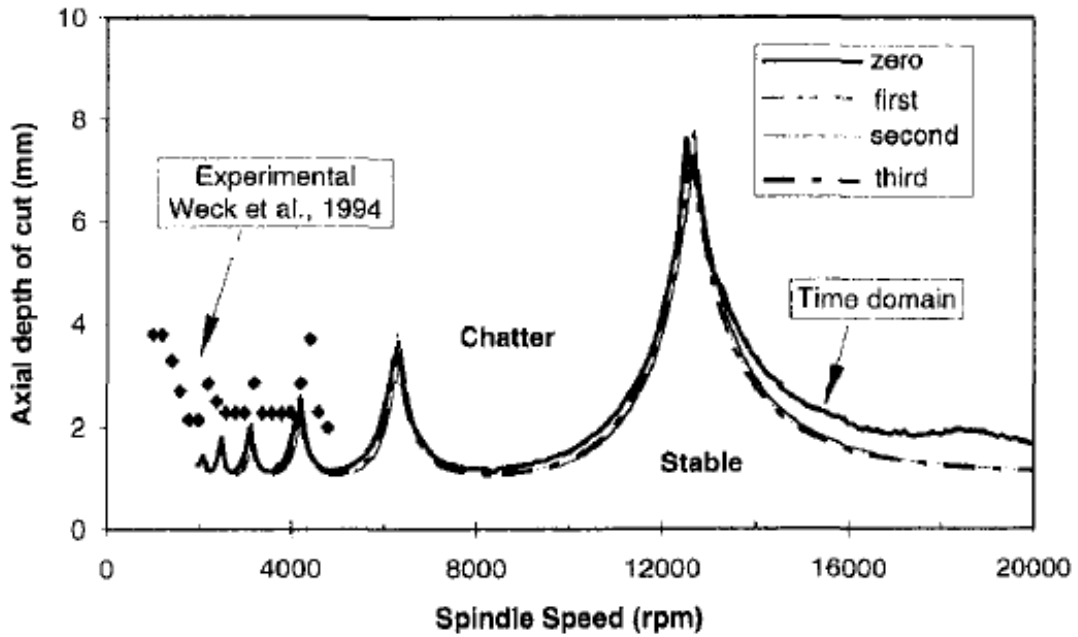
Figure 37. Analytical, simulation and experimental stability diagrams for a 2-DOF end milling system. (Workpiece material: aluminum, cutter; 3 flute, HSS end mill In half immersion up-mllllng)[113]

Altintas [115] also studied the three-dimensional chatter in milling using the same analytical method. After years of research on developing general chatter stability lobes in milling, it started to be expanded into more complicated machining cases. Bayly et al. [116] investigated the chatter stability in low radial immersion endmilling. Faassen et al. [117] proposed the stability prediction method that takes into account the effects of varying spindle speed to the cutting process and the machine dynamics of milling. Altintas et al. [118] compared the frequency domain and semi-discrete time domain solutions of the chatter stability of milling by showing the accuracy of the predicted stability lobes in low radial immersion milling.

The research on the dynamics and the stability of micro-milling started, as the interest in micro-machining increased. Filiz et al.[119, 120] developed an analytical micro-endmill dynamic model and solved numerically. The model is validated through

51

the finite element simulation and the frequency response experiment using a piezo actuator as a vibration source in order to conduct the modal analysis of the tool tip as shown in Fig. 38.
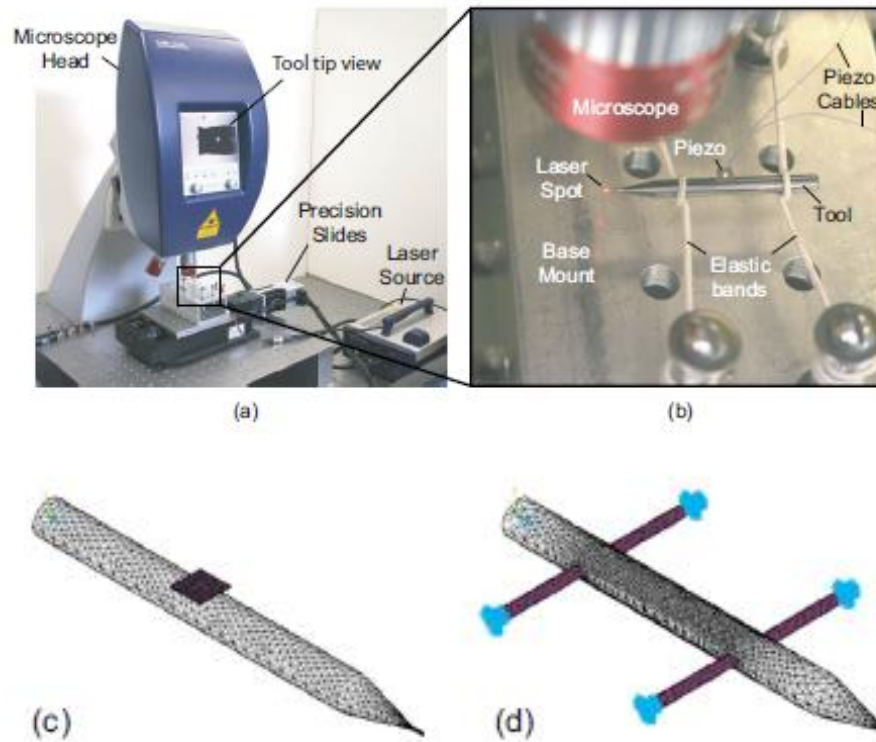
Figure 38. Frequency response simulation and experiment of micro-endmill(a)&(b)Experimental setup for free-free boundary conditions, (c)FE model with the piezoelectric element, (d)FE model with the elastic bands[120]

Malekian et al. [121] developed a micro-milling cutting force model considering the tool run-out, tool dynamics, ploughing effect and the elastic material recovery. The milling experiments are conducted in the chatter-free condition based on the stability analysis in order to verify the model. Park et al. [122] proposed a robust chatter stability model based on the dynamics of the micro-milling tool and emphasized the importance of the process damping in the stability of micro-milling operations as shown in Fig. 39(a). The nonlinearity in micro-milling is applied to the chatter stability

model and the effect of the tool run-out to the stability lobes is investigated by Afazov

et al. [123] as shown in Fig. 39(b).

(a)

(b)
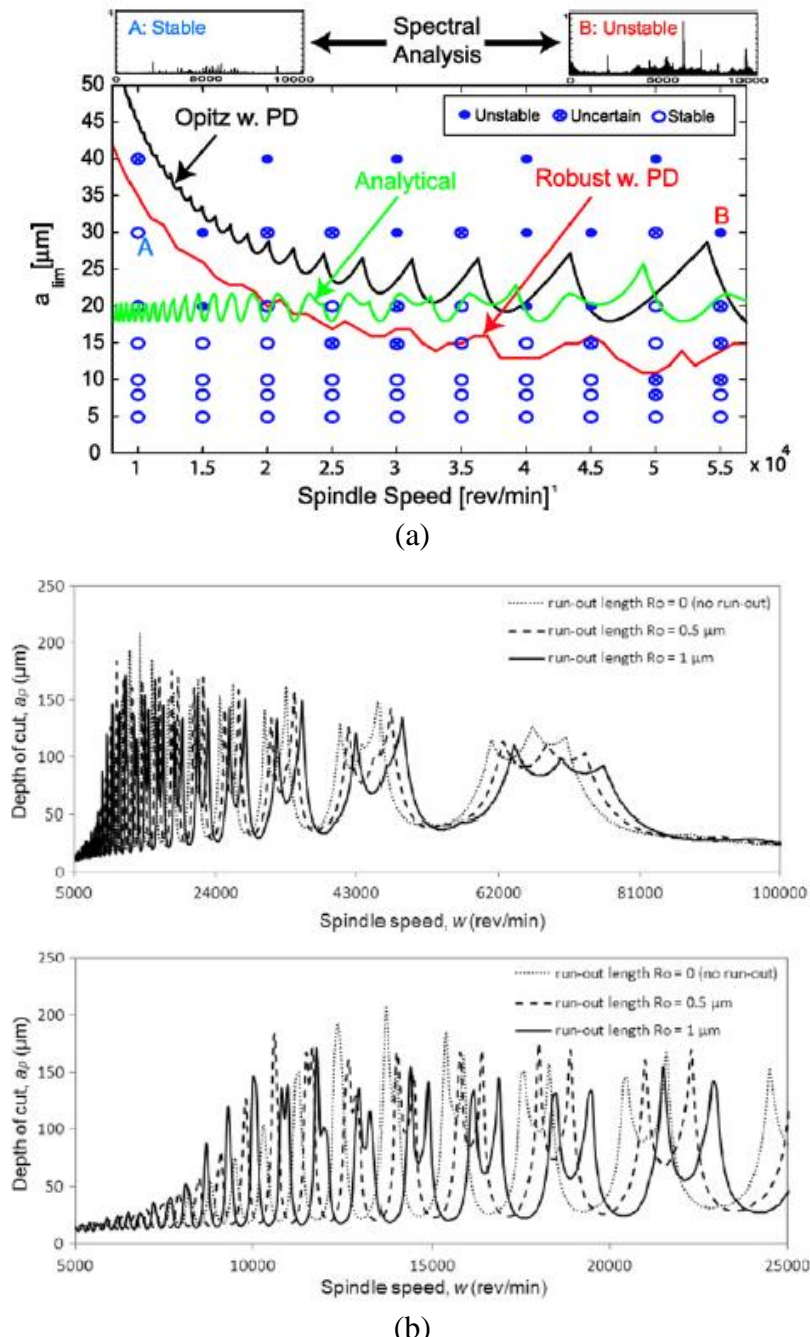
Figure 39. Chatter stability lobe with other effects(a)Comparison of stability lobes with conventional chatter, robust, analytical models and experiments at slotting of Al7075 with process damping[122], (b)run-out effect on the stability lobes at 8 um/tooth feedrate [123]

Jin et al. [124] identified the cutting force and the process damping coefficients in micro-milling and predicted the chatter stability using those coefficients. In order to evaluate the stability of the system, the stability lobes that can be obtained through the frequency response experiments of the tool is required. In the conventional milling, an accelerometer was attached to the tool tip and an impulse was applied by the impact hammer to perform the Frequency Response Function (FRF) test as shown in Fig. 40(a). However, it is impossible to attach the accelerometer to the small tool tip. Only a few alternative methods of stability evaluation have been introduced in the literature. Filiz et al. [120] attached the piezo actuator to the shank to vibrate the tool tip and measured the vibration using laser Dopler vibrometer. Park et al. [122] used receptance coupling method to calculate the transfer function by combining the structural dynamic transfer function of the shank using the impact hammer and the capacitance sensor and that of the tool tip from FEM modal simulation as shown in Fig. 40(b).

(a)

(b)
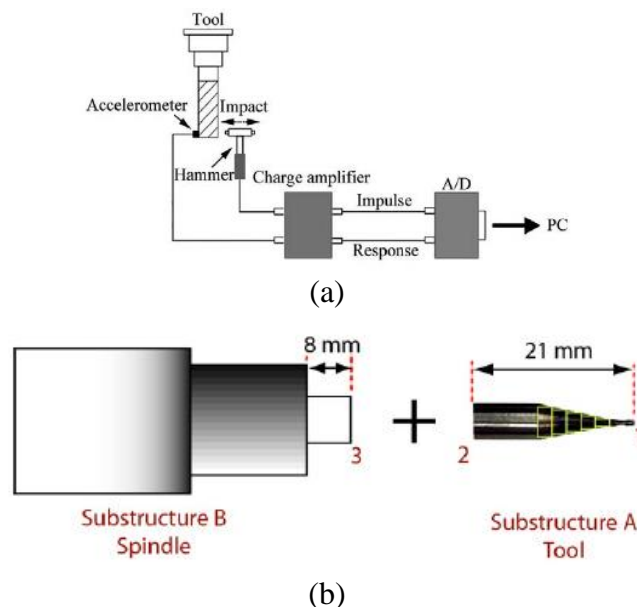
Figure 40. Existing methods of obtaining structural dynamic transfer function(a) Schematic diagram of hammer test[125], (b)receptance coupling of a spindle and an arbitrary end mill[122]

Section 11. Summary

The literature review describes existing research related to the research covered in this dissertation. The effect of tool wear on micromachining is emphasized. A lot of efforts were made to improve machining quality by predicting tool wear. In addition, machining stability has been an important research topic in micromachining field. Many chatter studies were performed by understanding the dynamic characteristics of the machine. In the next chapter, the chip production rate simulation in micro-endmilling process is conducted.

CHAPTER 3

CHIP PRODUCTION RATE SIMULATION

The simulation of the chip production rate in micro-endmilling process is conducted based on the trajectory of the cutting tooth of a micro-endmill and the MCT effect. The MCT can be approximated from the cutting edge radius and the UCT is determined from the feedrate and the spindle speed. The MCT effect describes the effect of the relationship between the MCT and the UCT on chip formation. If the UCT is larger than the MCT, one chip is created when the cutting tooth passes the workpiece, and when the MCT is larger than the UCT no chip is created when the cutting tooth passes the workpiece. Because, the cutting edge slides on the workpiece. Based on this MCT effect, a chip production rate simulation is conducted to see how chip formation changes when UCT is larger or smaller than MCT.

Section 1. Trochoidal path and uncut chip thickness

Our proposed tool wear monitoring system relies upon the UCT and the MCT effect. In this section, we develop the UCT model of the micro-endmilling. A trochoid can be generated by the combination of rotation and translation motion of a point on a circle. And, the path of the kth cutting tooth in the milling process follows the path as Fig. 41(a). The trochoidal path of the kth tooth edge is defined as Eq. (8)&(9), where x_k and y_k are the x and y position of kth cutting tooth, f is feedrate (mm/s), t is time (s), ω is cutting speed (rad/s), *n* is number of flutes, T_{cu} is UCT (mm), and f_{tooth} is feed per tooth (mm).
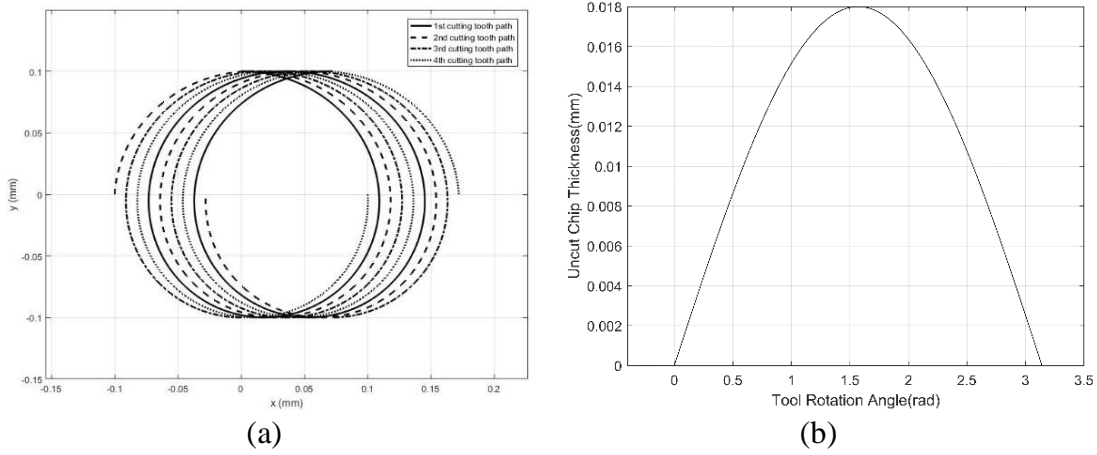
Figure 41.Uncut chip thickness(a) Trochoidal path of the cutting tooth for a 4-flute 200 μm micro-endmill, (b) UCT of a 2-flute 200 μm micro-endmill in at 6 mm/s feedrate and 10,000 rpm spindle speed [18]

$$x_k = ft + rsin\left(\omega t - \frac{2\pi}{n}(k-1)\right), \quad y_k = rcos\left(\omega t - \frac{2\pi}{n}(k-1)\right) \qquad (8)$$

$$T_{cu} = f_{tooth}\,sin(\omega t) \qquad (9)$$

Here, we are assuming that there is no chatter, tool deflection, and tool run-out, and the UCT varies from zero to feed per tooth as shown in Fig. 41(b).

In this section, the trochoidal path of a cutting tooth in milling process is simulated to determine the UCT. In the next section, the MCT is calculated prior to the chip production rate simulation.

Section 2. Minimum chip thickness

The MCT is directly related to the chip formation as it is considered as the major factor of the cutting mechanics of the tool-workpiece interface (whether shearing, ploughing, or elasto-plastic deformation is taking place). The possibility of shearing one chip per tooth pass or not depends on the tool condition, workpiece materials and

57

other machining parameters [126]. And, in order to simulate the chip production rate, the MCT has to be determined. As mentioned in chapter 2, the MCT(t_{cm}) to cutting edge radius (r_e) ratio can be approximated as 0.3 as given in Eq. (10).

$$t_{cm} \cong 0.3\, r_e \qquad\qquad (10)$$

Since the cutting edge radius is required to obtain the MCT, the cutting edge radius is measured in the next section.

Section 3. Cutting edge radius measurements

Generally, the sharpness of a rounded cutting edge is classified by its radius. Unfortunately, it has been measured in many different ways without any measuring standards. It can be affected by the resolution of the microscope or micro profilometer, the uncertainty from the user, and the circle fitting procedure onto the round edge. Wyen et al. [72] introduced a cutting edge radius measuring method to increase the reliability of the measured values. This measuring method is described in chapter 2.

To ensure that the acceptable cutting edge radius is applied to the MCT calculation in our simulation, Wyen's method was applied to measure the cutting edge radius of a 2-flute 200 μm micro-endmill from Performance Micro Tool (PMT) using Olympus MX50 microscope and the image processing shown in Fig. 42(a)&(b).

The MCT can be approximated from the cutting edge radius measurement. The following section describes the relationship between the ploughing effect and the chip production.
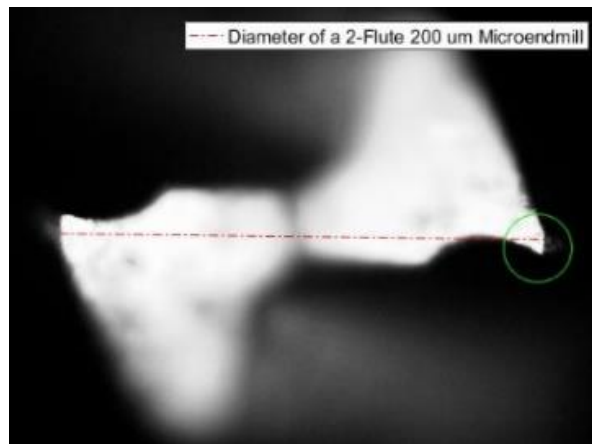
(a)
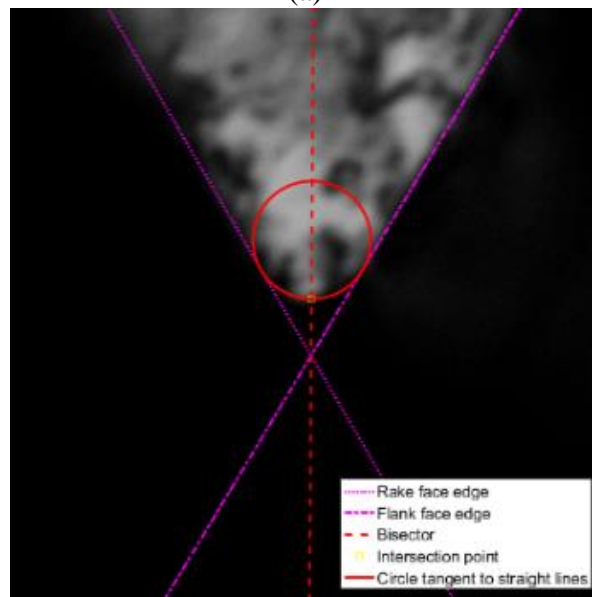
(b)

Figure 42. A 2-flute 200 μm micro-endmill with 2.01 μm cutting edge radius (a) 50× magnification, (b)150× magnification of the cutting edge on the right side in the tool image in (a).

Section 4. Ploughing effect

No chip will be generated if the UCT is less than the MCT. Assuming that the MCT does not change during a single tooth pass, only the UCT varies from zero to feed per tooth while cutting one tooth path. Therefore, regardless of whether the feed per tooth is larger or smaller than the MCT, shearing will not occur at the entering and leaving stage as shown in Fig. 43. And, the chip will not be generated until the accumulated feed per tooth become larger than the MCT, at which point shearing begins.

59
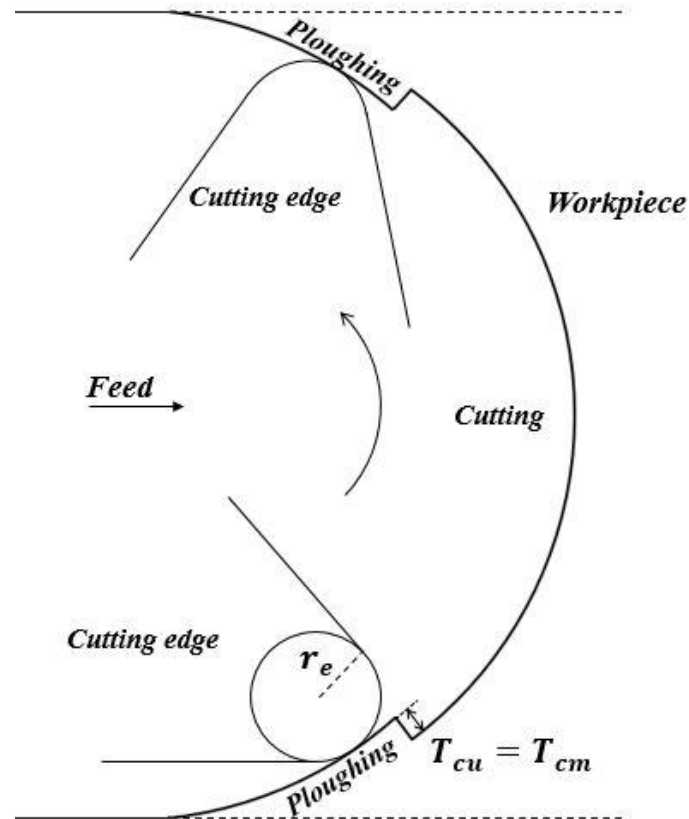
Figure 43. Ploughing effect in micro-endmilling [18]

Section 5. Chip production rate simulation

In order to simulate the chip production rate, the chip numbers are generated based on the MCT effect at the feedrate between 0 to a certain feedrate that is able to generate the UCT above the MCT. Since the cutting edge wear is unpredictable, the UCT which can be obtained from the feedrate is changed assuming that the cutting edge radius is constant. Also, a number of tooth passes is chosen so as to look at the trend of number of chips generated at the same number of cuts. In. Fig. 44, a flow chart of the chip production rate simulation algorithm is shown. A MATLAB® code is developed based on this flow chart.
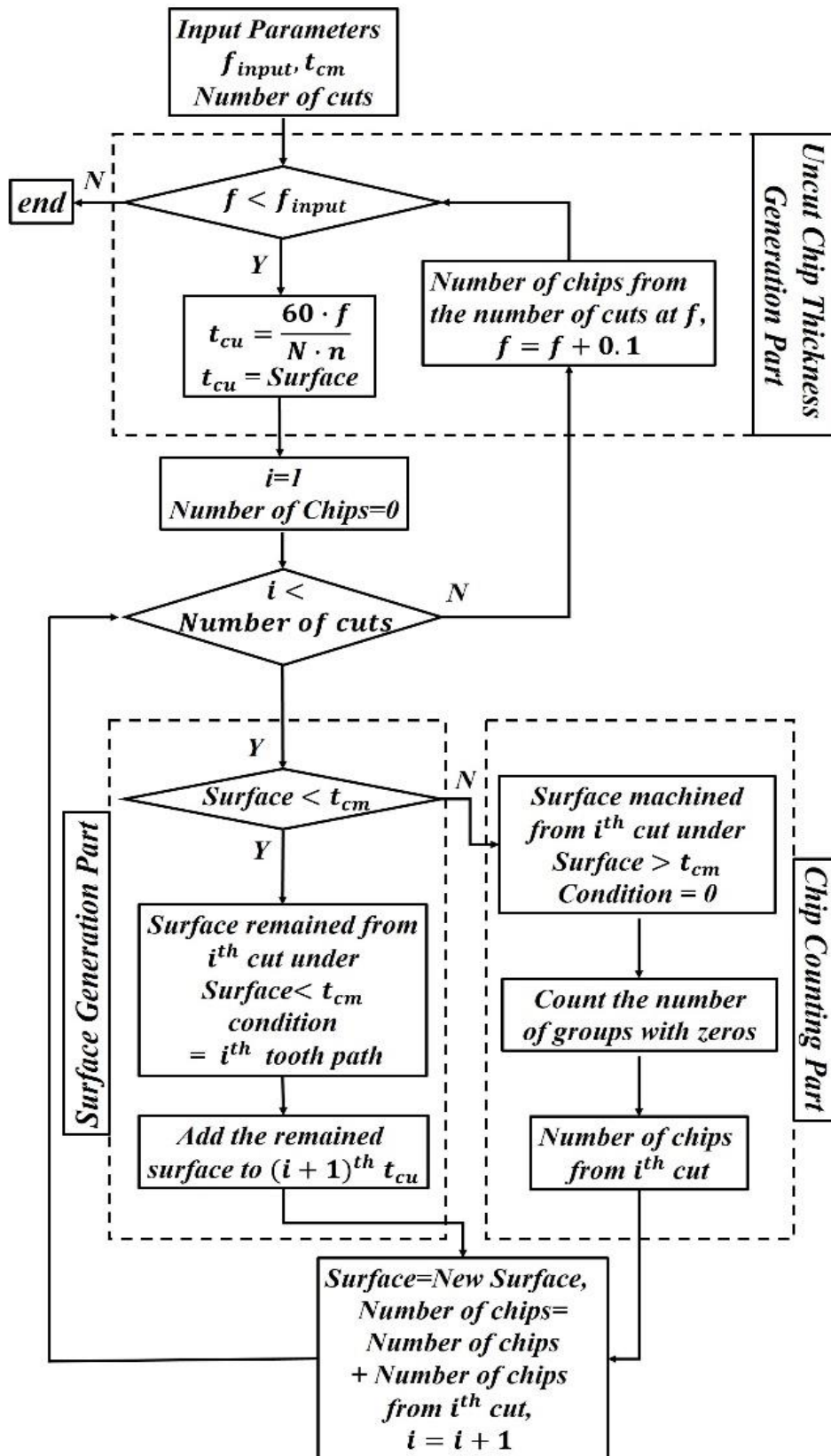
Figure 44. A flow chart of chip production rate simulation algorithm [18]

Section 6. New chip thickness

The engagement angle of a tooth is from $0°$ to $180°$. The UCT is zero at the entrance and the exit and it is equal to the feed per tooth at $90°$. The chip formation occurs only at those angles for which the UCT has exceeded the MCT.

Once a chip is created at i^{th} tooth cut, the new surface created on the workpiece will have the same shape as the removed part of the ith tooth path. When a chip is not produced due to the MCT effect, the remained surface after i^{th} tooth cut will be the same as the $i - 1^{th}$ tooth path. The unremoved part will be accumulated in the $i + 1^{th}$ tooth cut and become a new chip thickness. In Fig. 45, the process of chip generation is shown. As shown in Fig. 45(a), the UCT becomes closer to zero when the tooth enters and leaves the workpiece, and becomes smaller than the MCT during the period. Although one chip is created, it can be seen that there is an unremoved workpiece left at the entrance and the exit and added to the next UCT.

Section 7. Chip counting and chip volume size

The number of chips is obtained by counting the number of groups composed of zero values in the remained surface. In Fig. 45(b), a single chip is formed after the 1st cut and after the 2nd cut. After the 3rd cut, three chips are formed.

Practically, infinitesimally small chips cannot be counted. Thus, we add here a 'filtering' to simulate the number of chips that would be counted given a limitation on the smallness of chips that can be detected with a hypothetical chip counting device. The chips with more than a certain volume (filtering) are only counted to show the change in the number of chips in the different sizes. The chip volume size can be obtained by multiplying the axial depth of cut and the removed area.

(a)

(b)
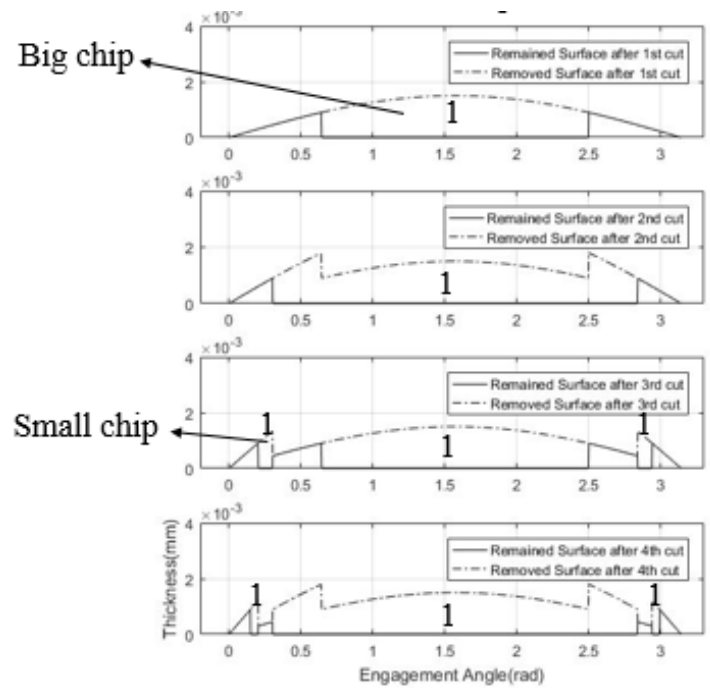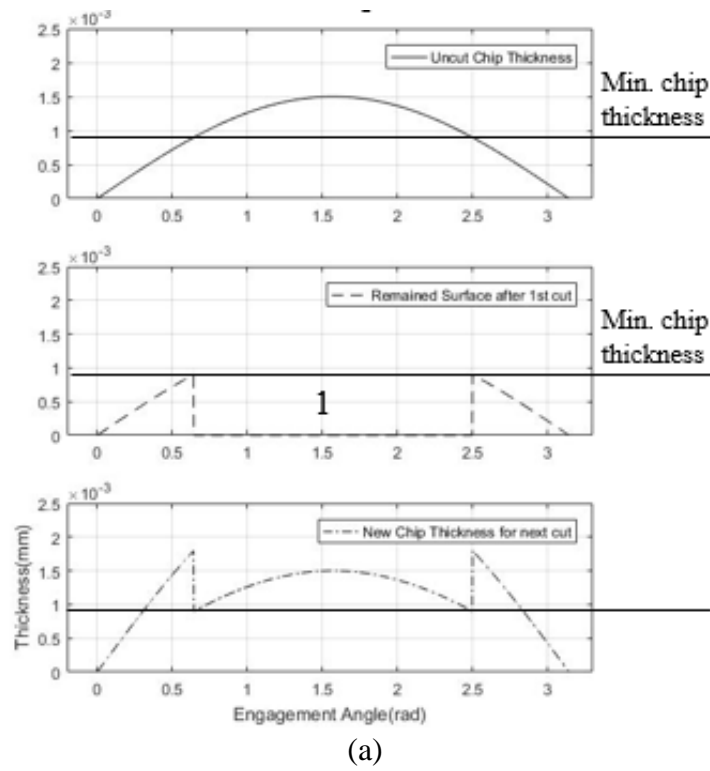
Figure 45. Chip counting and size of chips(a)New chip thickness after the 1st cut in micro-endmilling, (b)Remained surface after the cut [18]

The removed area is calculated from the integration of the removed surface by the trapezoidal rule, shown in Eq. (11), where d is the axial depth of cut, θ_{start} and θ_{end} are the engagement angle at the startstart and end of a formation of a chip. The volume of a perfectly formed chip can be calculated as Eq. (11), where 0.637 of feed per tooth is the average of UCT, V_{chip} is the chip volume, and r is the tool radius.

$$V_{chip} = d \int_{\theta_{start}}^{\theta_{end}} surf \, d\theta = 0.637 \pi r f_{tooth} d \qquad (11)$$

Table 1
Simulation input parameters

Simulation Input Parameters	
Tool Radius (mm)	0.1
Number of flutes	2
Spindle Speed (rpm)	80,000
Feedrate (mm/s)	1.0, 1.1, 1.2, 1.3, 1.4, 1.5, 1.6, 1.7, 1.8, 1.9, 2.0
Cutting Edge Radius (mm)	0.002
Axial Depth of Cut (mm)	0.04
Filter Size (μm^3)	0~22,500
Number of Cuts	500

Section 8. Simulation result

The chip counting simulation for the micro-endmilling operation is conducted using the input parameters in Table 1. The tool radius, spindle speed and the axial depth of cut are selected considering our future experimental conditions. In particular, the spindle speed can also be used as a parameter to determine the UCT. But, the spindle speed is selected as 80,000 rpm, which is the highest speed, in order to minimize the

cutting force [51, 52]. The feedrate is selected between 1.0 mm/s and 2.0 mm/s in order to simulate the change of the number of chips when the UCT crosses the MCT at feedrate 1.6 mm/s which corresponds to the MCT of 0.0006 mm which is the one-third of the cutting edge radius 0.002 mm. The filter values for the chip volume size are chosen between zero and the maximum chip volume size in the simulation. The size of a perfect chip is calculated to be approximately 3,002~6,004 μm^3 in the selected feedrate and it is also applied as a reference of the filter value. And the number of cuts is arbitrarily selected within a range suitable for detecting changes in the number of chips.

(a)

(b)

(c)
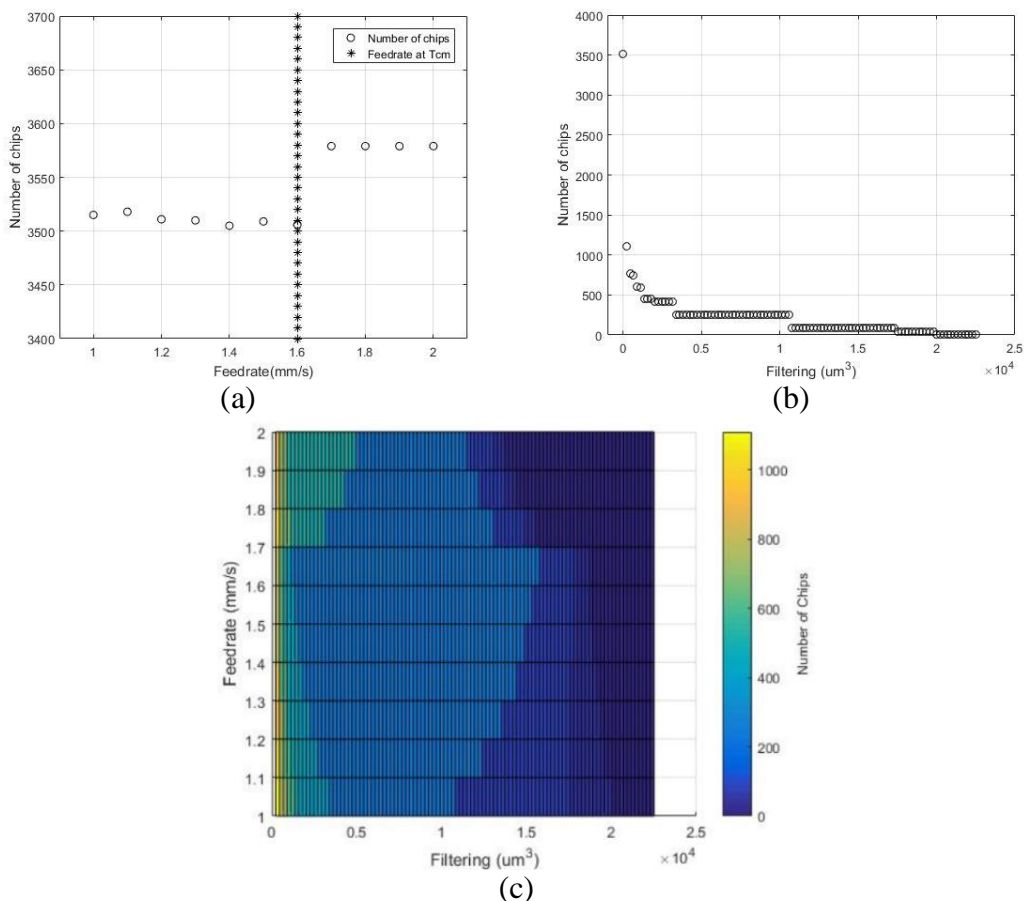
Figure 46. Number of chips vs. filtering vs. feedrate(a)Number of chips in different feedrate without filtering, (b)number of chips at feedrate 1.0 mm/s in different filter values, (c)number of chips in different feedrate and filter values.

The number of chips produced at different feedrates is shown in Fig. 46(a). The number of chips shows a clear 1.9% drop from 3,579 to 3,510 when feedrate is reduced from 1.7 mm/s to 1.6 mm/s and crosses the feedrate that corresponds to the MCT. And the result includes all the chip volume sizes. But, approximately 60% of chips are smaller than 225 μm^3 which is less than 10% of the volume of a perfectly formed chip as shown in Fig. 46(b).

The chips smaller than 225 μm^3 are difficult to be detected and counted in the future experiments due to its small size. Therefore, those chips are neglected in this simulation of chip counting by using the filtering.

In Fig. 46(c), the number of chips in different feedrate and filter values are shown. When the filter value is smaller than the 5,400 μm^3, the number of chips decreases as the feedrate decreases from 2 to 1.6 mm/s and it increases as the feedrate decrease from 1.6 to 1 mm/s. When the filter value is between 5,400 and 10,580 μm^3, the number of chips is almost the same in all the feedrate range. When the filter value is larger than the 10,580 μm^3, the number of chips increases as the feedrate decreases from 2 to 1.7 mm/s, 1.6 to 1 mm/s. When the filter value is between 5,400 and 10,580 μm^3, the number of chips is almost the same in all the feedrate range. When the filter value is larger than the 10,580 μm^3, the number of chips increases as the feedrate decreases from 2 to 1.7 mm/s and it decreases as the feedrate decreases from 1.6 to 1 mm/s. However, at the feedrate between 1.6 ~ 1.7 mm/s and at the filter value between 1,125 ~ 2,925 μm^3, the number of chips decreases from 502 to 261 which 1.6 ~ 1.7 mm/s and at the filter value between 1,125 ~ 2,925 μm^3, the number of chips decreases from 502 to 261 which is 48% of the sharp drop. And, at the same feedrate range but at the different filtering value between 13,050~14,630 μm^3, the number of chips

increases from 83 to 251 which is 202.4 % of the sharp increase.

Section 9. Summary

This result shows that the changes in the state of the interaction at the tool-workpiece interface due to the MCT effect would result in the changes in the chip production rate. Therefore, the detection of the chip production rate changes would allow the prediction of the state of the interaction between the tool and the workpiece.

In micro-endmilling, it is very important to maintain good machining performace. And, the state of the interaction significantly affects the machining performance such as the surface finish, the machining accuracy, and the tool life etc. As a result, there have been many studies measuring the variations in cutting conditions (the tool wear, cutting temperature, cutting force etc.) that may occur during the state change, and the values are used to enhance the machining performance. In this respect, the chip production rate might also be used to improve the machining performance in the future.

In the next chapter, the experimentation of the chip counting in micro-endmilling process is described. A device for counting the number of chips produced during the cutting process has been designed and built. Since the simulation presented here shows a relationship between chip production rate and cutting-edge radius, it is expected that information about tool wear may be able to be obtained real-time and automatically during the cutting process as described in chapter 6.

CHAPTER 4

CHIP PRODUCTION RATE EXPERIMENT

The chip counting experiment is performed to validate our simulation result. Simulation is carried out under the same conditions as the experiment. The experimental set-up and the cutting teest conditions are explained. In order to obtain the number of chips from the image, a digital image processing algorithm is developed And the experimental results are analyzed [129]. The experimental results show that the number of chips decreases gradually when the UCT is crossing the MCT.

Section 1. Simulation for experiment

Prior to the experiment, a new simulation is performed with the different filtering values listed in the Table 2. In the simulation results reported in Fig. 46, the number of chips varies depending on the feedrate and the size filtering values. It is not physically possible to count infinitesimally small chips. Thus, we apply a 'filtering' to the simulation to count the number of chips that takes into account a limitation on the size of chips that can be detected by an experimental setup.

Table 2
New Simulation input parameters

Simulation Input Parameters	
Tool Radius (mm)	0.1
Number of flutes	2
Spindle Speed (rpm)	80,000
Feedrate (mm/s)	1, 2, 3, 4, 5, 6
Cutting Edge Radius (mm)	0.002
Axial Depth of Cut (mm)	0.04
Filter Size (μm^3)	0, 5000, 10000, 15000, 20000
Number of tooth passes	500

If the size filtering value is less than 10,000 μm^3 as illustrated in Fig. 47(a) and (b), then the number of chips drops between the feedrate 2 and 1 mm/s near the critical feedrate of 1.6 mm/s. However, if the filtering value is larger than 10,000 μm^3 as illustrated in Fig. 46(c), (d) and (e), then the number of chips decreases gradually.

(a)

(b)

(c)

(d)

(e)
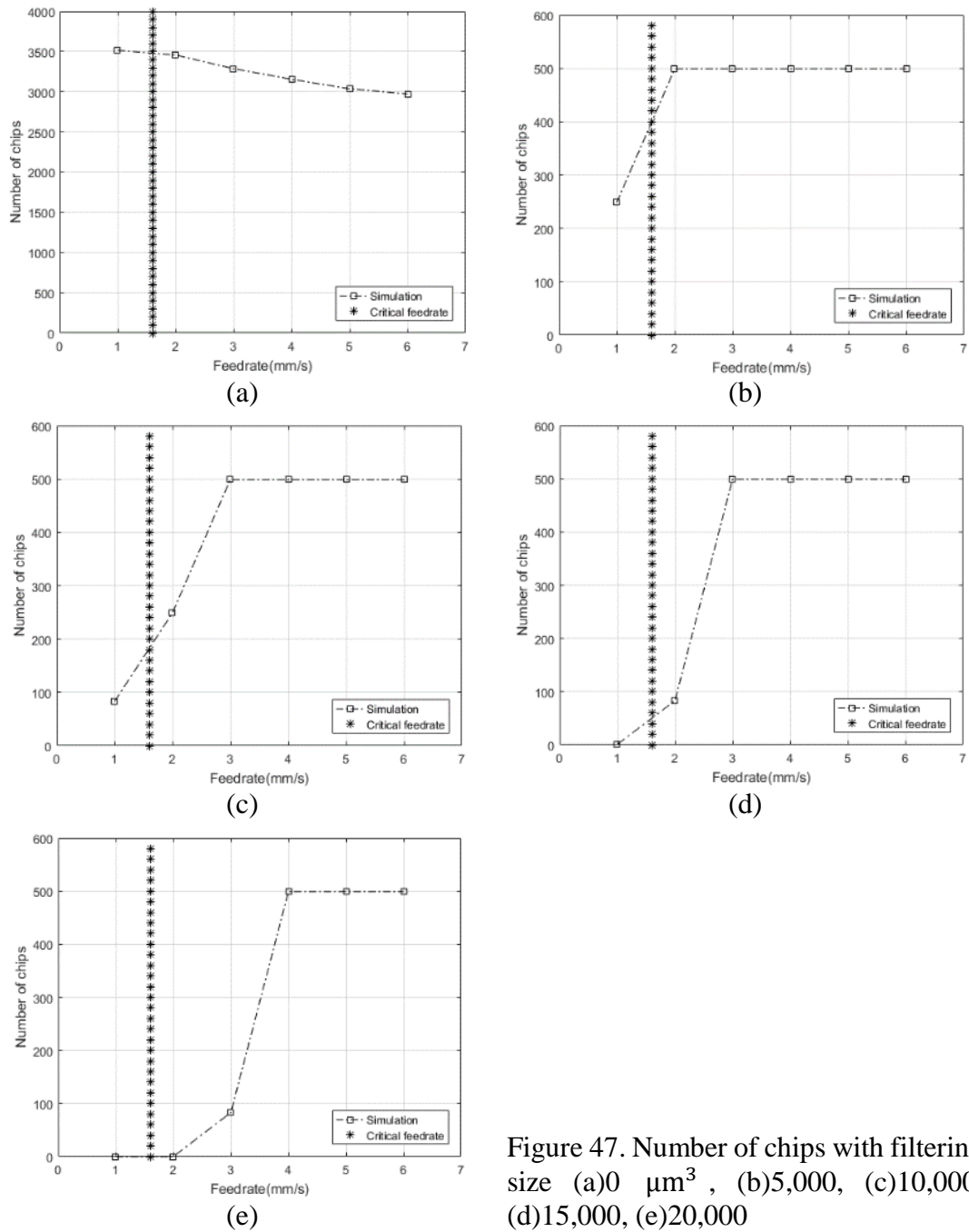
Figure 47. Number of chips with filtering size (a)0 μm^3, (b)5,000, (c)10,000, (d)15,000, (e)20,000

Section 2. Experimental setup

We have designed and built a machine that is capable of collecting and counting the chips produced by a micro-milling process, and filtering the chips for size. A conceptual schematic of the machine is shown in Fig. 48.
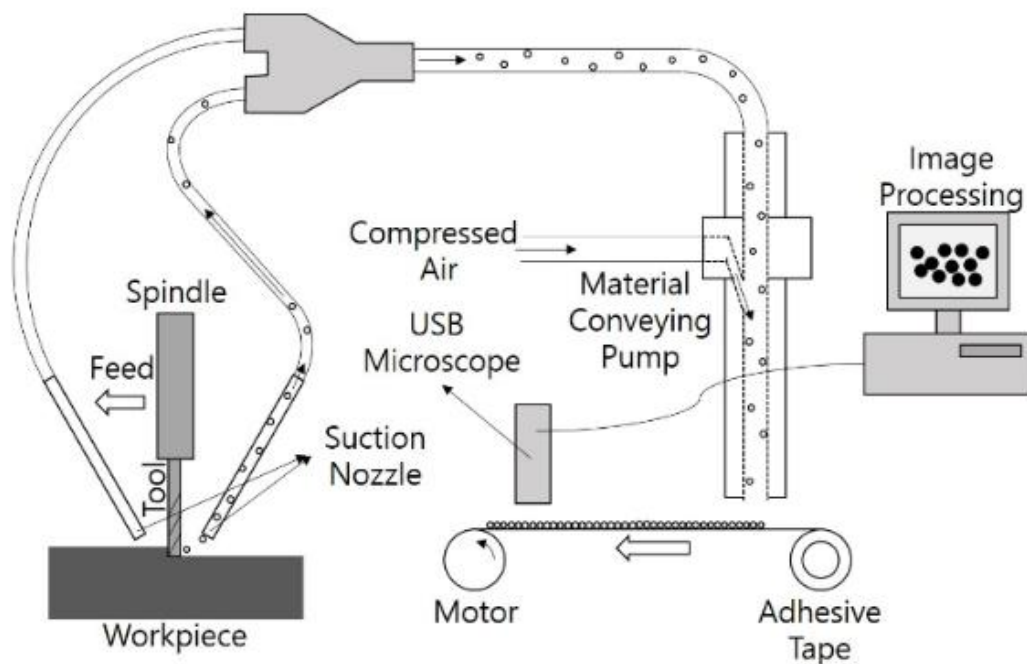
Figure 48.Conceptual schematic of a chip counting system [129]

In this machine, chips are vacuumed from the point of production at the tool tip through the suction nozzle and the tube and dispersed through the outlet nozzle onto the adhesive tape on the conveyor system as shown in Fig. 49(a). The chips are then imaged with a USB digital microscope (Dino-Lite Pro 1.3 MP).

An image processing algorithm is written to count the chips in the image. Only chips above a specified size threshold are counted, thus filtering the chips for size. A custom-built 3-axis micro-milling machine with the spindle (NSK NR-3080S) attached to a brushless motor (EM3080J) controlled by Beckhoff TwinCat 3.0 environment is

fitted with the 3D printed suction nozzle holder with tubing connections as shown in Fig. 49(c). The suction nozzle is an aluminum pipe. In order to increase the efficiency of this pneumatic system, a LDPE (Low- density polyethylene) tube with a low internal drag force is used for connections.
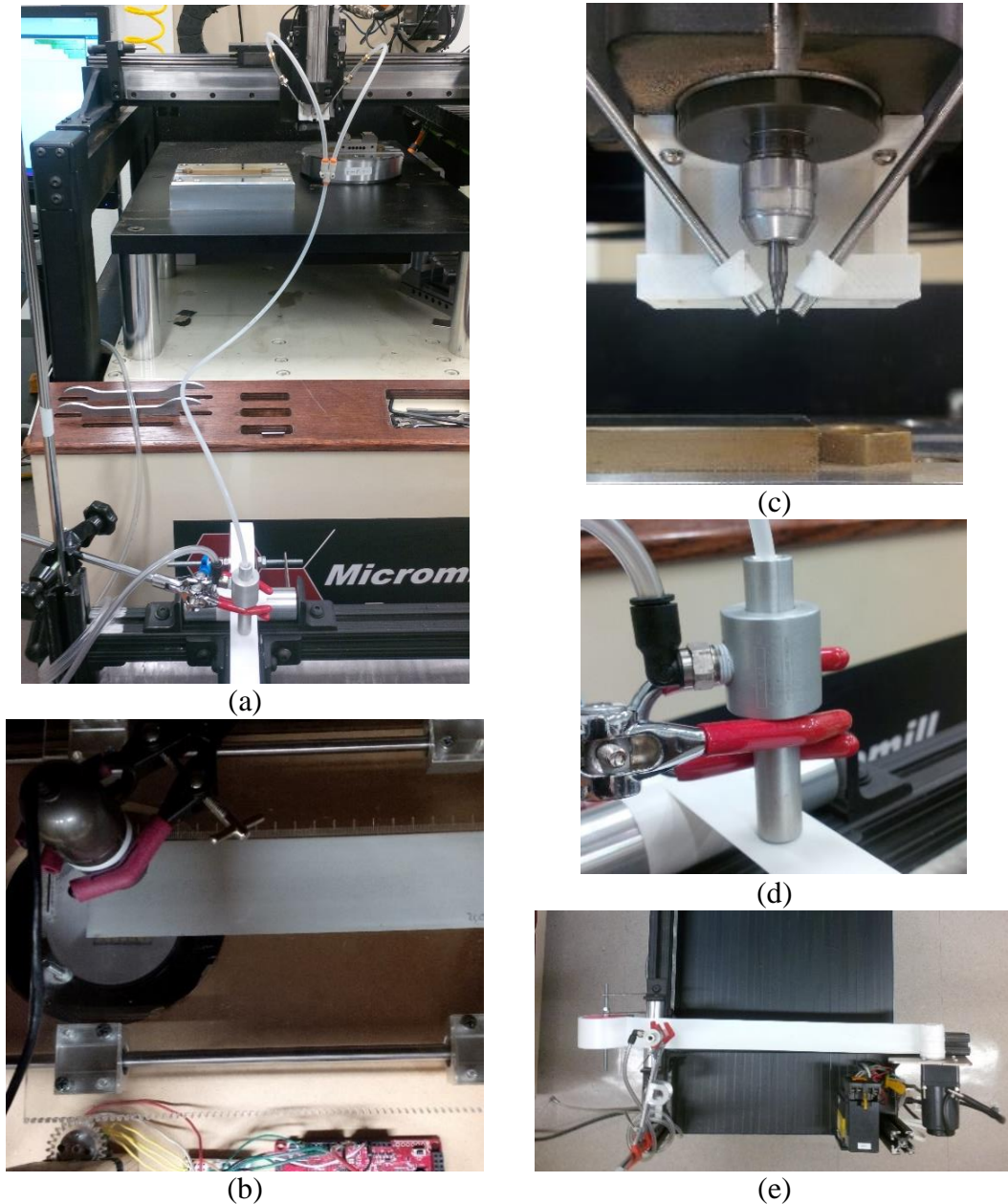
Figure 49. Experimental set-up(a)chip collecting system [129], (b)image taking moving table with a UBS digital microscope, (c)chip suction nozzle, (d)material conveying air pump, (e)conveyor system with the vinyl tape,

71

A material conveying vacuum air pump (VACCON DF 1-3) is connected to the inlet tubing, and the outlet dispersion is through the outlet of the vacuum pump, as shown in Fig. 49(d). A roll of white vinyl tape (white commercial 3M general purpose vinyl tape 764) is attached to a static roller. The end of the tape is then pulled out and attached to a motor, as shown in Fig. 49(e). The motor (USM206-401W2) speed is controlled by a motor speed controller unit (USP206-1U2).

The machining parameters are spindle speed, feedrate, and depth of cut. The spindle speed is selected as 80,000 rpm which is the maximum speed of the spindle. In the micro-milling process, the spindle speed needs to be high enough so that the cutting force can be reduced [51, 52]. A 2-flute 200 μm tungsten carbide micro-endmill (Performance Micro Tool: 200M2X600S) is used in this experiment. The cutting edge radius of a micro-endmill is measured as 2~3 μm in the previous research [42, 54, 55]. Therefore, the MCT can be approximated as one-third of the cutting edge radius which is 0.67~1 μm. In order to ensure that the UCT crosses the MCT during the experiment, the feedrate is selected as 1~6 mm/s which corresponds to a range of the feed per tooth of 0.3~2 μm for a 2-flute endmill at 80,000 rpm spindle speed. The depth of cut is arbitrarily selected as 40 μm. A moving table is developed that translates a transparent acrylic plate in one direction. After the tape is moved onto the table, the USB digital microscope is used to take pictures of the tape lying on the table with as shown in Fig. 48(b). The table is translated by a rack and pinion gear motion attached to a geared DC motor. The table is moved by a simple on-off logic and moves by 1 cm after each picture is taken. The images are taken when the table is stopped to avoid the blurriness of the image. An LED back light is placed below the tape to back-illuminate the chips and provide high contrast between the tape and the chips. The image processing toolbox in

Matlab R2016b is used to count the number of chips from the image. A custom object counting algorithm for counting chips is developed here and is reported in the next section. A microscope (Olympus MX50) is used to take pictures of the bottom view of the tool for cutting-edge radius measurements.

Section 3. Digital Image processing

The chips from the micro-end-milling operation can be counted from an image of the chips taken by a microscope. Because of the large number of chips and the high rate of chip production, hand-counting is excessively tedious. Thus, an object counting algorithm is applied to count the chips. This type of algorithm has been already applied to other applications such as counting red blood cells [131] or counting fish in a water tank [132], etc. In our method, instead of using global threshold method, the locally adaptive threshold method is applied addition to the existing object counting algorithms in order to get the accurate number of chips since the images have blurry parts due to the performance of the microscope.

In order to apply the counting algorithm, the images should be in binary form. The important factor in the binarization process is a threshold. There are two threshold methods: the global and local threshold methods. The global threshold is based on Otsu's method which automatically selects a fixed threshold from a gray-level histogram of an image [133]. The drawback of the global threshold method is that the binarization fails when an image has varying illumination. In order to avoid this failure, the locally adaptive threshold has been developed. It calculates a different threshold in each local group of pixels to account for varying illumination.

Among many Locally Adaptive Threshold Methods, a method developed by

Bradely and Roth [134] is applied in this research.

In this work, a chip-collecting device is used to collect the chips from a slot micro-end-milling operation, and sample images of the chips are obtained by USB microscope. Digital image processing is performed based on Locally Adaptive Threshold Method and the morphological operations [135].

A sample image (2560 × 2048) of the tape with the chips is shown in Fig. 50(a). In the figure, the chips in the in-focus area in the center of the image are more easily distinguishable from the background than the chips in the outer area which is out-of-focus. The chips in the out-of-focus area would not be counted accurately due to the blurriness. In order to remove the out-of-focus area from the image, the boundary between the in-focus and the out-of-focus area needs to be determined. However, it is difficult to determine the boundary due to the gradual change in the blurriness from the center to the outside of the image.

In order to understand the properties of the image, the gray-level of the chips and the background are investigated. The RGB image is converted into the gray-scale image to obtain the gray intensity level. The conversion is conducted by an algorithm which sums the weighted values of R, G, B components [136]. The level is represented by an integer between 0 ~ 255 (black~white) and it is higher in the in-focus area but lower in the out-of-focus area as shown in Fig. 50(b).

In Fig. 50(c), the average grayscale levels of the randomly picked chips, one from the in-focus area and one from the out-of-focus area are obtained as 89.2 and 118.0, respectively. Also, the average level of a randomly cropped background from the in-focus area and the out-of-focus area are 142.1 and 141.3, respectively. And, the average level of the whole image is 140.9. According to those values, the gray level of an image

is dominated by the background. But, the gray level of a chip is significantly influenced by the blurriness. The chips are counted by finding the connected components in a binary image.

(a)

(b)

(c)
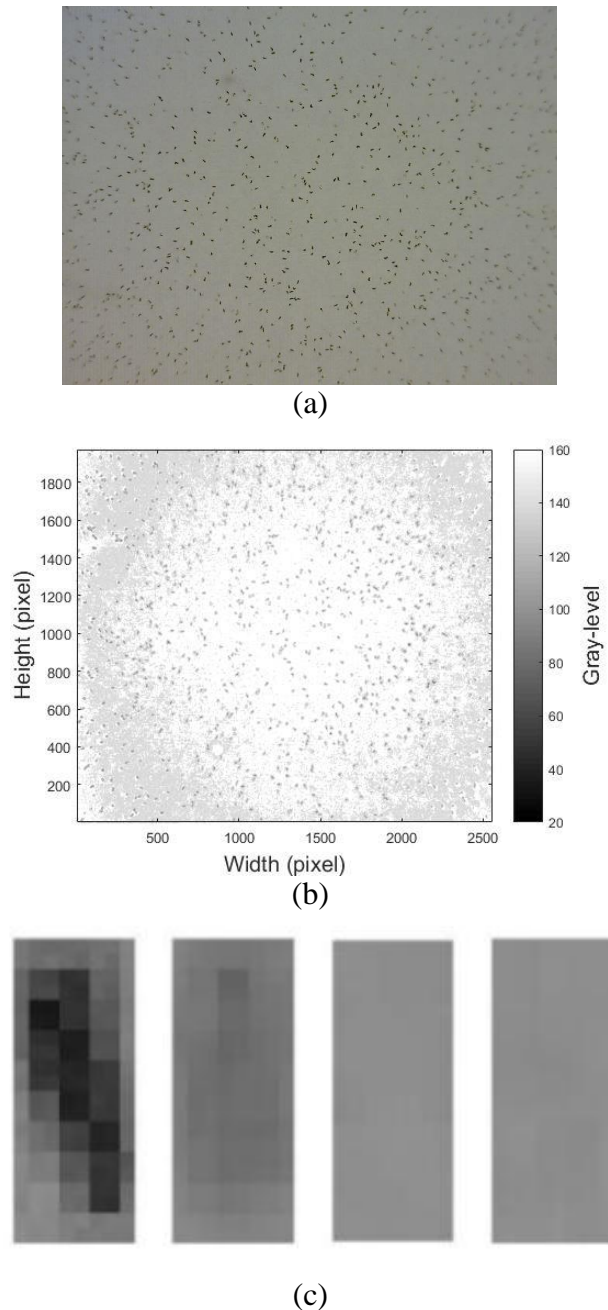
Figure 50. An image sample from chip counting system(a)an image of the tape with the chips, (b)gray level of the image, (c)a chip in the in-focus area and in the out-of-focus area, a background area in the in-focus area and in the out-of-focus area (from left to right)

75

Here, we briefly review the method of counting that is used in the testing of each binarization method.
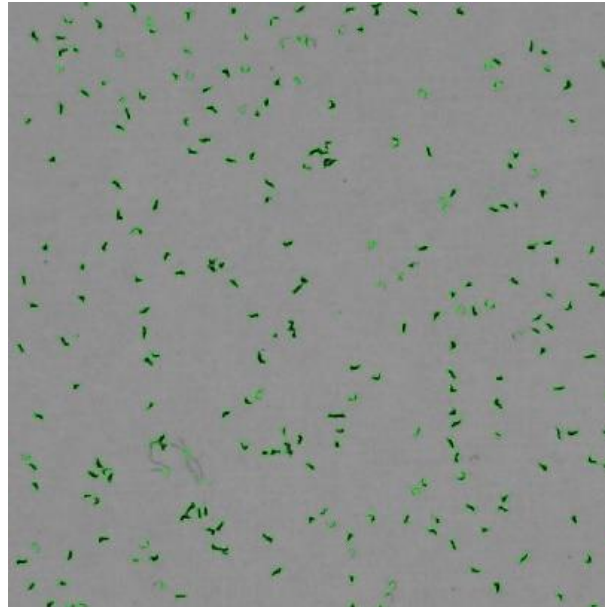
Figure 51. Boundaries(green lines) around the labeled areas with more than 4-connected pixels

The number of labeled areas that are connected to more than 4 neighbor-hood pixels are counted as the chips in an image [137]. Fig. 51 illustrates the detection of the chips by placing an outline around each detected chip. In the example image shown in Fig. 51, the number of chips is 235. In order to apply the connected-pixel chip counting algorithm, the image has to be a binary image which only has black and white. A threshold value is needed to separate individual pixels into two classes: background and objects. Hence, the number of chips is largely dependent on the threshold value.

The Global Threshold Method generates one threshold which separates an image into the background and the objects [133]. However, the global threshold is not suitable for an image with a varying gray-scale level in the background. To compensate for such a shortcoming, the Locally Adaptive Threshold Method has been developed

[134]. The sampled image of chips from the out-of-focus area has blurriness which can be considered as the varying gray-scale level. Therefore, Locally Adaptive Threshold Method is applied to obtain an accurate number of chips from the image.

(a)

(b)

(c)

(d)

(e)
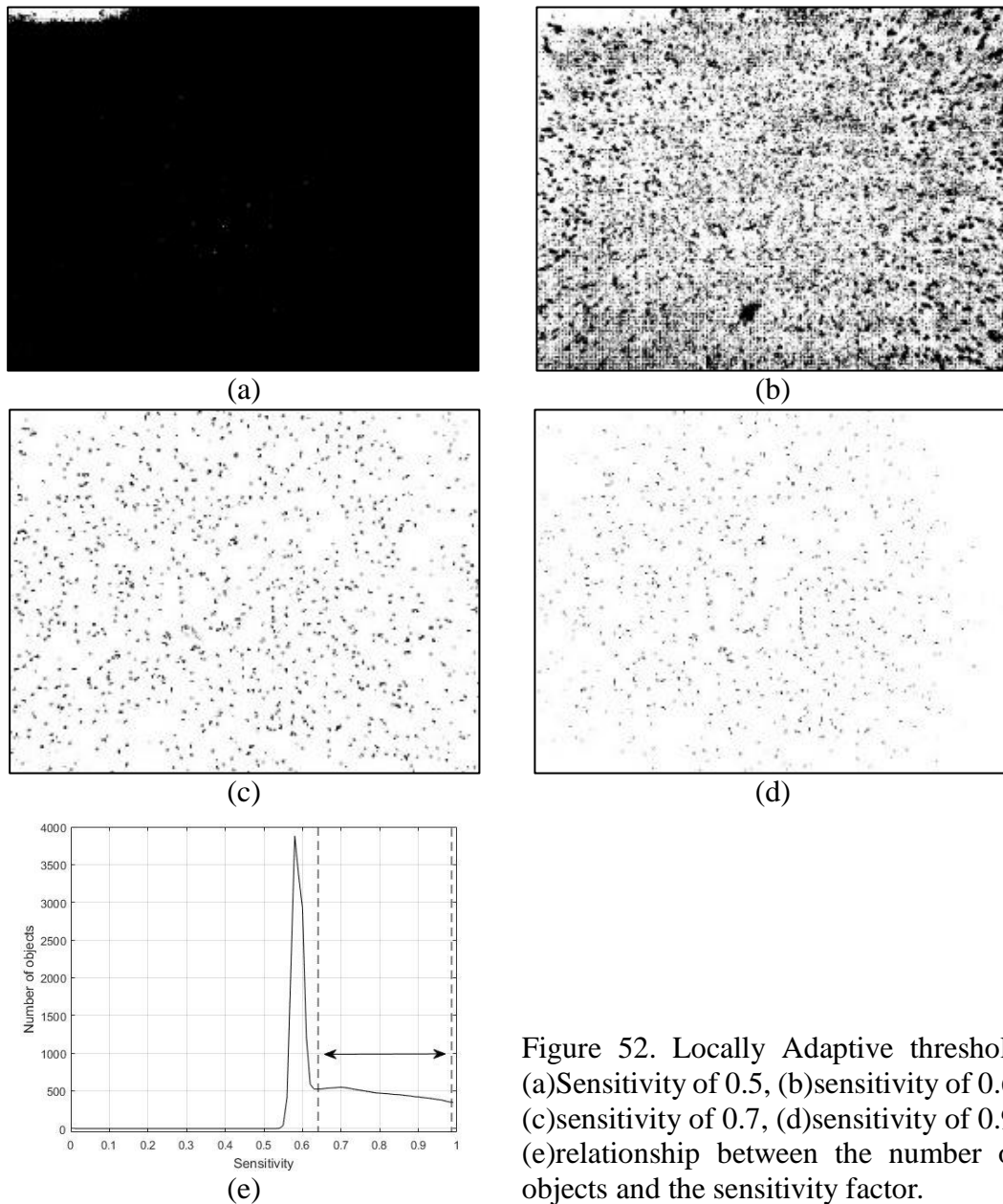
Figure 52. Locally Adaptive threshold (a)Sensitivity of 0.5, (b)sensitivity of 0.6, (c)sensitivity of 0.7, (d)sensitivity of 0.9, (e)relationship between the number of objects and the sensitivity factor.

The Locally Adaptive Threshold Method requires a 'sensitivity factor' which determines the pixels that will be thresholded as the foreground pixels [138]. The binary

images obtained from the locally adaptive threshold with sensitivities of 0.5, 0.6, 0.7 and 0.9 are shown in Fig. 52. When the sensitivity is too low, as shown in Fig. 52(a), no chips are found in the image because the background is thresholded as the foreground and the entire image is dark. But, when the sensitivity is set too high, as shown in Fig. 52(d), only the chips in the in-focus area are counted because the chips in the out-of-focus area are removed. Therefore, the optimal sensitivity factor needs to be determined in order to obtain an accurate chip count.

The influence of the sensitivity factor on the chip counting in the out-of-focus area is shown in Fig. 53. The chips with the green boundary are the chips that are counted. The arrows in the figures show the chips which describes the major differences between the different sensitivity factors.

(a) (b)

(c) (d)
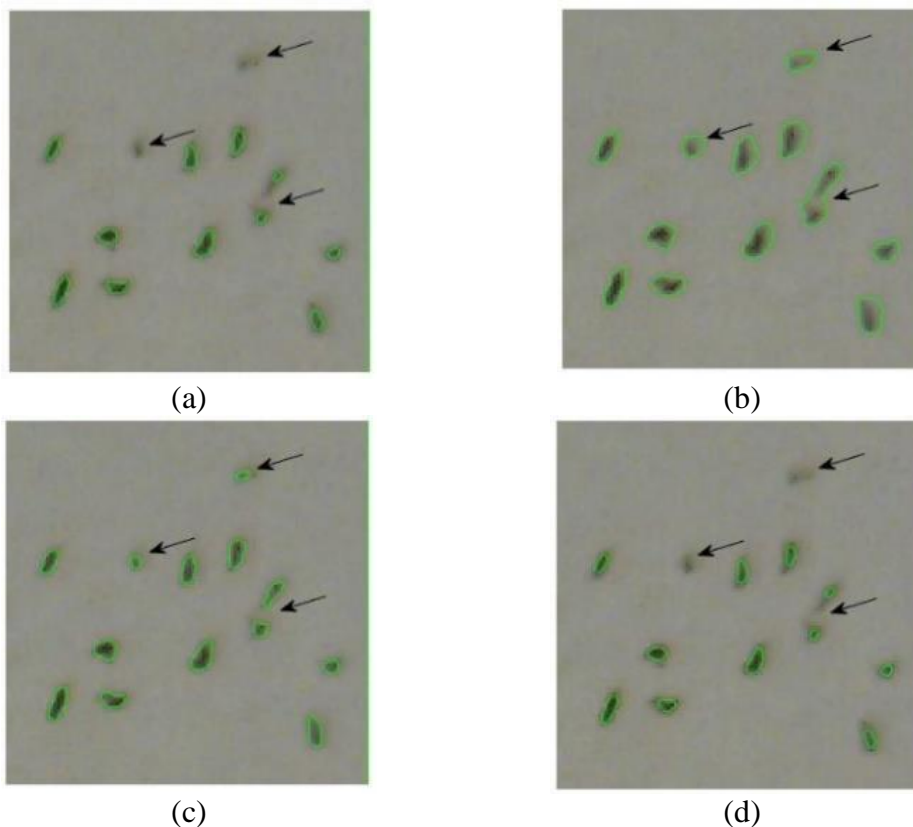
Figure 53. Sensitivity factor and the chips in the out-of-focus area, (a)global threshold, (b)local threshold with the factor of 0.65, (c) local threshold with the factor of 0.75, (d) local threshold with the factor of 0.85

In Fig. 53(a), the two chips are not counted when the global threshold is applied. In Fig. 53(b), (c) & (d), the chips are counted by applying the local threshold. But, the two chips are counted as one chip in Fig. 53(b) with the sensitivity factor of 0.65 and the two chips are not counted in Fig. 53(d) with the sensitivity factor of 0.85. In Fig. 53(c), all the chips are counted with the sensitivity factor of 0.75. Therefore, the sensitivity factor is chosen between 0.7~0.8.

(a)

(b)

(c)

(d)

(e)
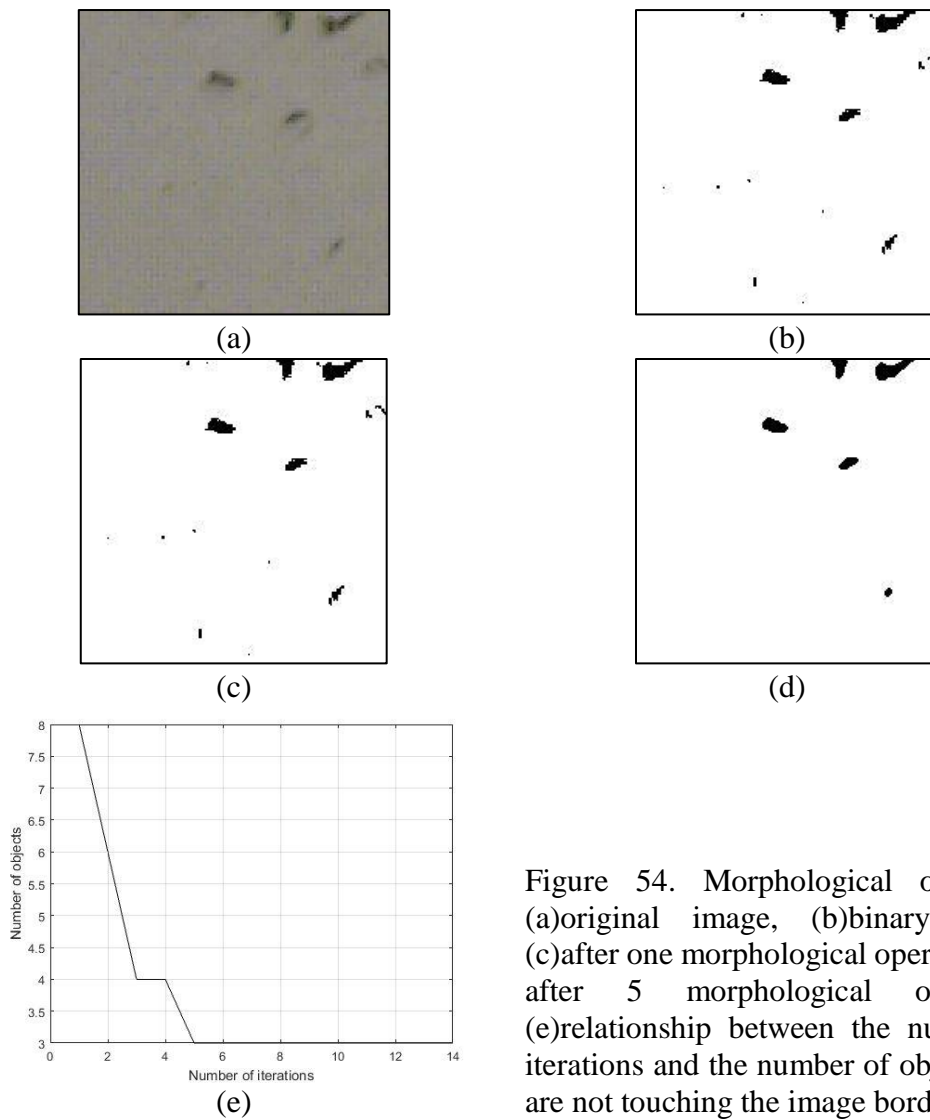
Figure 54. Morphological operation, (a)original image, (b)binary image, (c)after one morphological operation, (d) after 5 morphological operations (e)relationship between the number of iterations and the number of objects(that are not touching the image border)

79

The 'majority' morphological operation is applied to the images to make the chips smoother as shown in Fig. 54(a)-(d) [135]. The 'majority' operation sets a pixel to one, if a pixel has more than five ones in its 3-by-3 neighborhood. The image before the operation has many isolated pixels and objects with uncertain shape and gray-scale levels as shown in Fig. 54(b).

After one 'majority' operation, the shape of the chips becomes smooth and the isolated pixels are removed as shown in Fig. 54(c). However, the uncertain objects are still unremoved. After 5 iterations, only the chips are remained as shown in Fig. 54(d) & (e). The iterations for the original image size should be more than 20 to get the converged value.

One of the main issues in the image processing is computing time. The relationship between the computing time and the image size has to be investigated to optimize the chip counting process. The chip counting system needs to operate automatically while the micro-end-milling machine is cutting the workpiece. And, the number of chips should be counted before the microscope takes the next image. Therefore, the computing time to obtain the number of chips needs to be considered for the future experiment. The time for computing the locally adaptive threshold with the 20 iterations of 'majority' morphological operation increases as the size of the image increases as shown in Fig. 55. The choice of the appropriate image size should be made so that image processing can take place within a fixed amount of time.

In order to count the chips, 10 of the 80 images taken by the USB microscope are selected randomly. And, one small image of the size of 1600 by 1600 is cropped from each of the 10 images regardless of the area.
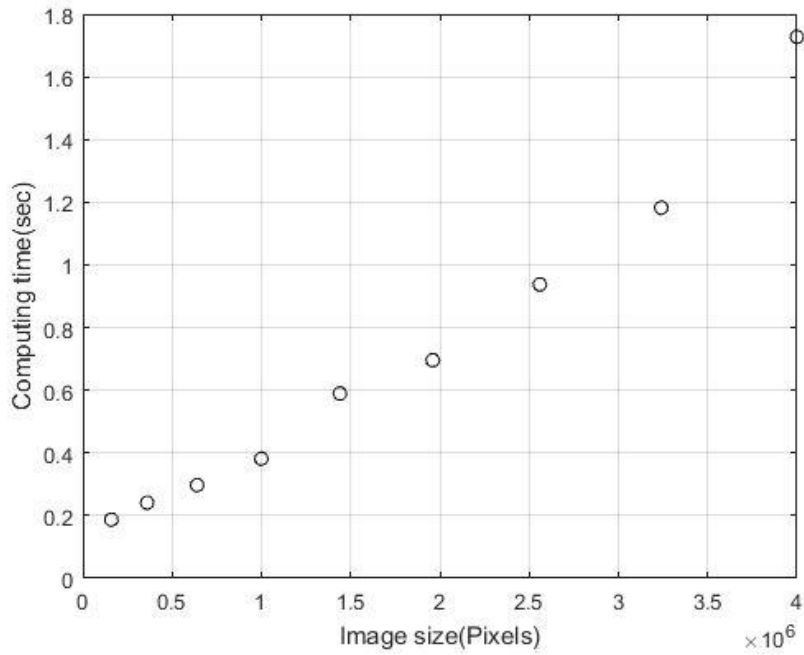
Figure 55. Relationship between the computing time and the image size

Prior to counting chips in the 1600 by 1600 images, the chips in the 400 by 400 cropped images are counted both manually and automatically to test the reliability of Locally Adaptive Threshold Method as shown in Fig. 56.
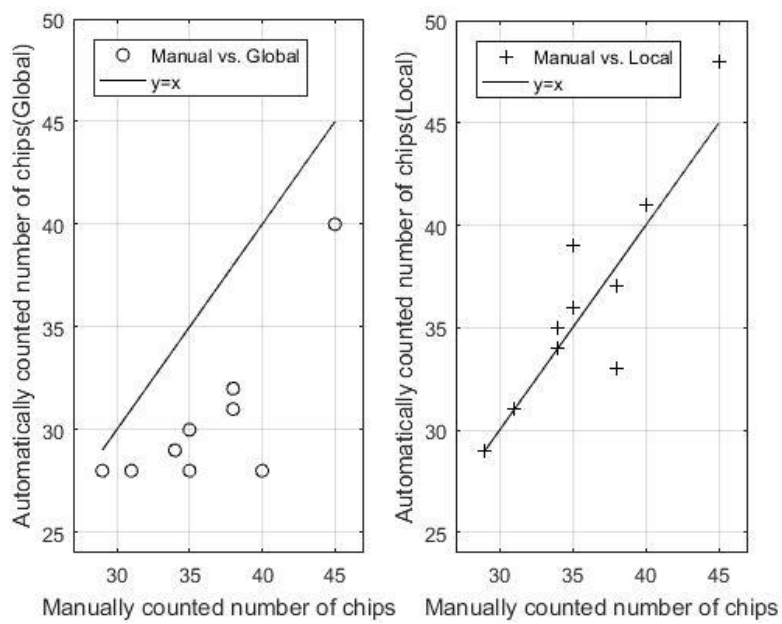
Figure 56. Comparison between the number of chips counted manually and automatically

The size of 400 by 400 is selected so that the amount of the chips in the image becomes manually countable. The sensitivity factor of 0.7 is applied. The morphological operations are performed for 25 iterations in each image. The test results are listed in Table 3. The total number of chips from the 10 cropped images by the global threshold method has counting error greater than twice the counting error by Locally Adaptive Threshold Method.

After Test.1, the number of chips in the images of size 1600 by 1600 is counted automatically as shown in Table 4. The size of 1600 by 1600 is chosen to finish the computation within 1 sec based on Fig. 55. The sensitivity factor and the number of iterations of the morphological operation are not changed from Test.1. The difference between the number of chips obtained by the global threshold and the local threshold is in the range of 10~20 %. The main reason of the difference is that the global threshold method is not counting the chips in the out-of-focus area accurately as shown in Fig. 57.
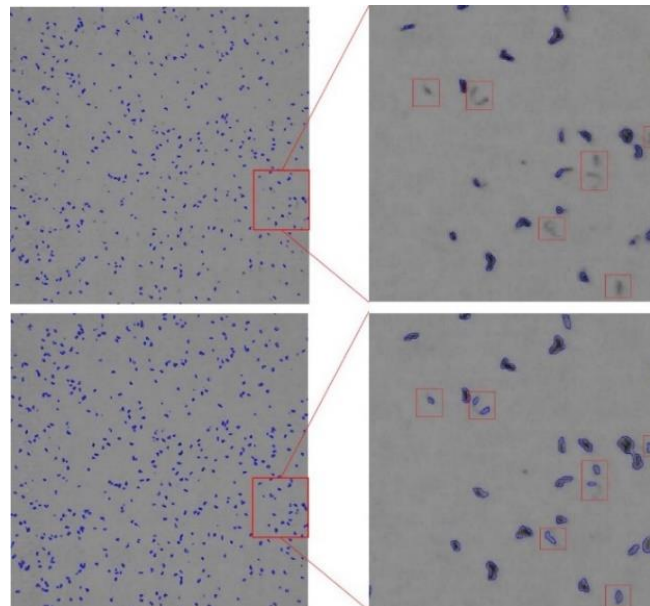
Figure 57. Labeled area from global threshold method (above) and local threshold method(below)

A chip counting method using digital image processing is investigated. The importance of counting the number of chips in micro-end-milling operation is discussed. The results from Test. 1 show that the chip counting algorithm using Locally Adaptive Threshold Method can be applied to the image with less than 10% counting error. It is sufficiently accurate to detect the change in the number of chips expected in the future experiments based on our chip counting simulation from the previous research [18]. And the second test shows that Global Threshold Method may not be able to count nearly 20% of the chips compare to Locally Adaptive Threshold Method. These results indicate that the effective chip count can be achieved using Locally Adaptive Threshold Method.

Table 3
Number of chips in the image size of 400 by 400

| Test1 | Manual | Automatic | | | |
| | | Global | | Local | |
	Number of chips	Number of chips	Error (%)	Number of chips	Error (%)
1	359	303	15.6	363	1.11
2	297	264	11.11	313	5.39
3	289	261	9.69	302	4.5
4	312	264	15.38	316	1.28
5	294	265	9.86	304	3.4

Table 4
Number of chips in the image size of 1600 by 1600

| Test2 | Automatic | | Difference (%) |
	Global Number of chips	Local Number of chips	
1	419	522	19.73
2	446	516	13.57
3	521	590	11.69
4	475	561	15.33
5	444	511	13.11

In this section, the digital image processing to get the number of chips from the images is explained. The locally adaptive threshold method is applied to the image processing since the global threshold is not accurately counting the chips in the blurry parts of the images.

In the next section, the chip production rate experiment is explained.

Section 4. Experiment

A brass workpiece is fixed to the work table. The workpiece is faced off with a 2 mm endmill before every set of experiments. The 200 μm tool is installed on the tool holder of the spindle. The tip of the tool is touched off on the workpiece surface. The axial depth of cut is set to 40 μm and the radial depth is 200 μm (full-slotting). The spindle speed is set to 80,000 rpm.

The air flow rate for the chip suction part is fixed to the maximum of 3 SCFM (Standard Cubic Feet per Minute) at the air pressure of 40 PSI. The conveyor pulling motor is turned on at a constant speed to pull the tape. Then, the endmill is fed into the workpiece at a constant feedrate to perform a slot milling operation. When a complete slot is finished, the machine is turned off and the tape with the chips is removed from the system by cutting off a portion of the tape that is more than a certain distance (30 to 40 cm) from where the chips start to stick on the tape.

The tape with chips is then placed on the moving table. The tape is translated from one side to the other side to take the image of the different area so that a number of image samples can be obtained from one slot milling. Fig. 58 shows an image of collected chips on the tape.
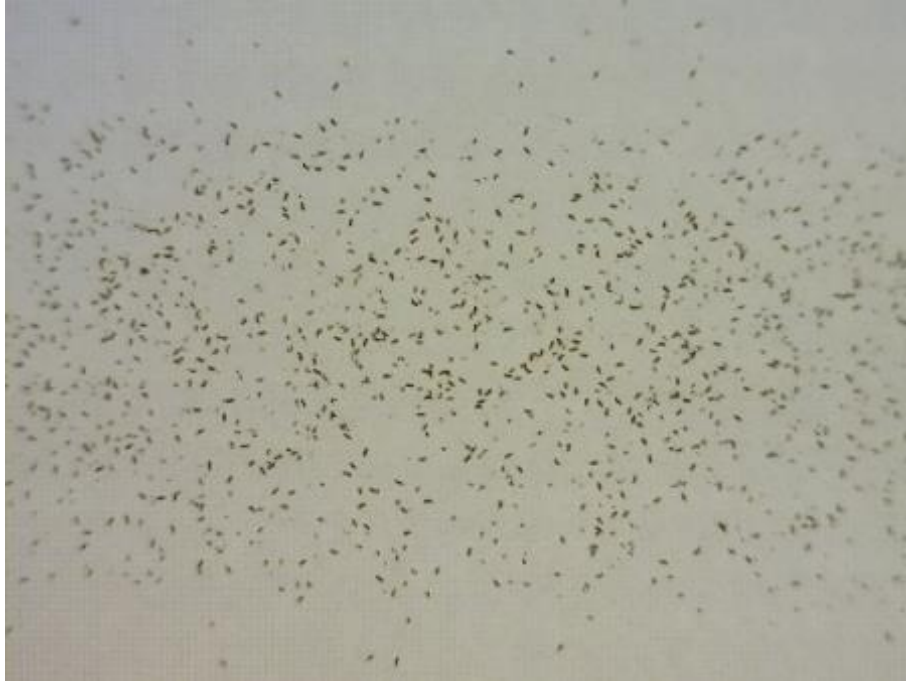
Figure 58. Image of the chips on the tape taken by a USB digital microscope

The chips in the images are counted using the chip counting algorithm. Within one experimental set, a number of channels are cut, and every single channel is cut at a constant feedrate. The first channel is cut at a feedrate of 1 mm/s, and each subsequent channel is cut at a feedrate 1 mm/s faster than the previous feedrate. The last channel is cut at a feedrate of 6 mm/s.

All the experiments are conducted in the same experimental conditions except the cutting edge radius of the tool. Within one experimental set, a number of channels are cut, and every single channel is cut at a constant feedrate. The first channel is cut at a feedrate of 1 mm/s, and each subsequent channel is cut at a feedrate 1 mm/s faster than the previous feedrate. The last channel is cut at a feedrate of 6 mm/s.

The images of the bottom view of the tools are taken before every set of cutting experiments to measure the cutting edge radius and to ensure that the tool is not broken as Fig. 59.

<div style="text-align:center">(a)   (b)</div>
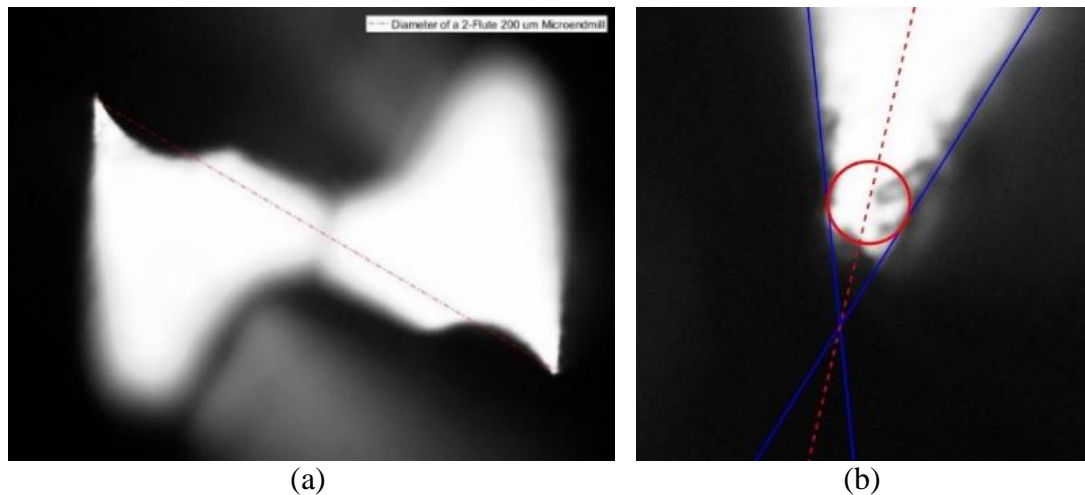
Figure 59. Cutting edge radius of a micro-endmill(a)Image($\times$ 50) of the bottom view of a new 200 μm micro-endmill taken by the microscope, (b) image($\times$ 100) of the cutting edge of the new tool(cutting edge radius: 1.8 μm)

Section 5. Result

The chips from cutting tests are counted. 30 images are sampled from one slot milling test at 4 mm/s feedrate. The number of images is determined based on the length of the tape with collected chips. The speed of the tape is 16.4934 mm/s since the diameter of the pulley on the motor shaft is 45 mm and the motor speed is 7 rpm. And the length of the slot is 110 mm. Therefore, the maximum tape length that is able to obtain from the slot milling with the feedrate of 6 mm/s is 30.2379 mm. Then, the moving tape in the chip counting device translates by 10 mm after each picture is taken. Therefore, the maximum number of images able to get is 30. Moreover, in order to keep the consistancy, 30 images are taken even with the other feedrates from 1 mm/s to 5 mm/s which generate longer tape. The mean (1,279) and the standard deviation (65.29) of the number of chips from the not cropped images is shown in Fig. 60(a). The coefficient of variance of the number of chips from the cutting test is 5.1%. When the image is cropped, the mean (415) and the standard deviation (15.73) of the number of chips from the cropped images is shown in Fig. 60(b).

<div style="text-align:center">86</div>
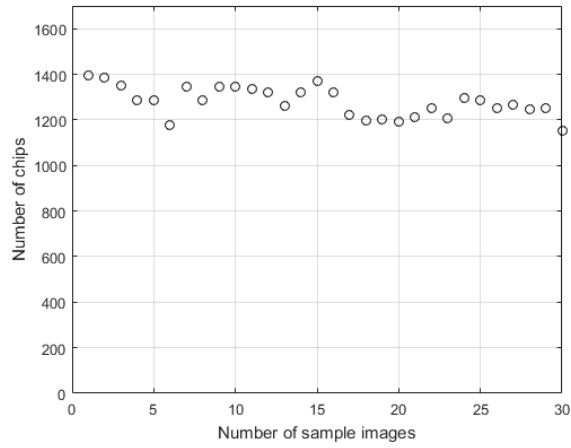
(a)
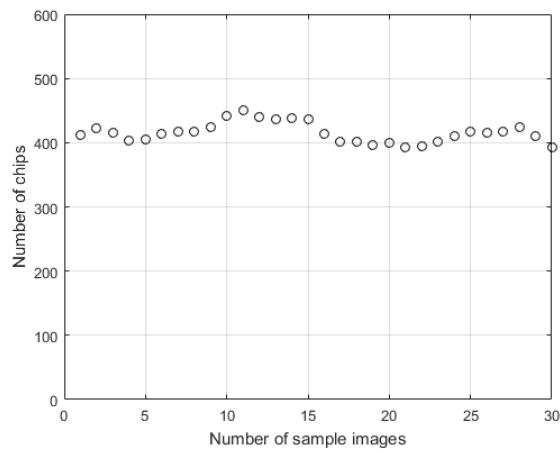
(b)
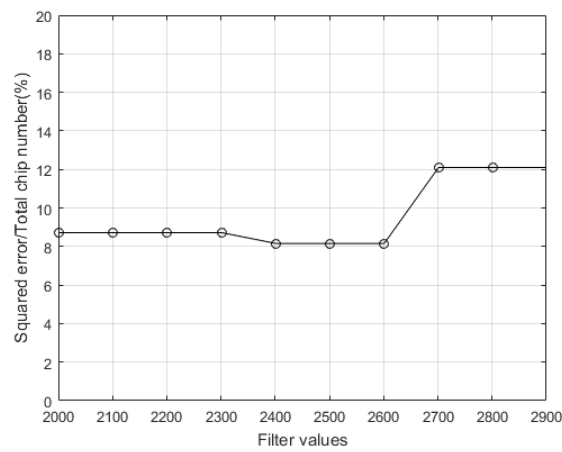
(c)

Figure 60. Reliability of number of chips and size filtering value (a) number of chips from the 30 image samples without image crop, (b) number of chips from the 30 image samples with image crop, (c) selection of the filtering values (2,400~2,600) in the simulation for the 1st experiment with 100 filtering value

The experimental results are compared with the simulation. The simulation is

performed in the same conditions of the experiment except the number of tooth passes and the filtering values.

The number of chips from the experiment in the shearing cutting conditions is expected to be equal to the number of tooth passes. Based on this assumption, the number of tooth passes for the input in the simulation should be determined. However, the number of chips from our experiment can be affected by many experimental conditions which are difficult to control, such as the loss of the chips during the chip collecting process through the tube, the air suction and blow nozzles, and the adhesion of the tape, etc. Therefore, the number of tooth passes for the simulation is selected to be the same with the number of chips from the experiment at the feedrate of 6 mm/s which can be assumed as the shearing dominant cutting condition in our experiment so that the equal number of tooth passes can be applied to the simulation and the experiment.

In order to compare the simulation results to the experimental results, two 'filtering' values need to be selected: one for the simulation and one for the chip counting algorithm for the experimental data. Both filtering values specify the smallest chip that should be counted. The filtering values depend on the conditions of the chip counting system which includes unpredictable experimental conditions such as the change in the image quality due to the unfixed depth of focus of the microscope due to the flexible tape, and the size of the chips that are produced, etc. Hence, the filtering values for the simulation are inversely predicted from the experimental results. To find the filtering values for the simulation which minimize the difference in the number of chips between the simulation and the experiment, the squared error between the numbers from the simulation and the experiment is calculated as shown in Fig. 60(c).

The filtering value of 2,400~2,600 is selected in the simulation to minimize the error (squared error/total num. of chips: %) down to 8.15 % for the 1st experiment with the filtering value of 100 in the experiment. The number of chips counted under conditions of no size filtering from the six sets of experiments are listed in Table 5. The trend of the change in numbers is compared with the simulation as shown in Fig. 61. In Table 6&7, the number of chips with the experiment size filtering values of 100 and 150 are listed. And the trends are shown in Fig. 62 & 63. The number of chips tend to decrease gradually as the feedrate decreases from the highest feedrate 6 mm/s to the lowest feedrate 1 mm/s. The number of chips from the experiments 2, 3, 4, and 6 tend to decrease gradually with no experiment size filtering. The number of chips from experiments 1 and 5 decrease without consistency. The result from the experiment 5 slightly increases. The number drop is not significant around the critical feedrate. The simulation results show a small decrease when the feedrate is crossing the critical feedrate. The error is between 6.72 ~ 17.9 %

In the experiments 1, 2, 3, and 6, the number of chips decrease gradually with the experiment size filtering of 100. The number of chips from the experiments 1 and 3 have a tendency to decrease after the numbers which are nearly constant. In the experiment 1, the number of chips drops more than 50 % from the feedrate of 3 mm/s to the feedrate 1 mm/s crossing the critical feedrate. In the experiments 2, 3, and 4, the number drops more than half between the feedrate of 4 mm/s and 1mm/s. In the other results, the number of chips either decreases gradually without any large drop or the increase and decrease alternates. The simulation shows a large drop in numbers when the feedrate is crossing the critical feedrate. The error is within the range of 7.96 ~ 19.67 %. The experiments with the experiment size filtering of 150 have the error

Table 5
Number of chips from the cutting experiments and the simulation (no size filtering for experiment)

Number of Chips(No size filtering)

Feedrate(mm/s)	Ex1	Ex2	Ex3	Ex4	Ex5	Ex6
1	524	671	750	549	675	826
2	631	699	898	551	662	975
3	743	739	869	630	916	1302
4	665	725	1136	741	731	1467
5	770	876	1227	689	844	1459
6	655	836	1220	691	620	1497
Cutting edge radius(μm)	3.32	1.78	2.69	2.12	2.21	4.05
Critical Feedrate (mm/s)	2.65	1.42	2.15	1.69	1.77	3.24

Simulation Control Parameter

	Ex1	Ex2	Ex3	Ex4	Ex5	Ex6
Num. of tooth passes	655	836	1220	691	620	1497
Filtering($\times$ 1000)	1.6-1.7	1.1~1.6	1.5~1.6	1.5~2.6	1.1	2.4
Error (%) (Squared error / total num. of chips)	8	8.97	10.28	7.22	17.9	6.72
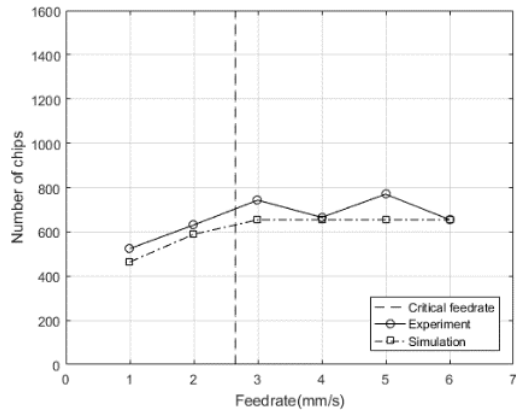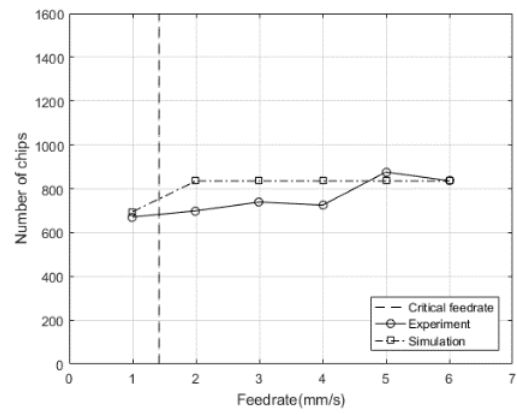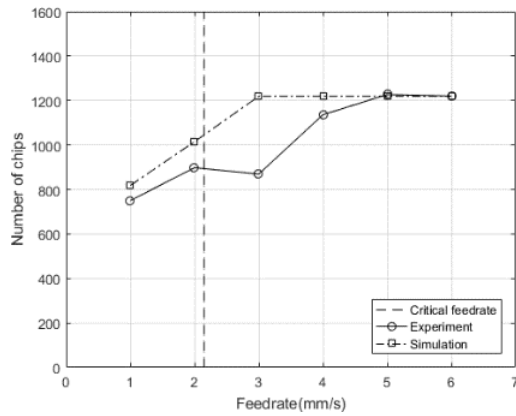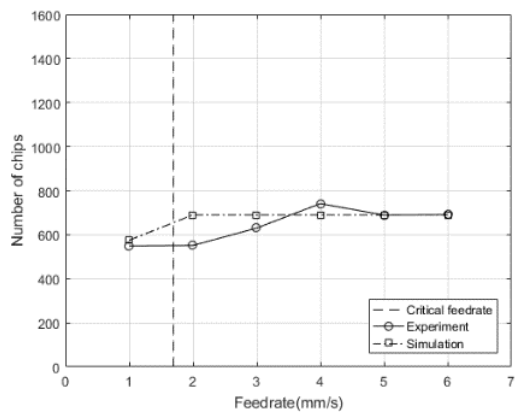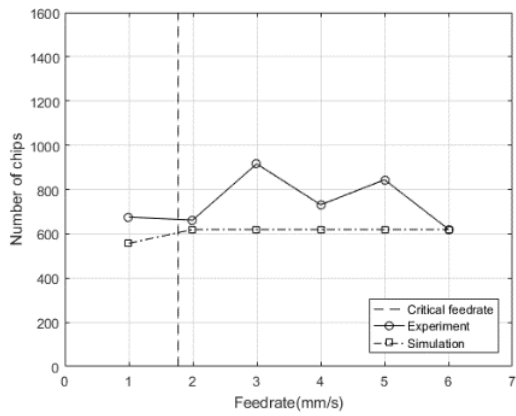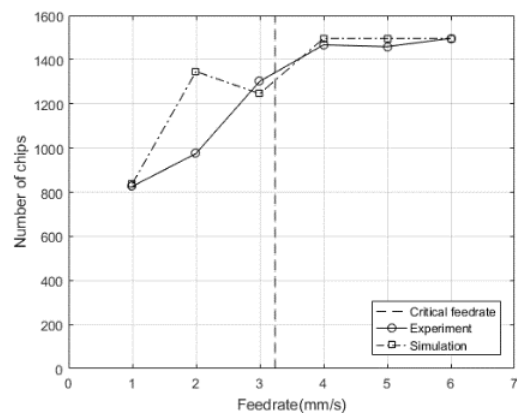
Figure 61. Number of chips from experiments with no experimental size filtering (a)experiment 1, (b)experiment 2, (c)experiment 3, (d)experiment 4, (e)experiment 5, (f)experiment 6

Table 6
Number of chips from the cutting experiments and the simulation (Size filtering for experiment : 100)

Number of Chips

Feedrate (mm/s)	Ex1	Ex2	Ex3	Ex4	Ex5	Ex6
1	123	156	115	134	208	138
2	211	255	166	189	250	199
3	269	247	226	202	316	330
4	279	321	286	300	287	363
5	300	341	286	235	310	398
6	276	368	295	283	256	466

Simulation Control Parameter

	Ex1	Ex2	Ex3	Ex4	Ex5	Ex6
Num. of tooth passes	276	368	295	283	256	466
Filtering(× 1000)	2.4~2.6	2~8	1.9~2.6	2.7~6.3	1.7~3	4.7~5
Error (%) (Squared error / total num. of chips)	7.96	19.67	7.79	18.32	9.77	16.95
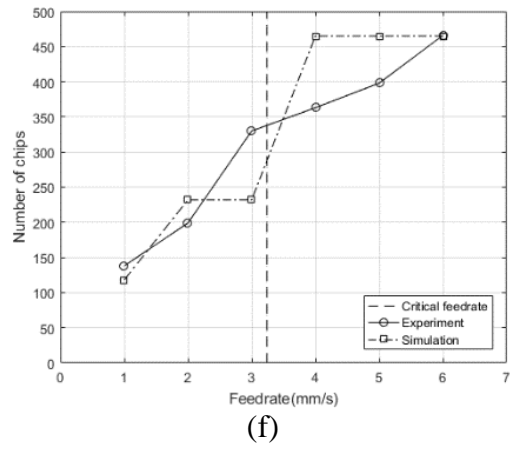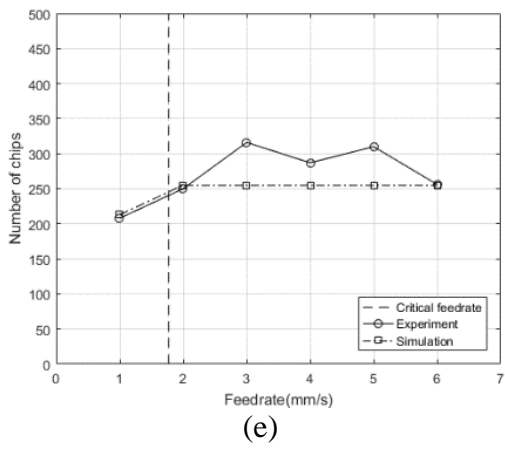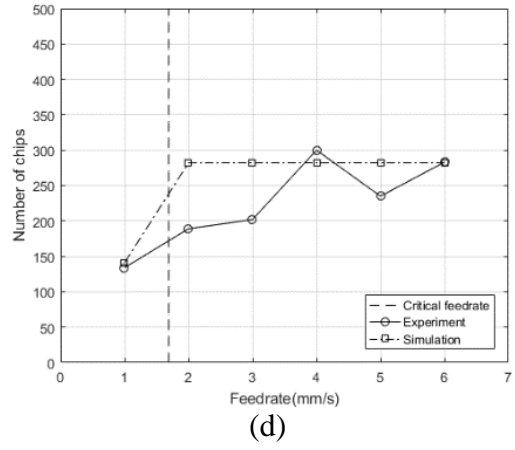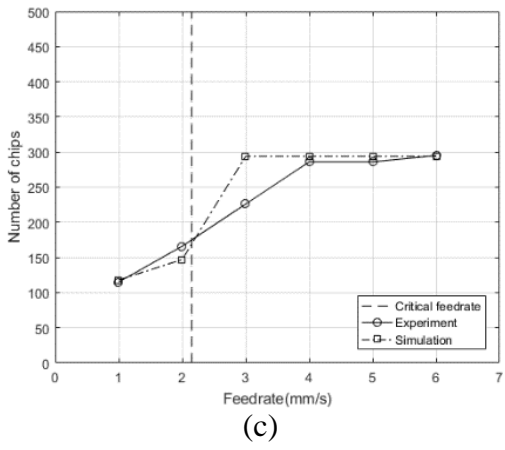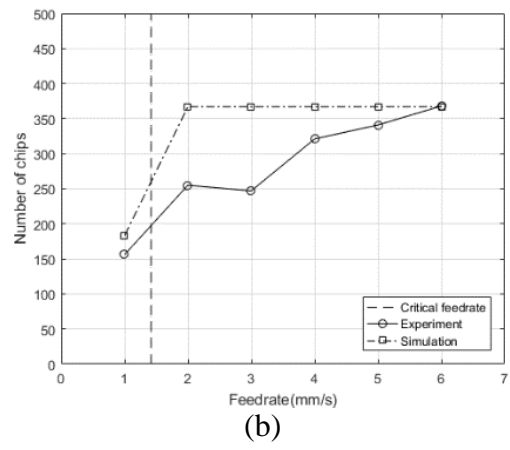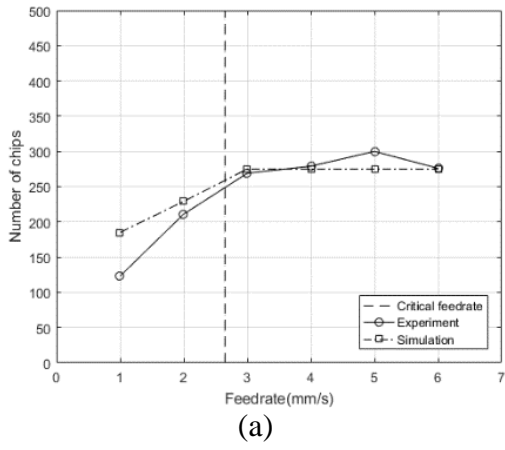
Figure 62. Number of chips from experiments with experimental size filtering of 100 (a)experiment 1, (b)experiment 2, (c)experiment 3, (d)experiment 4, (e)experiment 5, (f)experiment 6

Table 7
Number of chips from the cutting experiments and the simulation (Size filtering for experiment : 150)

Number of Chips

Feedrate(mm/s)	Ex1	Ex2	Ex3	Ex4	Ex5	Ex6
1	65	36	57	69	114	52
2	141	133	103	138	180	78
3	193	165	168	165	264	163
4	216	230	208	253	258	174
5	252	267	235	214	279	228
6	244	289	235	234	240	264

Simulation Control Parameter

	Ex1	Ex2	Ex3	Ex4	Ex5	Ex6
Num. of tooth passess	244	289	235	234	240	264
Filtering($\times$ 1000)	4.9~8.3	8.5~11	2.7~12.5	6.4~11.6	3.1~5.6	14.1~19.3
Error (%) (Squared error / total num. of chips)	11.1	20.18	12.82	15	11.16	19.29
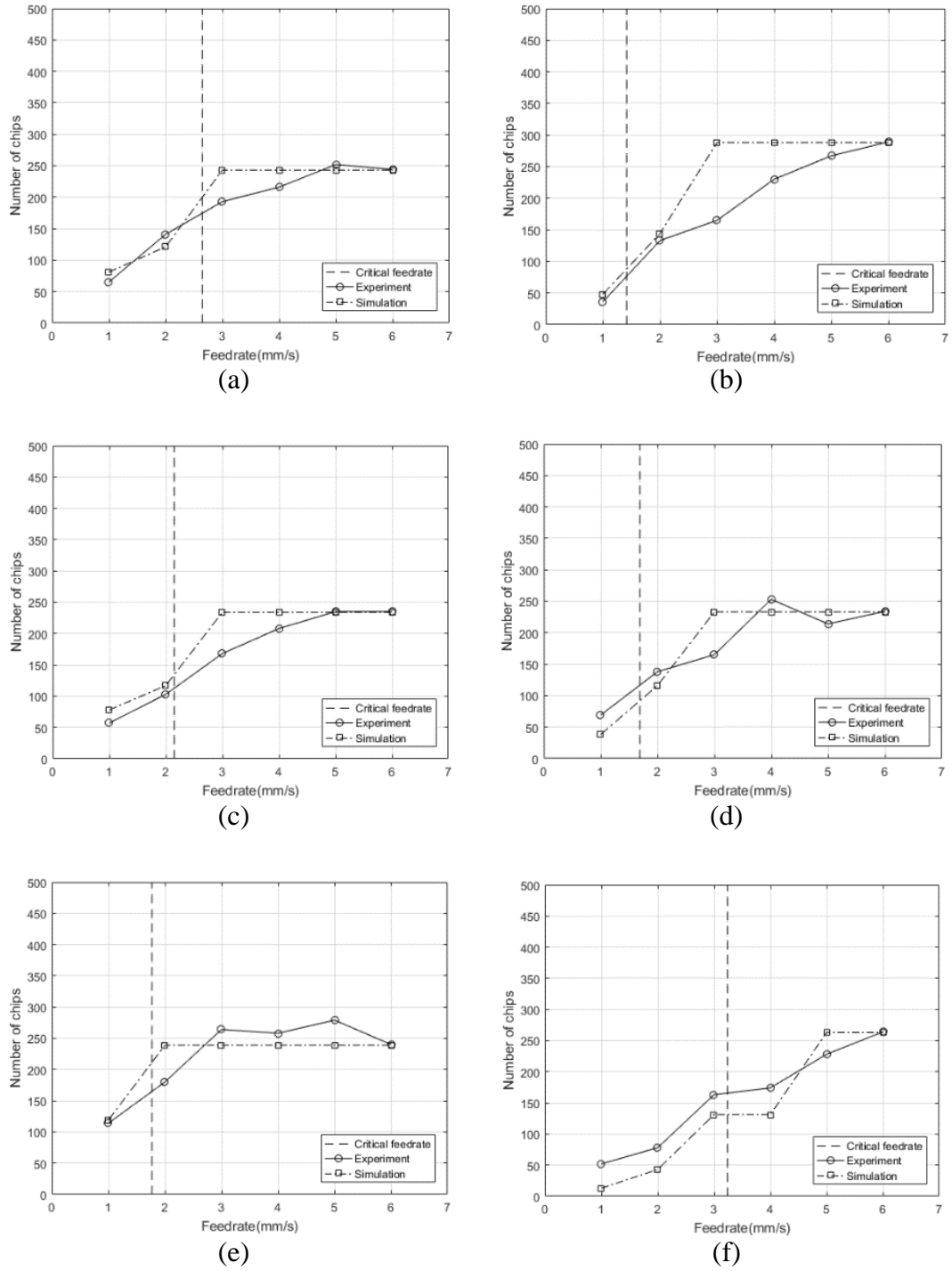
Figure 63. Number of chips from experiments with experimental size filtering of 150 (a)experiment 1, (b)experiment 2, (c)experiment 3, (d)experiment 4, (e)experiment 5, (f)experiment 6

between the experiments and the simulation of 11.15 ~ 20.18 % which is larger than the

error from the results with no filtering and the filtering of 100. In the experiments 3, 4, 5, and 6, the number of chips decreases gradually. The number of chips from experiments 1, 3, 4, and 5 tends to have numbers close to constant before the decrease in the numbers. In the experiment 4 and 5, the number of chips drops more than 50 % between the feedrate of 4 mm/s and 1 mm/s and between the feedrate of 3 mm/s and 1 mm/s, respectively.

Section 6. Summary

The chip production rate in micro-endmilling is measured using the developed chip collecting and counting system, and the results are compared with the simulation.

The experimental results show that the number of chips decreases as the feedrate decreases. In some of the results with the experiment size filtering of 100, the number of chips drops by almost half around the critical feedrate which can be calculated from the cutting edge radius.

The results show that the total reduced number of chips between the feedrate of 6 mm/s and 1 mm/s from the experiment and the simulation are almost the same. However, the large drop in the numbers from our experiments could be difficult to be distinguished from the gradual decrease. In the experiment 2, 3, and 4 with the filtering of 100 and the experiments 4 and 5 with the filtering of 150, the number drops half over more than two feedrates from 3 mm/s to 1 mm/s or 4 mm/s to 1 mm/s crossing the critical feedrate. And, the large error is mostly caused by the difference in the number of chips at the feedrate where the number drops in the simulation. Thus, the results from our experiments are not accurate enough to predict the cutting edge radius. Therefore, more investigations should be conducted in order to detect the large number drop in the experiment.

When the UCT crosses the MCT, it could be a transition zone where the cutting regime changes from the shearing to the ploughing as shown in Fig. 64(a). The transition zone can be detected by measuring the cutting force [130]. From our experimental results, the transition zone could be detected by counting the number of chips as shown in Fig. 64(b). Our method could be less expansive than the any other transition zone detecting method.
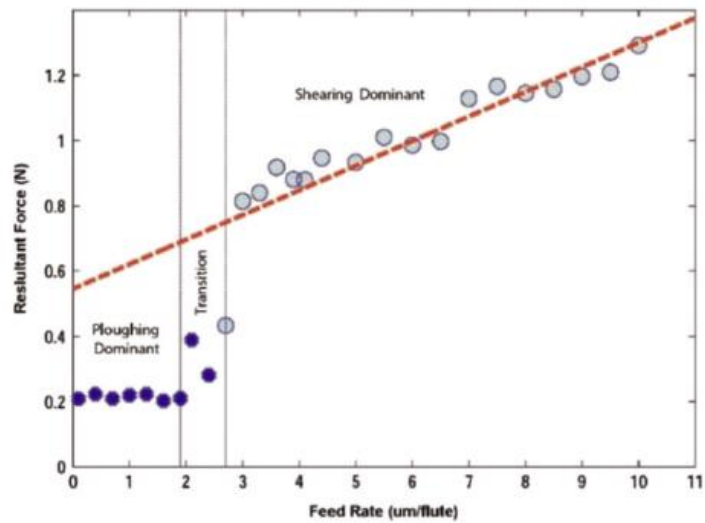
(a)
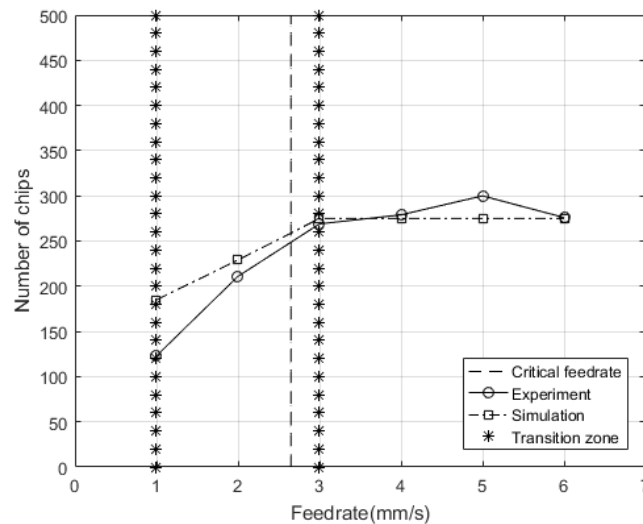
(b)

Figure 64. Transition zone detection(a)identification of the transition zone using the cutting force measurement from the ploughing dominant region and the shearing dominant region[130], (b)identification of the transition zone using the number of chips from the ploughing dominant region and the shearing dominant region.

In order to improve the surface quality and the machining accuracy, avoiding the ploughing cutting regime is recommended. When the number of chips starts to decrease during the machining process, the cutting mechanism changes from the shearing to the ploughing regime entering into the transition zone. At that moment, the feedrate needs to be increased up to a certain point to maintain the shearing dominant regime where the chip numbers show a nearly constant amount.

This operation could be performed as an online chip counting process which can be applied to the micro-milling system to automatically feedback the tool wear data to the machine to optimize the machining parameters.

The tool run-out which might affect the number of chips is not considered due to the difficulties of measuring the run-out from the $200 \ \mu m$ tool. The chatter stability is not taken into account in the decision of the spindle speed and the depth of cut. Since the tool is small, it is difficult to investigate the structural dynamics of the cutting system which is the most essential part in the chatter stability analysis Therefore, in chapter 7, an investigation is made on the chatter stability of our micro-milling machine.

In the next chapter, the reliability of the proposed method of estimating the cutting edge radius is investigated by analysing the data obtained from the experiments.

CHAPTER 5

DATA ANALYSIS

In this chapter, the reliability of the previously developed cutting edge radius estimator is evaluated. This estimator predicts the cutting edge radius by detecting the decrease in the number of chips as the edge slips over the workpiece when the MCT becomes larger than the UCT, thus transitioning from the shearing to the ploughing dominant region. The estimator can be divided into two parts: the chip collecting part and the chip counting part. The chip collecting part sucks the chips while cutting by using the air vacuum pump. And the air is discharged onto the adhesive tape so that the chips can be attached onto the tape. The chip counting part counts the chips by taking an image of the tape with the chips attached using a microscope and by applying image processing. There are many uncertainties in the pneumatic system and the image processing. So, these uncertainties may deteriorate the accuracy of the estimation. Therefore, this study evaluates the reliability of the newly proposed cutting edge radius estimator.

Section 1. Review on chip production rate simulation and experiment

A chip production rate simulation has shown that the number of chips produced decreases when the MCT becomes larger than the UCT[18]. It has also been confirmed through experiments that the number of chips tends to decrease under these conditions. In the previous simulation and experiment, the MCT was fixed by setting the cutting edge radius as constant for the ease of the experiment. The change in the number of chips was observed when the UCT was made smaller than the MCT by decreasing the

feedrate[139].

The cutting edge radius of the tool used in this previous experiment was measured to calculate the corresponding MCT and the corresponding critical feedrate as well. The cutting edge radius was measured from the experiment and the measurements were used in the simulation. The measured cutting edge radius could have an inherent error in the direct measuring process using a microscope and image processing. Therefore, the measuring procedure should be conducted in a very careful manner. 10 measurements were made for each cutting edge image from experiment 1 to 6 and the means and standard deviations are listed in Table 8 and shown in Fig. 65.
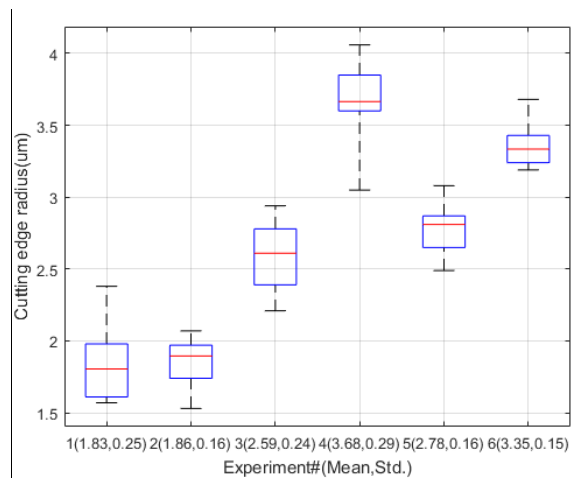
Figure 65. Box plot of cutting edge radius with mean and standard deviation

Table 8
Cutting edge radius with mean and standard deviation

Exp.	Cutting edge radius	
	Mean(μm)	Std.(μm)
1	1.83	0.25
2	1.86	0.16
3	2.58	0.24
4	3.68	0.29
5	2.78	0.16
6	3.35	0.15

The next section explains the process of finding the conditions under which the proposed cutting edge radius estimator will perform best.

Section 2. Calibration

The cutting edge radius estimator can be considered as a kind of sensor that measures the cutting edge radius by detecting the chip number drop. The sensor needs to be calibrated whenever the operating conditions change. The purpose of the calibration for this sensor is to detect the drop in the number of chips more accurately. Previous studies have shown that a large drop in the number of chips can be seen in the number of chips above a certain size[18, 139]. The calibration of this sensor is to find the appropriate threshold of size filtering to filter out chips smaller than a certain size and to count only the number of large chips.

In a chip production rate simulation, the volume of the chips is calculated. The unit for the size filtering threshold values for simulation is in μm^3. In the experiment, the chip size is obtained from the 2-D images. Therefore, the unit for the size filtering values for the experiment is in pixels. Since the values have different units, they are considered separately.

First, the size threshold for the simulation is found as follows: The simulation results of the chip number with three different cutting edge radii are shown in Fig. 66. The chip production rate simulation requires a value for the number of tooth passes as an input parameter. The number of tooth passes for the simulation is determined based on the experimental set-up as follows: The size of the image is 1900 pixels by 1400 pixels, and the conversion factor from pixel to mm is 0.0048 mm/pixel. The length of the image of the tape which is 1900 pixels is used to calculate the time taken for the tape to travel a distance corresponding to 1900 pixels. The cutting time can be calculated from the tape speed and the size of the image. From this information, the number of tooth passes during the time is estimated as 1,469.

Increasing the size filtering threshold reduces the number of chips as it filters more chips smaller than the threshold. The proper size filtering threshold should be a value within a range that allows for the detection of large drops in the number of chips at the critical feedrate. For example, in Fig. 66(a), if the critical feedrate is 1.6 mm/s, the number of chips drops sharply from feedrate 2 mm/s (above the critical feedrate) to 1 mm/s (below the critical feedrate) at the size filtering threshold of 5,000. Similarly, in Fig. 66(b), if the critical feedrate is 2.4 mm/s, the number of chips has a large drop between feedrate 3 mm/s (above the critical feedrate) and 2 mm/s (below the critical feedrate) with the size filtering threshold of 5,000. In Fig. 66(c), the number of chips also drops sharply between feedrate 4 mm/s and 3 mm/s at the size filtering threshold of 5,000, if the critical feedrate is 3.2 mm/s. Therefore, the proper size filtering threshold for the simulation is determined to be 5,000.

Next, the size filtering threshold for the experiments is determined. In this process, the simulation results and the experimental results are linearly fitted. Experimental chip number data is collected from a set of images of chips produced during a cutting process. 30 images are taken in each feedrate as explained in section 5 in chapter 4. Therefore, 180 images are taken in each experiment. From each set of 30 images, 20 images are randomly selected as the training data and the remaining 10 images are used as the testing data. The training data is used for the calibration process.

In order to find the experimental size filtering threshold that gives the maximum R-squared value, the filtering threshold is swept from 20 to 450.
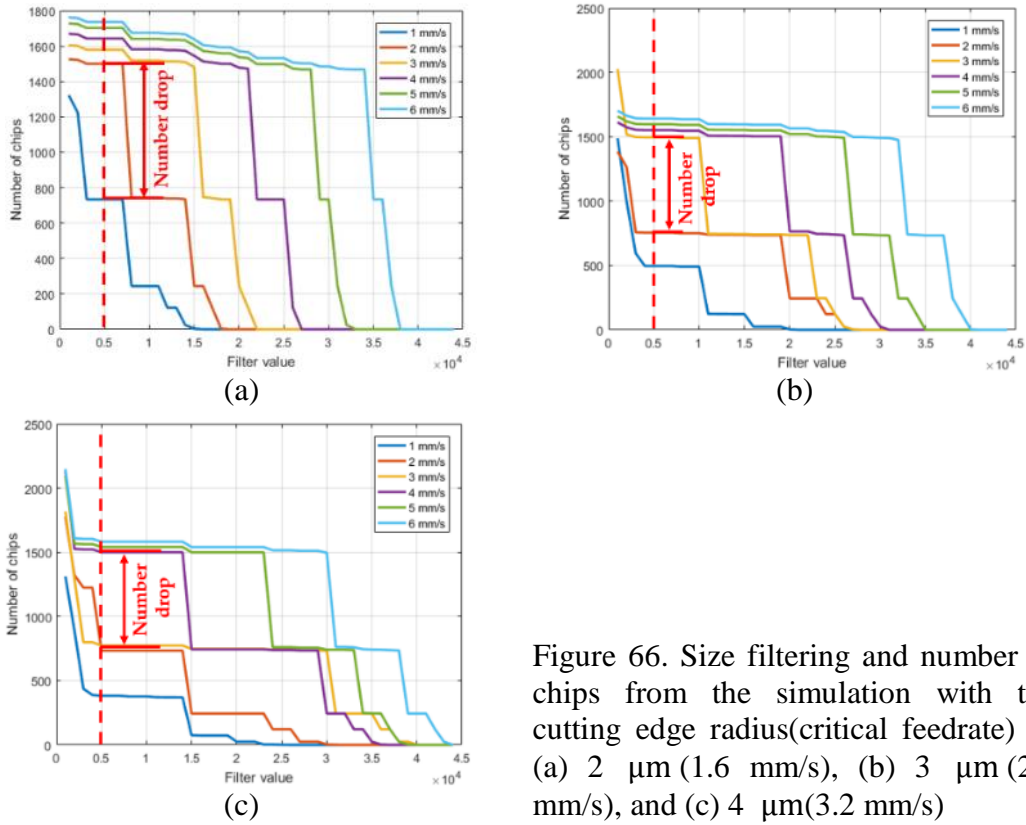
Figure 66. Size filtering and number of chips from the simulation with the cutting edge radius(critical feedrate) of (a) 2 μm (1.6 mm/s), (b) 3 μm (2.4 mm/s), and (c) 4 μm(3.2 mm/s)

The maximum R-squared values are selected between the filtering thresholds of 20~250, since the number of chips becomes significantly small when the threshold becomes larger than 250 as shown in Fig. 67. The optimum threshold is selected as listed in Table 9. The results from the linear fitting using the optimum thresholds are shown in Fig. 68.

The reason why the filtering thresholds are different for each experiment is that the experimental conditions are changed in parts that are not controlled by the system. For example, when the system equipment is dismantled and then re-assembled, there can be variations in conditions such as the distance between the microscope and the tape, the precise focus position of the microscope, and so on. Therefore, in each experiment, this calibration process should be conducted.

Table 9
Optimum experimental filtering threshold with maximum R-squared value

Exp.	Optimum filtering threshold	Experimental filtering threshold		
		Maximum r-squared	Slope	y-Intercept
1	47	0.83	0.14	63.76
2	126	0.80	0.24	-132.23
3	124	0.88	0.15	10.46
4	150	0.85	0.13	9.46
5	172	0.94	0.14	-14.48
6	116	0.91	0.23	-36.81

(a)   (b)
(c)   (d)
(e)   (f)
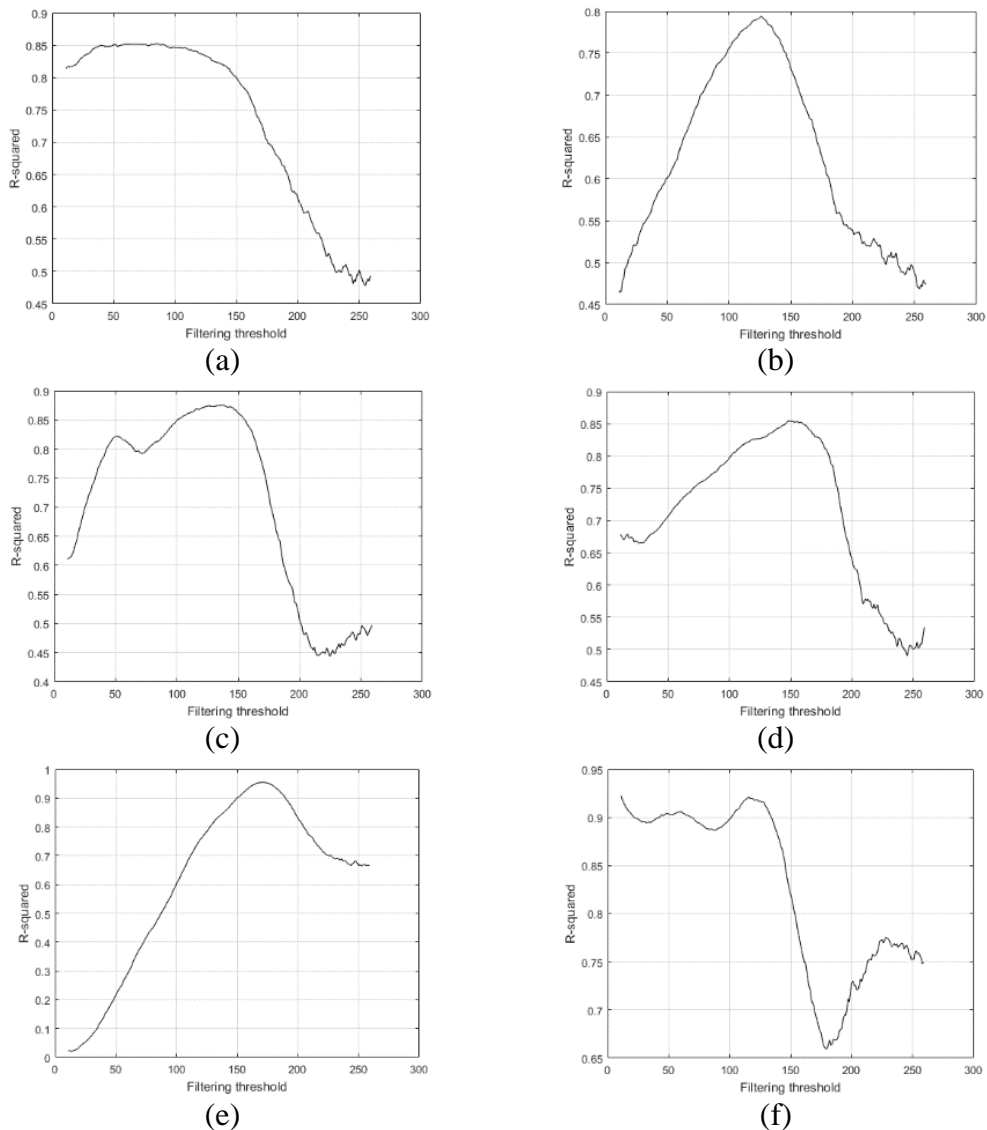
Figure 67. Relationship between the experimental filtering threshold and R-squared values from the linear fitting from (a) exp. 1 to (f) exp. 6
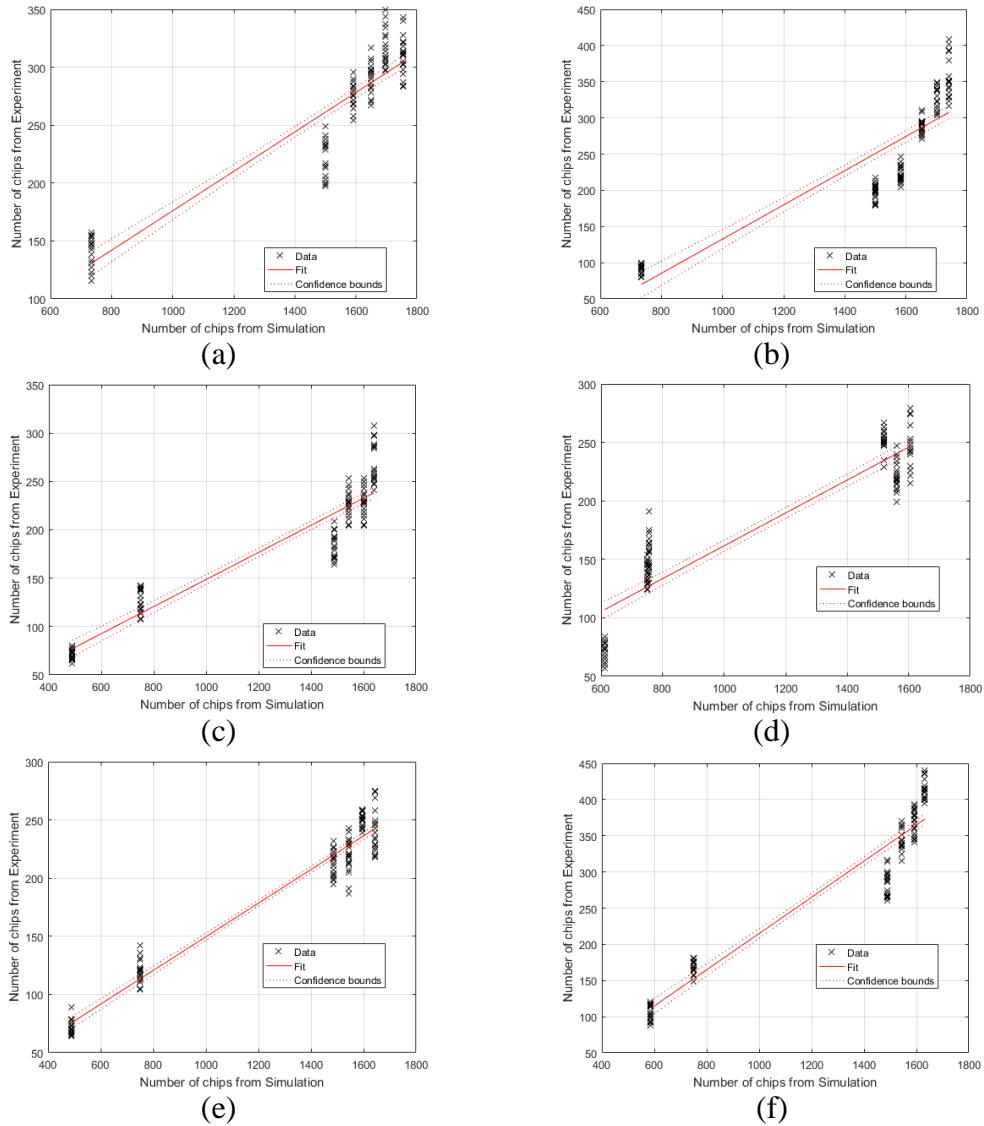
Figure 68. Linear fit of the number of chips from the simulation and the experiment with the optimum experimental filtering threshold from (a) exp. 1 to (f) exp. 6

Additionally, the reason why the number of chips from the simulation and the experiment are different is due to the chip loss from the chip collecting part and the image crop in the image processing in the chip counting part. The number of chips counted from the images before the crop is around 1,280 which is 87% of the estimated number of tooth passes (1,469) in a single image as shown in Fig. 60 in chapter 4. This indicates that around 13% of produced chips are lost in the chip collection process. However, the image crop is then conducted to increase the accuracy in the chip counting.

The image is cropped to 64% of the original image, causing an expected difference of 36% between the produced and counted number of chips. Moreover, the number of chips decreases as the size filtering value increases. To obtain the optimum size filtering value, the number of chips from the experiments becomes smaller since the size filtering values should be applied to obtain the number drop.

As a final step of the calibration, the optimum drop detection threshold should be obtained. The key to the cutting edge radius estimation is to detect the drops in the number of chips when the MCT becomes larger than the UCT. After finding the first calibration parameter (size filtering threshold) of the estimator, the number of chips obtained from the experiment is applied as the input signal. The output signal of the sensor can be obtained as shown in Eq. (12).

$$Output = \frac{(Input - Offset)}{Slope} \qquad (12)$$

Eq. (12) is the sensor response curve for this estimator. The offset and slope values are obtained from the first calibration process.

In order to see the result after the first calibration, Eq. (12) is applied to the testing data to get the output data from the calibrated estimator. In this experiment, it is important to detect the drops in the number of chips as the feedrate crosses the critical feedrate. However, not only does the number of chips drop when the feedrate crosses the critical feedrate, but also the number of chips drops between the other feedrates as shown in Fig. 69. Therefore, an additional process is needed to be able to distinguish the number drop at the critical feedrate from the other number drops at the other

106

feedrates.

We begin by proposing that the drop in the number of chips at the critical

feedrate is larger than the drops that occur at other feedrates.
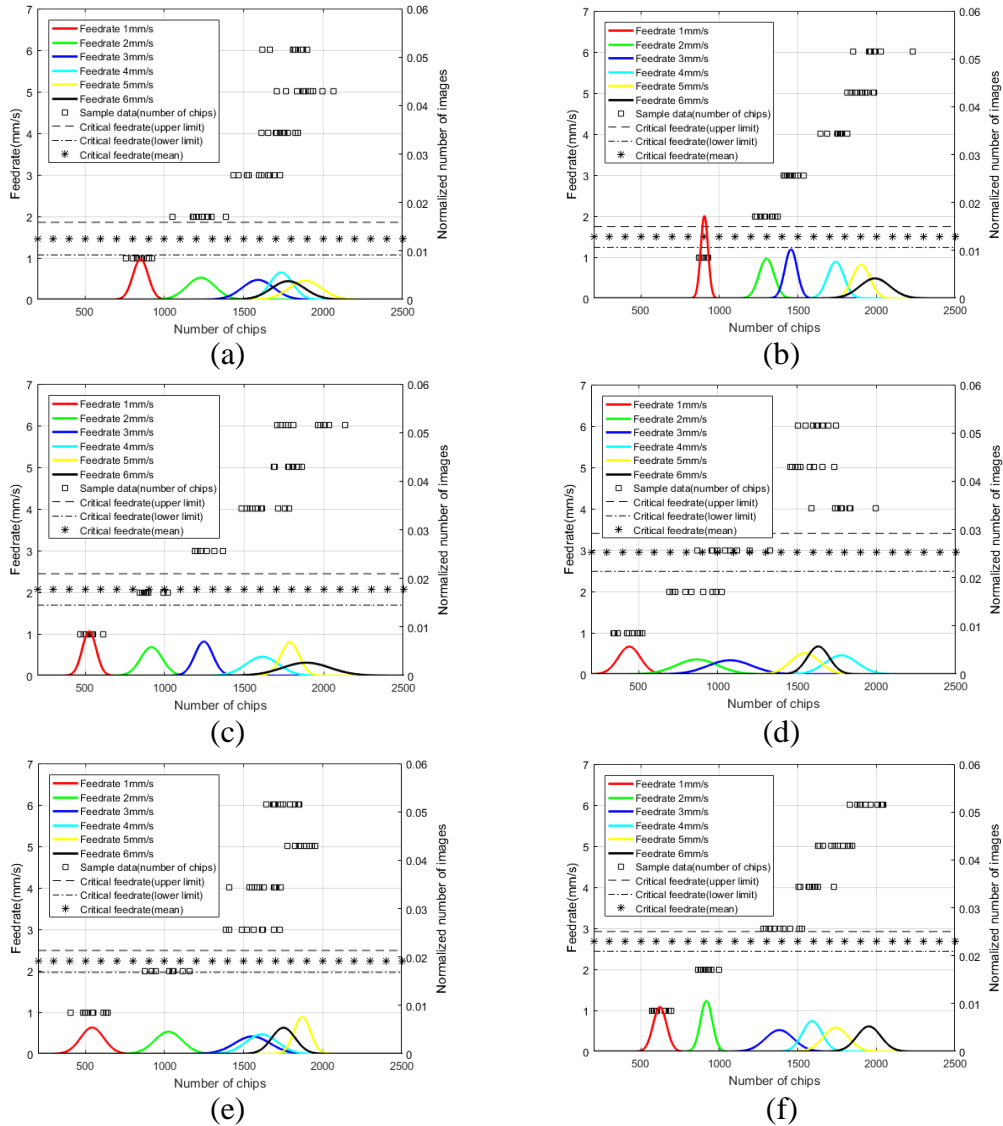
Figure 69. Normal distribution of the output signal and the critical feedrate boundary(Mean, Std.) from (a) Exp. 1 (1.46 mm/s, 0.196 mm/s), (b) Exp. 2 (1.49 mm/s, 0.127 mm/s), (c) Exp. 3 (2.07 mm/s, 0.188 mm/s), (d) Exp. 4 (2.94 mm/s, 0.23 mm/s), (e) Exp. 5 (2.23 mm/s, 0.132 mm/s), and (f) Exp. 6 (2.68 mm/s, 0.12 mm/s)

In order to distinguish the large drop from the other small drops, a drop

detection threshold is introduced. This threshold represents the decrease in the chip

107

number in percentage. For example, when the number of chips is reduced by 20% between feedrate 3 mm/s and 2 mm/s and the other drop is 30% between feedrate 2 mm/s and 1 mm/s, the feedrate range between the feedrate of 2 mm/s and 1 mm/s is selected with the threshold of 25% as the critical feedrate range that includes the actual critical feedrate.

The thresholds from 10% to 50% are applied to the training data to find a value that gives the highest probability of estimation as shown in Fig. 70. The optimum threshold and the maximum probability values are listed in Table 10. A method of estimating the cutting edge radius and obtaining the probability of estimation is described in the next section.

Section 3. Physical interpretation of calibration

In the calibration process, the size filtering and the drop detection threshold values are used. The size filtering threshold is needed in order to see the drop in the number of chips in the simulation as well as in the experiment. This means that the drop can be seen only with the chips larger than the threshold. In other words, chips smaller than the threshold obscure the observation of the MCT effect.

Table 10
Optimum drop detection threshold and maximum probability of estimation

Exp.	Probability of estimation and threshold (%)	
	Optimum threshold (%)	Max. Probability (%)
1	27	78
2	23	99
3	25	62
4	31	77
5	25	92
6	25	97
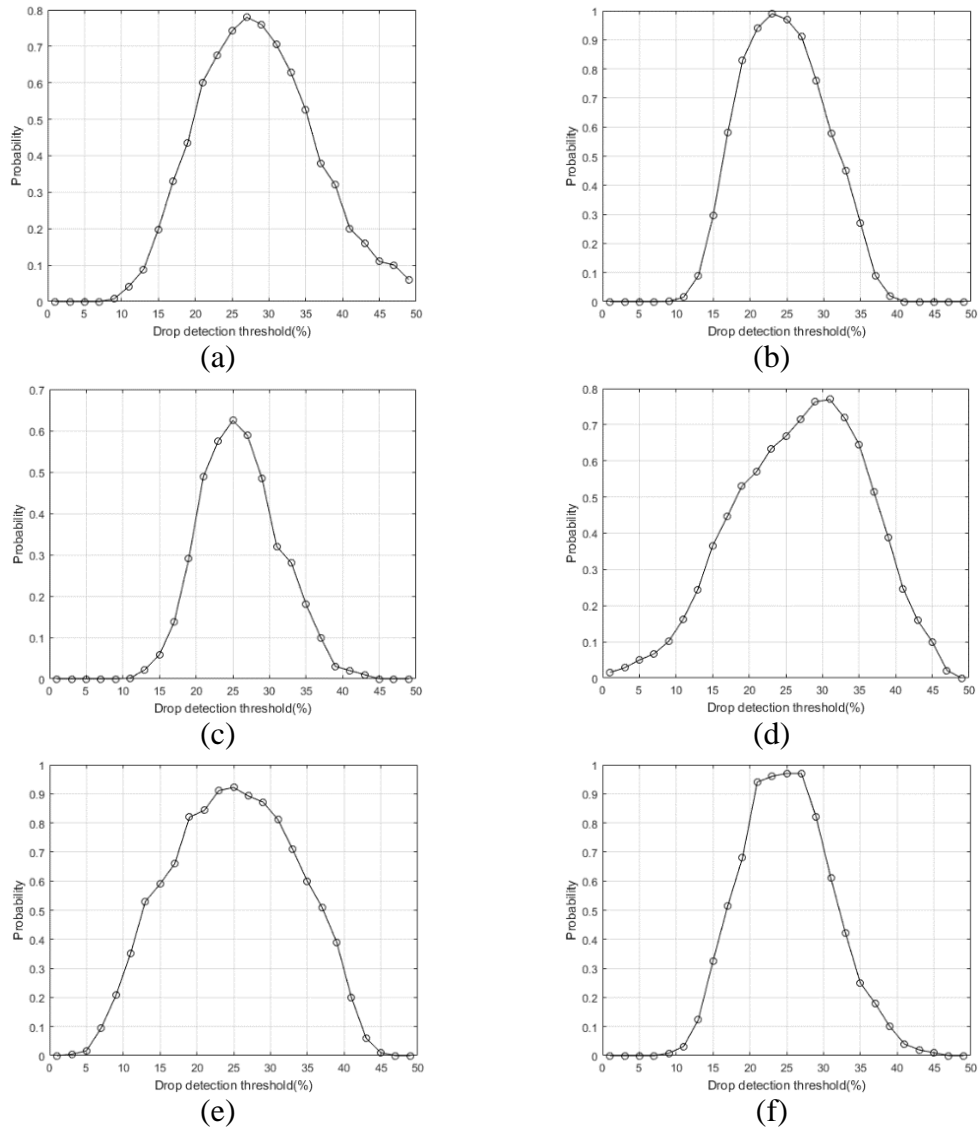
Figure 70. Drop detection threshold and probability of estimation (a) exp.1 to (f) exp.6

Also, the drop detection threshold is applied in the calibration process because the drop in the number of chips occurs in multiple feedrate ranges making it difficult to distinguish the feedrate range which is including the critical feedrate from the other feedrate ranges with the drop in the number of chips. According to the simulation results, the number drop should occur at a single feedrate range which is including the critical feedrate. And, the assumption that the critical feedrate is constant during the cutting process has been made. However, in the real cutting process, the cutting edge radius

would change due to the tool wear changing the critical feedrate during one set of experiments. Therefore, the drop in the number of chips could occur in multiple feedrate ranges. Additionally, the ploughing effect which changes the chip production rate might occur even when the UCT is larger than the MCT before the expected feedrate range due to other reasons such as tool run-out or tool deflection which are not considered in this research.

Section 4. Cutting edge radius estimation

In order to evaluate the reliability of the cutting edge radius estimator, the probability of detecting the drop in the number of chips between the feedrates above and below the critical feedrate should be investigated.

In Fig. 71, a flow chart which explains how to calculate the probability of correctly estimating the cutting edge radius is presented. In this calculation, only the testing data is used. 10 images that are not used in the calibration are selected from each different feedrate as the testing data. The difference in the number of chips is calculated as follows: the difference between the number of chips at feedrate 6 mm/s and the number of chips at feedrate 5 mm/s is calculated. Then, the difference between the number of chips at feedrate 5 mm/s and the number of chips at feedrate 4 mm/s is calculated. In this order, the difference between the number of chips at feedrate 2 mm/s and the number of chips at feedrate 1 mm/s is calculated at the end. This process creates a new sample composed of the number differences that is used for the drop detection. The total number of this new set of samples is 10^6 since each data set from 6 different feedrates has 10 distinct numbers. Among those samples, if the number drop is detected at a certain feedrate range and the actual critical feedrate is in that range, then the

estimation is successful. The probability of estimation can be obtained by dividing the number of successful estimation by the total number of samples.

Section 5. Result

The cutting edge radius estimator is calibrated for each experiment, utilizing only the training data. The estimator is then applied to the testing data. The optimum size filtering threshold, the optimum drop detection threshold, the slope, and the offset values are used in the probability calculation.

The accuracy of the estimator is evaluated by calculating the probability of having the actual critical feedrate in the estimated critical feedrate range as listed in Table 11.

Table 11
Probability of critical feedrate estimation from (a) exp.1 to (f) exp.6

Exp.	Actual critical feedrate(mm/s) (Mean($\pm$Std.))	Probability of estimation (%)				Good estimation
		Estimated critical feedrate				
		1~2 mm/s	2~3 mm/s	3~4 mm/s	4~5 mm/s	None
1	1.46($\pm$0.20)	76.95	13.00	0.00	0.00	10.05
2	1.49($\pm$0.13)	98.81	0.49	0.01	0.00	0.69
3	2.07($\pm$0.19)	17.29	64.91	17.05	0.75	0.75
4	2.94($\pm$0.23)	7.27	74.29	18.44	0.00	0.00
5	2.23($\pm$0.13)	4.92	92.67	0.32	2.10	2.10
6	2.68($\pm$0.12)	2.01	96.66	1.22	0.00	0.11
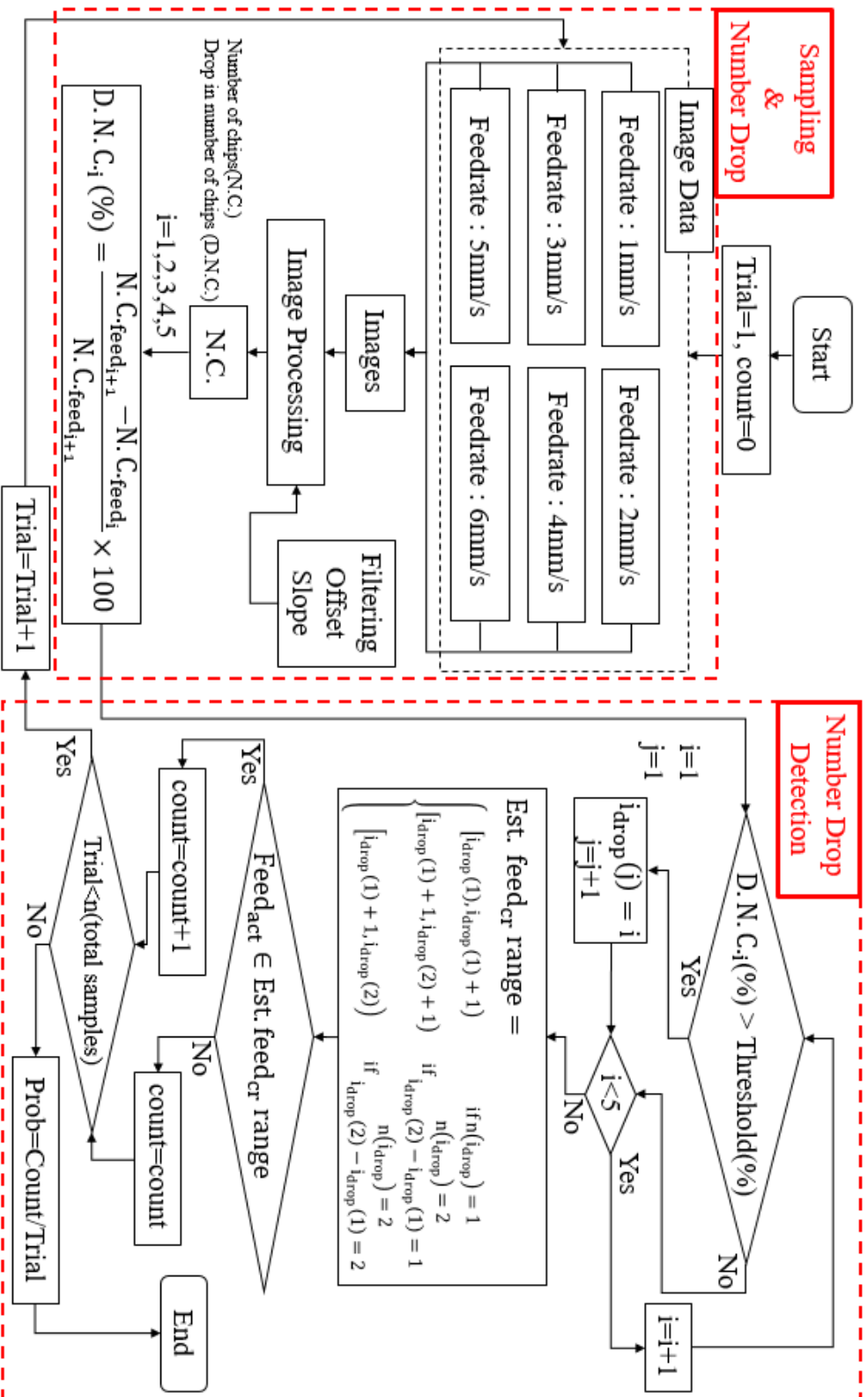
Figure 71. A flow chart of calculating the probability of estimation

Only the feedrates from 1 mm/s to 4 mm/s are shown in the results since the actual critical feedrates are in the smaller range of 1 mm/s and 2 mm/s. When the number drop could not be detected, the probability of 'none detected' is also considered. And, the resolution of the estimation is limited to 1 mm/s due to the feedrate increment of 1 mm/s.

In Exp. 1, the actual critical feedrate is correctly estimated to within 1 mm/s with a probability of 76.95%. But, there are 10.05% of samples without any drop detection. In Exp. 2, the actual critical feedrate is between 1 mm/s and 2 mm/s, and this is correctly estimated 98.81% of the time. In Exp. 3, the actual critical federate of 2.07 mm/s is correctly estimated to within 1 mm/s with a probability of 64.91%. The probability of estimating wrong ranges of 1~2 mm/s and 3~4 mm/s are 17.29% and 17.05%, respectively. The probability of estimating the actual critical feedrate within 1 mm/s in Exp. 4 is 74.29%. In Exps. 5 and 6, the probability of estimating the actual critical feedrate within 1 mm/s are 92.67% and 96.66%, respectively.

Section 6. Summary

In this chapter, the reliability of a new cutting edge radius estimator based on chip production rate for micro-milling is evaluated. The size filtering threshold and the number difference threshold values can be regarded as calibration parameters, and a method of calibration is proposed and reported. A set of sample data is split into two sets: training data and testing data. The training data is used for the calibration, and the testing data is used for the evaluation. The optimum size filtering threshold values which generate the highest R-squared value from the linear curve fitting between the number of chips from the simulation and the experiment are determined in order to

produce a sensor response curve for the estimator. Also, the optimum drop detection threshold values for the maximum probability of estimation is obtained as a part of the calibration process.

The testing data is used for the evaluation of the reliability of the estimator. The results show that the probabilities of correct estimation from the experiments are more than 70% except in Exp. 3 with 64.91%.

Exps. 2, 5, and 6 show probabilities of correct estimation above 90%. In Exps. 1, 3, and 4, the standard deviation values of the actual critical feedrates are larger than the standard deviation values from the other experiments. As a result, the probabilities of wrong estimation are larger in Exps. 1, 3, and 4 than in Exps. 2, 5, and 6 due to the influence of the standard deviation on the estimation.

The critical feedrate in this experiment can be only approximated to within 1mm/s. Since the feedrate increment in the experiment is 1 mm/s, it is only possible to estimate what feedrate range the critical feedrate is within. Further experiments are needed to determine if a higher precision of estimation is possible by using a feedrate increment smaller than 1 mm/s.

Development of an online cutting edge radius estimation system is planned as a future work. If the drop in the number of chips could be detected during the cutting process, the cutting edge radius data may be able to be obtained automatically resulting in developing a cutting edge wear rate model.

In the next chapter, the simulation of the cutting edge wear rate model is performed.

CHAPTER 6

CUTTING EDGE WEAR RATE MODEL SIMULATION

In this chapter, simulation of cutting edge wear rate model based on the chip production rate in micro-endmilling is conducted in order to understand the state of the interaction between the tool and the workpiece. The purpose of conducting this simulation is to show the applicatiliby of the cutting edge radius estimator to the online system. If the cutting edge radius estimator developed in this study is applicable to the online system, a lot of cutting edge wear data can be collected. Based on the data collected, a cutting edge wear model can be created. Our proposed cutting edge wear rate model can be useful in improving the tool life and the surface quality by estimating the tool wear.

Section 1. Background

The h_u which represents the UCT can be calculated in terms of the feedrate(f), number of teeth(n), and spindle speed(N) as Eq. (11).

$$h_u = \frac{f}{nN} \qquad (11)$$

The h_m(MCT) can be approximated as 1/3 of r_e(cutting edge radius) as Eq. (12).

$$h_m = 0.3r_e \qquad (12)$$

When the MCT crosses the UCT due to the increasing cutting edge radius from the cutting edge wear, the number of chips decreases[18]. At the moment that the MCT crosses the UCT, they are equal. The cutting edge radius can be estimated in terms of

the spindle speed, number of teeth, and the feedrate by putting Eq. (11)&(12) together as Eq. (13).

$$\frac{f}{nN} \approx h_u = h_m \cong 0.3r_e \qquad\qquad (13)$$

After the number of chips starts to decrease and the estimation of the cutting edge radius is made, the feedrate is increased to make the UCT larger than the MCT so that the cutting occurs in the shearing regime again generating one chip per tooth pass as shown in Fig. 72. As the cutting time increases, the MCT becomes larger than the UCT again due to the cutting edge wear and enables another estimation of the cutting edge radius. And, the cutting edge radius data can be collected until the tool breaks. From the data, the cutting edge wear rate could be obtained. Fig. 73 shows the flow chart of the cutting edge wear estimation. As a first step, the chip counting simulation was conducted[18].

In the simulation, the UCT model is developed base on the trochoidal tooth path of micro-endmilling process.
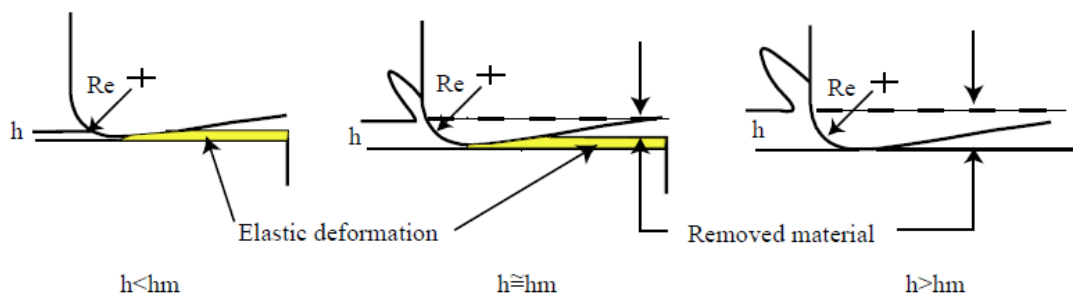
Figure 72. Schematic diagram of MCT effect (R_e:cutting edge radius, h : UCT, h_m : MCT)[4]
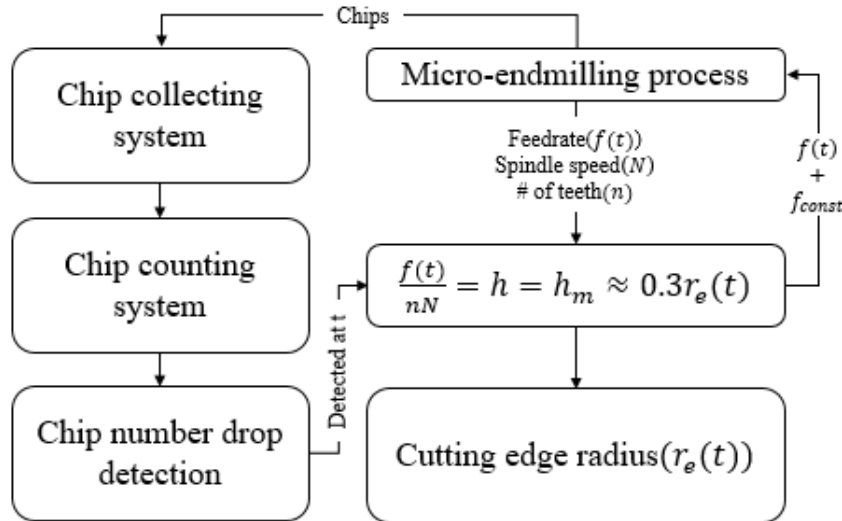
Figure 73. A flow chart of cutting edge wear estimation process

From the cutting tooth passes, only the tooth passes with the UCT larger than the MCT could remove the chip. As shown in Fig. 73(a), it was theoretically validated from the chip counting simulation that the number of chips drops in a large amount when the UCT becomes less than the MCT crossing the critical feedrate which corresponds to the measured cutting edge radius.

Section 2. Cutting edge wear rate simulation

A simulation of the cutting edge wear rate is conducted based on the results from previous research investigating the relationship between number of chips and tool wear based on an FEM simulation of the tool cutting-edge [9]. In this previous study by Thepsonthi [9], the change in the cutting edge radius was studied through the FEM simulation and the experiments. The spindle speed and the feed per tooth were 16,000 rpm and 4.5μm, respectively. The results are shown in Fig. 74(a), showing that the cutting edge radius becomes larger as the cutting distance increases. However, it does

not increase linearly, but exponentially. Therefore, Thepsonthi [9] also performed curve fitting to find the empirical cutting edge wear model from the experimental results.

As a first step in our simulation, the cutting distance from Thepsonthi [9] is changed to the cutting time to make it easy to apply to our proposed chip production rate tool wear modeling method. The cutting time t can be calculated from the cutting conditions(f_{tooth}: feed per tooth, n: number of teeth, N: spindle speed) and the cutting distance($dist_{cut}$), as shown in Eq. (14).

$$ t = \frac{60 dist_{cut}}{f_{tooth} n N} \qquad (14) $$

The cutting edge radius wear rate can be modelled by the curve fitting of the cutting edge radius data measured by Thepsonthi [9] and shown in Fig. 74(a) and the fitted data is shown in Fig. 74(b).

(a)   (b)
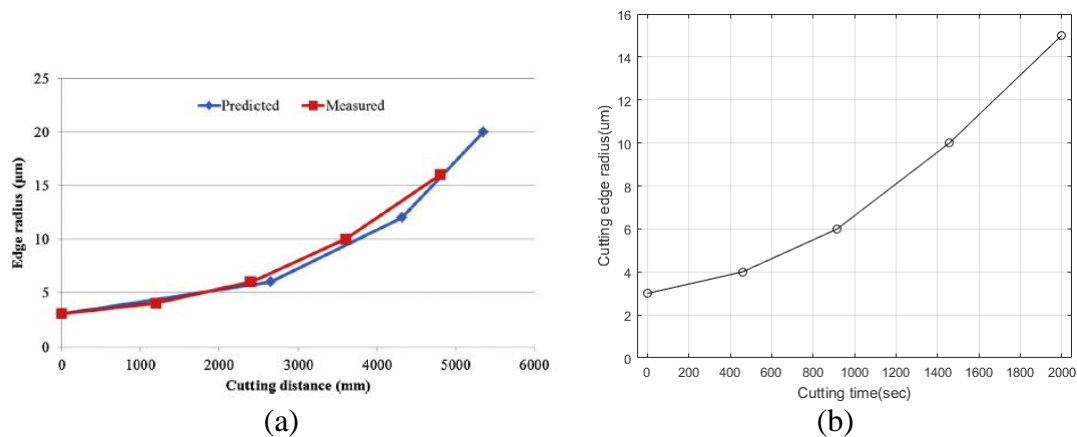
Figure 74. Cutting edge wear data(a)Comparison of measured cutting edge wear against predicted cutting edge wear by FEM simulation in micro-endmilling[9], (b)exponential curve fitting with the measured cutting edge radius data points in (a).

The exponential fit of the data has an R-square value of 0.997 with the coefficients of 2.88 and 0.0008 with 95% confidence bounds as Eq. (15).

118

$$r_e = 2.88e^{0.0008t} \qquad (15)$$

According to our previous results investigating the relationship between cutting edge radius wear and chip count, the number of chips drops at time t_i when the MCT becomes larger than the UCT. At that time, the feedrate should be increased from $f(t_i)$ to $f(t_{i+1})$ to make the UCT become larger than the MCT again. Then, as the tool continues to wear, the MCT will cross the UCT again at time t_{i+1}, resulting in another drop in number of chips.
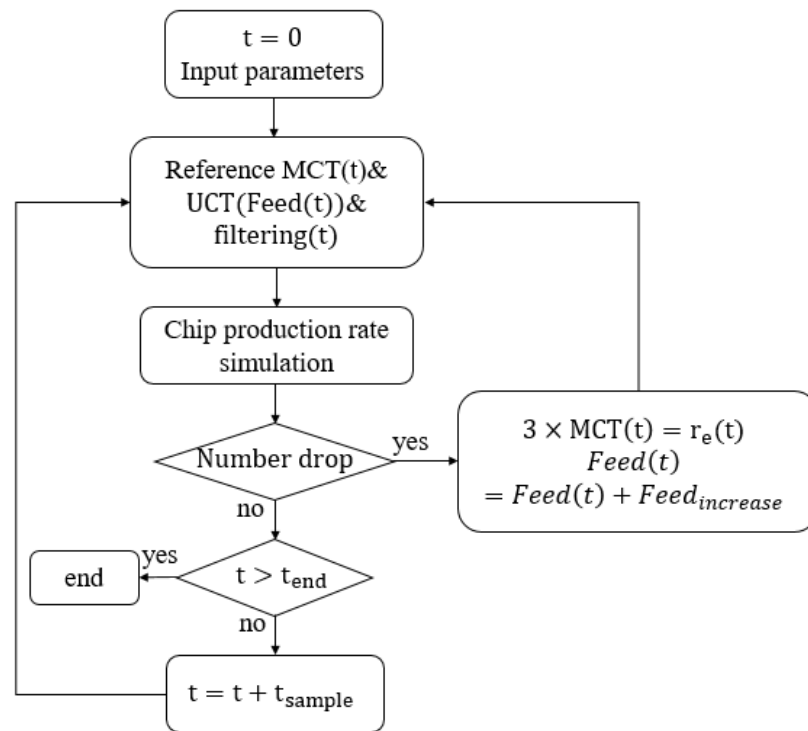
Figure 75. A flow chart of cutting edge wear rate simulation

The cutting edge wear rate simulation is conducted as shown in the flow chart in Fig. 75.

In consideration of the future experimental conditions, the input parameters for the simulation of the cutting edge wear rate are selected as listed in Table 12. This simulation includes the chip production rate simulation and the cutting edge wear model that are introduced in the previous section. In order to conduct the chip production rate simulation, the input parameters such as the tool radius, number of flutes, spindle speed, depth of cut, size filtering, number of tooth passes, and feedrate are needed. The cutting edge wear model from Thepsonthi[9] is used as a reference to calculate the MCT. Then, the MCT is compared to the UCT. The cutting edge radius is obtained eveytime when the MCT becomes larger than the UCT.

Table 12
Cutting edge wear rate simulation input parameters

Input parameters	
Tool radius (mm)	0.1
Number of flutes	2
Spindle speed(rpm)	80,000
Axial depth of cut (mm)	0.04
Filter size (μm^3)	50, 200, 300, adaptive filter
Number of tooth passes	500
Feedrate (mm/s)	3+feed increase
Cutting edge radius (mm)	Linear increase, Exponential increase[9]

Section 3. Result

Fig. 76 shows the results of the simulation. The MCT becomes larger as the cutting time increases. When the MCT becomes equal to the UCT at a critical point, the number of chips changes. The starting UCT should be above the MCT. And, the amount of increment of the feedrate applied at each of the critical points determines the number of cutting edge radius data points. Therefore, those parameters should be determined to

make enough data points for the development of the cutting edge wear rate model. The size filtering values are applied. The size filtering value is the volume of the removed chip from the workpiece. In order to see the influence of the size filtering on the chip numbers, the values of 50, 200, and 300 are applied. The reason for the application of the size filtering value is to remove the small chips that might not be able to be detected in the future experiment[18, 139, 140].

Two different cases, the linear and the exponential cutting edge wear rate model, are considered. In the linear case with the size filtering value of 50, the number of chips increases as the cutting time increases. Especially, the number of large chips is increased due to the slipping tooth on the cutting surface. But the size filtering value is not large enough resulting in the increase in the number of chips without any large drop in number but generating the small drops as shown in Fig. 76(a). In the figure, the first drop is at 360 sec and it drops again at 880 sec, 1,360 sec, and 1,880 sec. After the first drop, the feedrate is increased by 1 mm/s to make the UCT becomes larger than the MCT again. Four cutting edge radius data points are obtained.

The expected results should have constant number of chips through out the whole cutting time except the time when the number drops. Therefore, the larger filtering size values of 200 and 300 are applied to exclude the bigger chips from the results.

In the result with filtering size value of 200, the drop occurs at 280 sec, 840 sec, 1,360 sec, and 1,840 sec. But the number of chips still increases after the third drop as shown in Fig. 76(c). When the value of 300 is applied, the number stays constant until it reaches almost to the end as shown in Fig. 76(e). The number drops at 160 sec, 800 sec, 1,320 sec, and 1,840 sec obtaining four cutting edg radius data points.

121
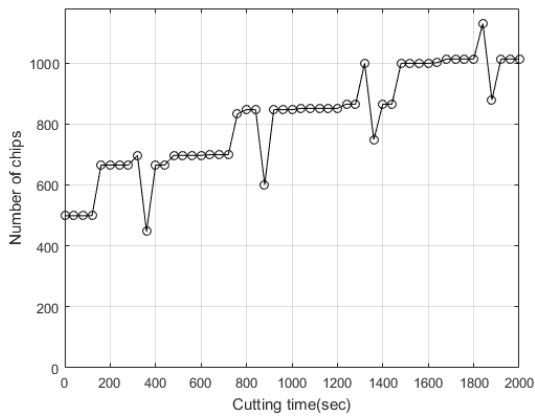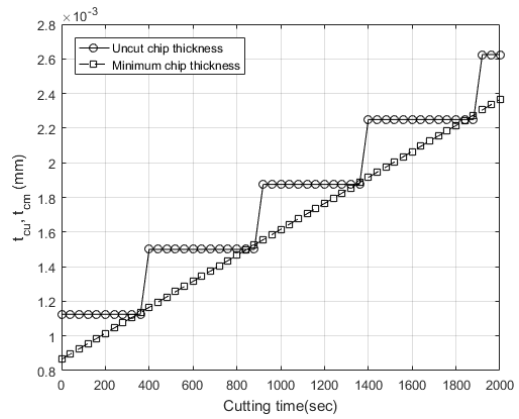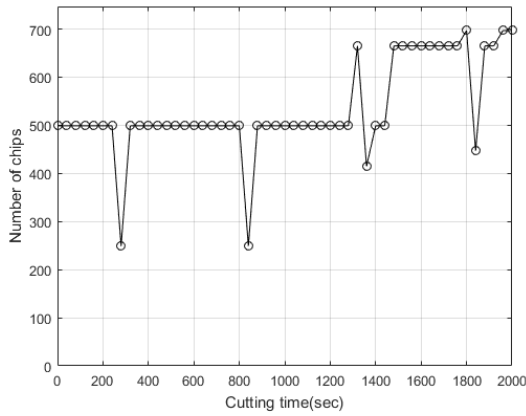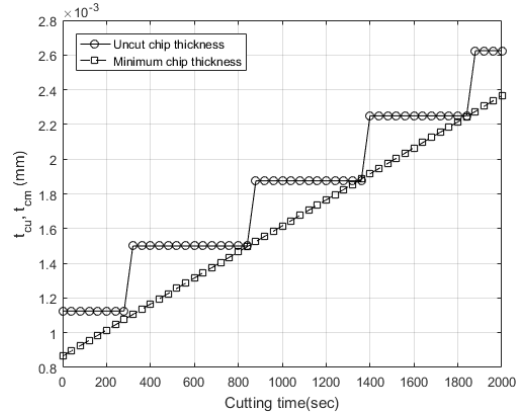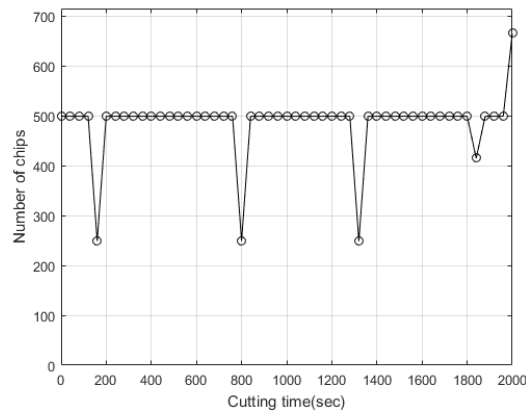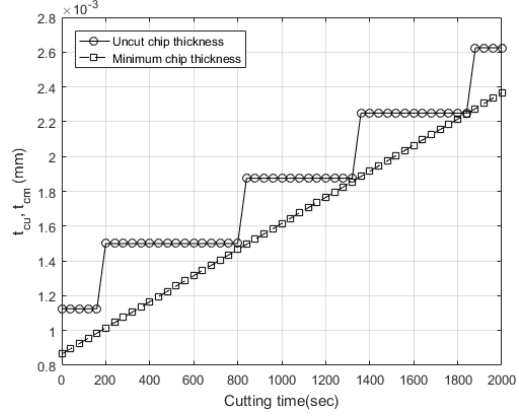
Figure 76. Linear cutting edge wear rate (a),(c),(e)number of chips vs. cutting time with the size filtering values of 50, 200, 300, respectively, (b),(d),(f) the UCT and the MCT vs. cutting time with the size filtering values of 50, 200, 300, respectively
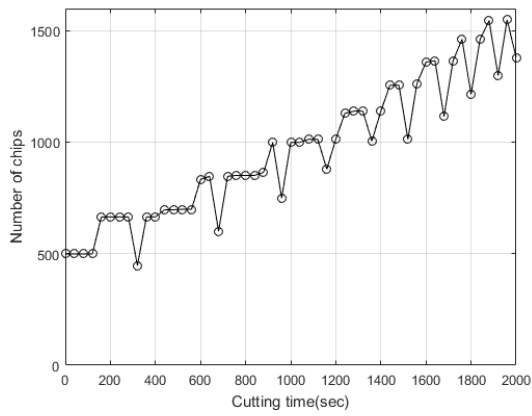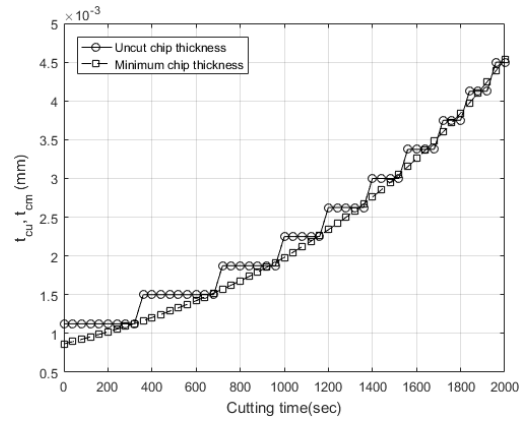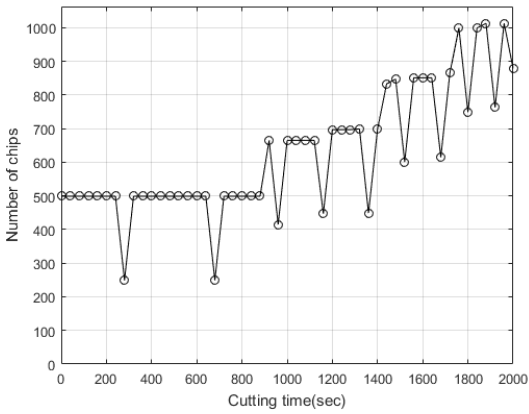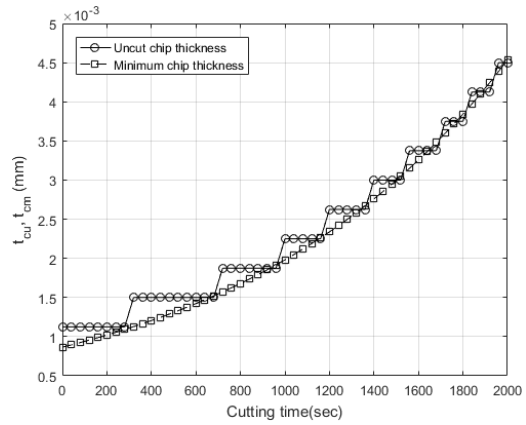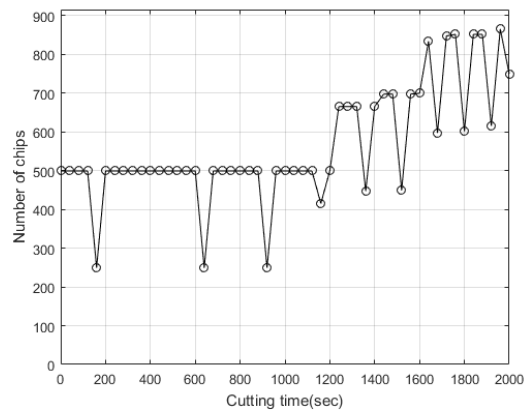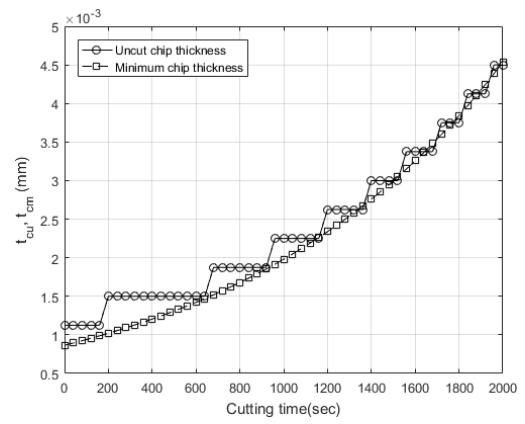
Figure 77. Exponential cutting edge wear rate (a),(c),(e)number of chips vs. cutting time with the size filtering values of 50, 200, 300, respectively, (b),(d),(f) the UCT and the MCT vs. cutting time with the size filtering values of 50, 200, 300, respectively.

From the exponential cutting edge wear model with 50 size filtering value, the number increases having nine drops as shown in Fig. 77(a). The size filtering values of 200 and 300 are applied as shown in Fig. 77(c)&(e). Those values are not large enough to make the number of chips constant. In the exponential model, the cuting edge wear rate becomes larger as the cutting time increases. And, the average volume of the chips increases as shown in Fig. 78.
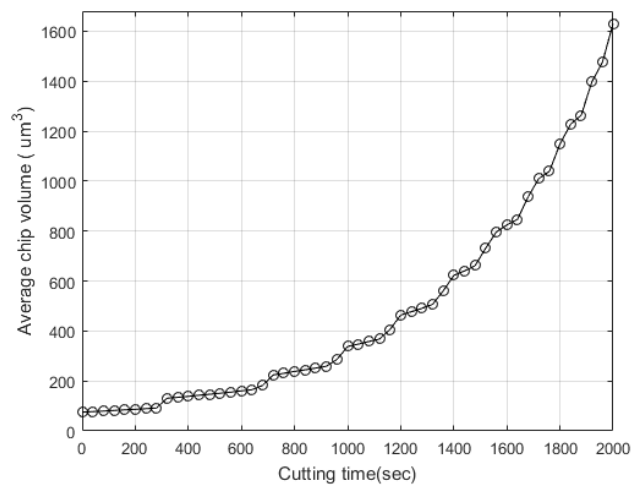
Figure 78. Change in the average volume of chips

Therefore, the size filtering value need to be increased based on the increase rate of average volume of the chips. The increase of the average volume of chips is fitted to an exponential function with the R-square of 99.47 % as Eq. (16).

$$v_{avg} = 63.45e^{0.001607t} \qquad\qquad (16)$$

The average volume increases due to not only the increase in the feedrate at the each drop of the chip number but also the increase of the cutting edge radius. As the

124

cutting edge radius becomes larger, the slip occurs more frequently which means that the chip thickness becomes thicker. Therefore, when the cutting edge wear rate increases much higher, then the influence of the ploughing effect should not be ignored.

If the increase of the average volume of the chips is considered in the determination of the size filtering value, the constant numbers of chips through out the whole cutting time can be obtained as shown in Fig. 79(a).

The error between the exponential cutting edge wear rate and the estimated cutting edge radius change rate by using the chip counting method is calculated. The average percentage error (%) is 10.44 % as shown in Fig. 79(c).

(a)

(b)

(c)
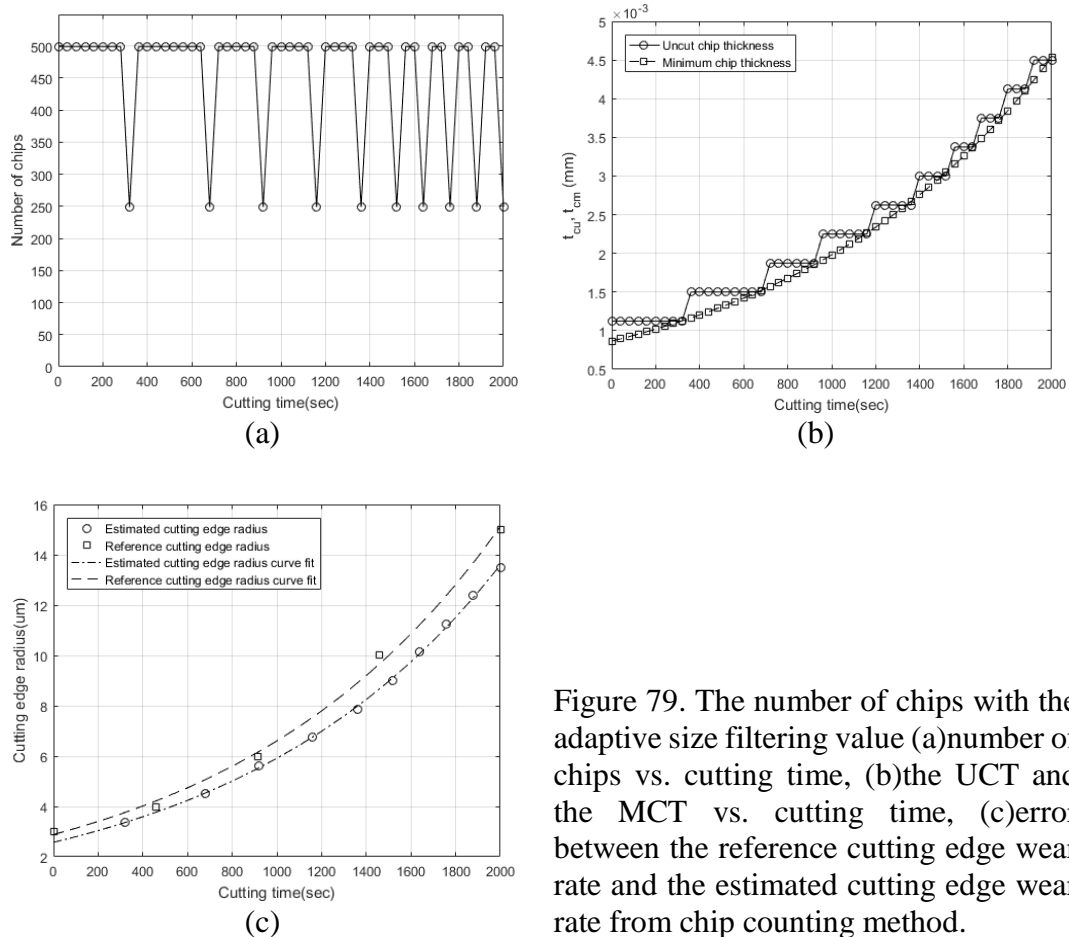
Figure 79. The number of chips with the adaptive size filtering value (a)number of chips vs. cutting time, (b)the UCT and the MCT vs. cutting time, (c)error between the reference cutting edge wear rate and the estimated cutting edge wear rate from chip counting method.

125

Section 5. Summary

The cutting edge wear estimation simulation is conducted by using the chip counting method based on the MCT effect. The simulation results show that the cutting edge wear rate can be estimated accurately with less than 11% of error compare to the reference data.

In the conventional tool wear monitoring methods, the cutting edge radius data can be obtained by taking the images of cutting edge using a microscope and by applying the image processing algorithm to draw a circle in order to measure the radius. But, these direct methods are not accurate and time consuming.

Our proposed method is expected to have the capability of collecting a large amount of cutting edge radius data during the cutting operation. Therefore, our method can be used to re-evaluate other direct tool wear monitoring methods by modeling the cutting edge wear rate with the cutting edge radius data points obtained from the online system.

However, the amount of the increase in the feedrate and the determination of the size filtering value need more investigation.

In the next chapter, the stability of micro-endmilling system is investigated by generating a chatter stability lobe using vision sensor.

CHAPTER 7

CHATTER STABILITY LOBE GENERATION FOR EXTENDED REACH MICRO-ENDMILLING USING VISION SENSOSR

This chapter presents a new chatter stability lobe generating method in micro-endmilling. The dynamic behavior of an extended reach 508 μm micro-endmill is recorded by a high-speed camera with a microscope lens. The stiffness, the natural frequency, and the damping ratio are measured in order to obtain a 2-DOF structural transfer function of the tool. In the stiffness measuring experiment, the step force input is applied to the tip of the tool and the displacement is measured from the CNC micro-milling machine. In the frequency response experiment, the impulse input is applied to the tool shank. The behavior of the area where the light being reflected on the tip of the tool is recorded while having the damped free vibration. The point tracking algorithm is applied to follow the vibrating tool to obtain the exponentially decaying frequency response. Based on the measurements, a chatter stability lobe is generated using the stiffness, natural frequency, and damping ratio obtained from the experiments.

Section 2. Background

The combination of the generation of wavy surface finish on the inner and outer surface of a chip due to the deflection of a flexible tool occured by the cutting force and the phase difference between the past tooth cut and the present tooth cut results in the regenerative UCT which causes self-excited vibration, chatter [141].
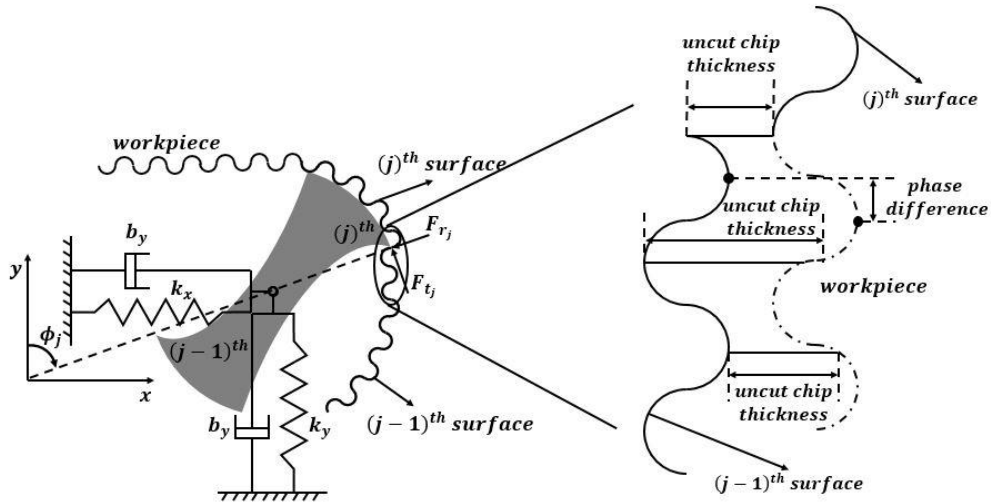
Figure 80. Regenerative chatter

The regenerative chatter mechanism is shown in Fig. 79. The prediction of chatter stability can be carried out by either numerical or analytical method. When the nonlinear behavior such as plouhing effect at the feed per tooth below the MCT in micro-milling is considered in the equation of motion, the solution needs to be solved numerically. However, in this research, only the linear cutting regime with the cutting feed per tooth above one third of the cutting edge radius [70, 142, 71, 126, 69] is considered. Therefore, the analytical stability model is applied in this work. The equation of motion of the micro-endmill is assumed to be a 2-DOF in the feed direction and the direction perpendicular to the feed. And the tool is assumed to be perfectly symmetric.

The development of the stability lobe in frequency domain is as follows[113]. The stability analysis begins with the varying UCT due to regenerative chatter described as Eq. (17) where $\Delta x(t) = x(t) - x(t-T)$ and $\Delta y(t) = y(t) - y(t-T)$ are the displacement in x and y direction and T is the tooth passing period.:

$$h(t) = \left(\Delta x(t) \cos \phi_j(t) + \Delta y(t) \cos \phi_j(t)\right) g\left(\phi_j(t)\right) \qquad (17)$$

The calculation takes place only within the engagement angle range via function $g(\phi_j)$ where $\phi_{st}(t)$ and $\phi_{ex}(t)$ are the start and exit engagement angle of the tooth.

$$g\left(\phi_j(t)\right) = \begin{cases} 1, & if\ \phi_{st}(t) < \phi_j(t) < \phi_{ex}(t) \\ 0, & otherwise \end{cases} \qquad (18)$$

The tangential cutting force on the jth tooth can be described as Eq.(19)&(20) where a is the axial depth of cut, K_t is the tangential cutting coefficient and K_r is the radial cutting coefficient.

$$F_{t_j}(t) = K_t a h_j(t) \qquad (19)$$

$$F_{r_j}(t) = K_r F_{t_j}(t) \qquad (20)$$

The total milling force direction can be obtained as Eq. (21) where a_{xx}, a_{xy}, a_{yx}, and a_{yy} are the directional milling force coefficients:

$$\begin{bmatrix} F_x \\ F_y \end{bmatrix} = \frac{1}{2} a K_t \begin{bmatrix} a_{xx} & a_{xy} \\ a_{yx} & a_{yy} \end{bmatrix} \begin{bmatrix} \Delta x \\ \Delta y \end{bmatrix} \qquad (21)$$

Fourier transformation is applied Eq. (21) to obtain the cutting force in the frequency domain. After the transformation, Fourier series expansion with zero order

is applied. The total milling force becomes Eq. (22) where a is the depth of cut, A_0 is the directional milling force coefficient and $G(i\omega)$ is the structural dynamic transfer function of the milling tool tip:

$$F(\omega) = \frac{1}{2} aK_t\left(1 - e^{-i\omega T}\right)A_0 G(i\omega)F(\omega) \qquad (22)$$

The structural dynamic transfer function of the milling tool tip is expressed as Eq. (23) where G_{xx} and G_{yy} are the dynamic transfer function in x and y direction:

$$G(i\omega) = \begin{bmatrix} G_{xx} & G_{xy} \\ G_{yx} & G_{yy} \end{bmatrix} \qquad (23)$$

Since the tool can be assumed as symmetric, the elements in Eq. (23) can be $G_{xx} = G_{yy}$ and $G_{xy} = G_{yx} = 0$.

The dynamic transfer function in the x direction can be described as Eq. (24) where X(s) is the displacement output in x direction, F(s) is the impulse input force, k is the stiffness of the tool tip, ω_n is the natural frequency and ζ is the damping ratio:

$$G_{xx}(s) = \frac{X(s)}{F(s)} = \frac{1}{k}\left(\frac{\omega_n^2}{s^2 + 2\zeta\omega_n s + \omega_n^2}\right) \qquad (24)$$

The characteristic equation of the system can be obtained from Eq. (22) as Eq. (25) where ω_c is chatter frequency:

130

$$det\left(I - \frac{1}{2}aK_t\left(1 - e^{-i\omega_c T}\right)A_0 G(i\omega_c)\right) = 0 \qquad (25)$$

The solution of Eq. (25) determines a_{lim} as

$$a_{lim} = -\frac{2\pi\Lambda_R}{NK_t}(1 + \kappa^2), \qquad \kappa = \frac{\Lambda_I}{\Lambda_R} \qquad (26)$$

where the real part and imaginery part are

$$\Lambda_R = Re\left(-\frac{1}{2a_0}\left(a_1 \pm \sqrt{a_1^2 - 4a_0}\right)\right)$$

$$\Lambda_I = Im\left(-\frac{1}{2a_0}\left(a_1 \pm \sqrt{a_1^2 - 4a_0}\right)\right)$$

where, $a_0 = G_{xx}(i\omega_c)G_{yy}(i\omega_c)(\alpha_{xx}\alpha_{yy} - \alpha_{xy}\alpha_{yx})$ and $a_1 = \alpha_{xx}G_{xx}(i\omega_c) + \alpha_{yy}G_{yy}(i\omega_c)$.

The spindle speed $n(rpm)$ can be calculated from Eq. (27) where $\epsilon = \pi - 2\psi$ is the phase difference and the phase shift can be calculated from $\psi = tan^{-1}\kappa$.

$$n = \frac{60}{NT}, \qquad T = \frac{\epsilon + 2k\pi}{\omega_c} \qquad (27)$$

Section 2. Experiment setup

Experimental setup is shown in Fig. 81. The structural dynamic transfer

function of the tool tip is needed in order to generate the stability lobe. The stiffness of the tool tip can be obtained from the static test by applying the step force input to the tool tip and the loadcell. The natural frequency and the damping ratio can be calculated from the free vibration frequency response test by appling the impulse force input. In the stiffness experiment a load cell (RB-Phi-117) with 780g capacity and 0.05% full scale precision is used to measure the applied force. The displacement for the stiffness experiment can be obtained by the position data from the machine.
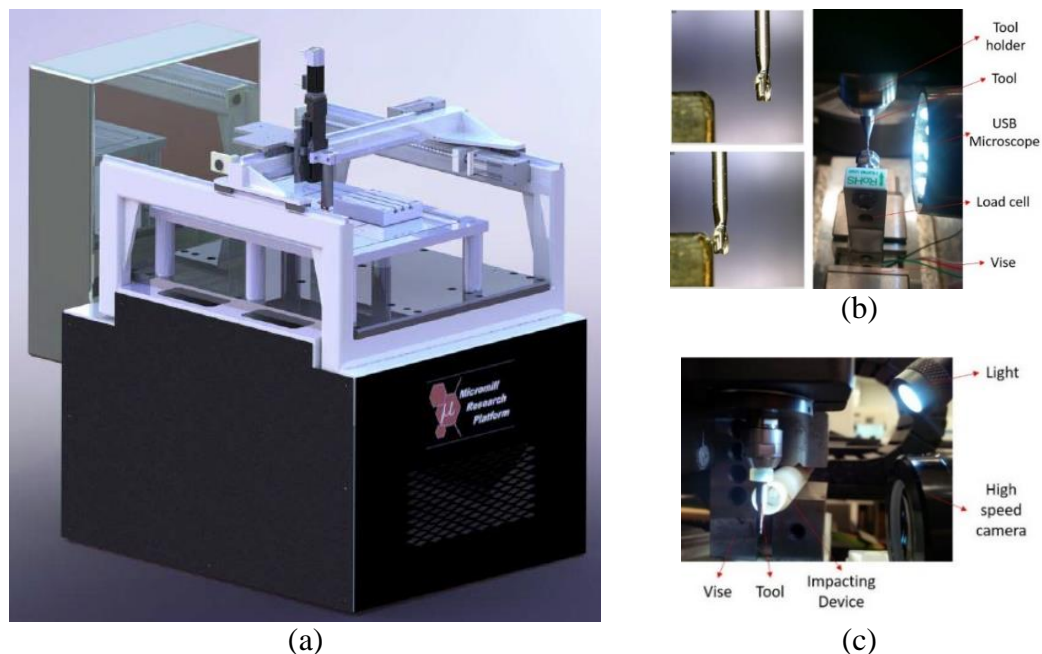
Figure 81. Stiffness and impulse response experiments set-up (a)milling machine, (b)stiffness measuring experiment, (c)frequency response experiment

An USB microscope (Dino-Lite AM4111T) is used to observe the tool during the stiffness experiment. And the displacement from the free vibration is measured using the high speed camera. A high speed camera (Chronos 1.4 high speed camera CR14-1.0) with a microscope lens (2x barlow lens) is used to record the video of the moving tool tip. The camera can perform from 1,057 FPS at 1280×1024 resolution to

38,565 FPS at 336×96 resolution. The FPS and the resolution are inversely proportional. In order to measure the high natural frequency, FPS must be fast. But the resolution is also important since the tool is small.

In this experiment, a 2-flute extended reach 508μm micro-endmill with 3.408 mm reach and the flute length of 0.762 mm from PMT(Performance Micro Tool : TS-2-0200-SR6) is selected to be able to assume the tool-tip as a uniform cantilever beam with circular cross-section. Only 1st mode natural frequency is considered since the 2nd mode natural frequency is not easy to generate and difficult to measure due to its high frequency. A 3-DOF CNC micro-milling machine with spindle (NSK NR-3080S) attached to a brushless motor (EM3080J) controlled by Beckhoff TwinCat 3.0 evironment is used for the cutting test. The spindle holder translates in x, y, and z direction instead of the spindle holder translating only in z direction and the workpiece translating in x and y direction as shown in Fig. 81(a). The full immersion slot milling is conducted on a brass 260 block in the selected cutting conditions with four different depth of cut at four different spindle speed based on the stability lobe to validate our experimental results by detecting the chatter frequency from the audio signal recorded by a microphone (Samson Go Mic) with 16-bit/44.1kHz resolution using Audacity software 2.2.2.

Section 3. Stiffness experiment

The stiffness of the tool tip can be obtained from two experiments: a static deformation experiment with a step force input applied to the tool-tip as shown in Fig. 82(a) and to the spindle-holder of the machine.
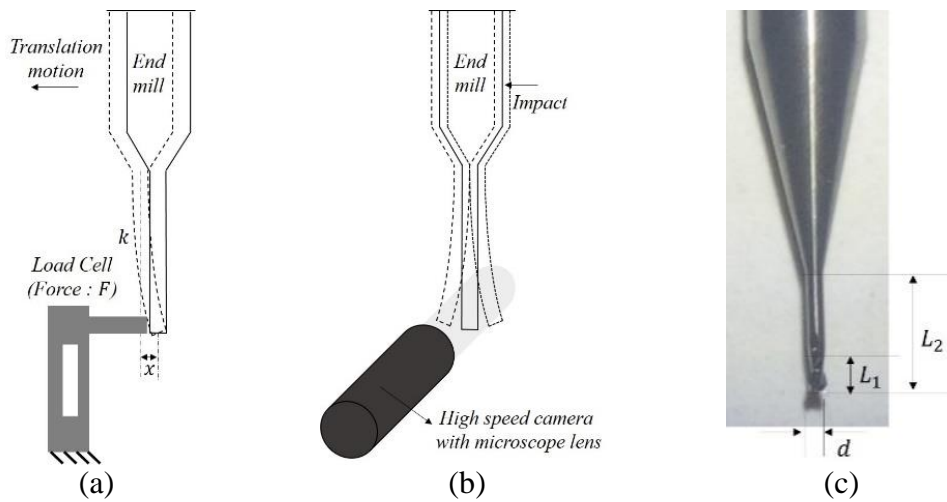
Figure 82. A schematic diagram of stiffness and impulse response experiments (a)stiffness measuring experiment, (b)frequency response experiment, (c)an extended reach $508 \mu m$ micro-endmill($L_1 = 0.762\ mm, L_2 = 3.048\ mm$)

In the experiment, the tool tip stopped before the applied force crosses the allowable maximum force with a safety factor 2 based on the maximum normal stress theory for the tungsten carbide tool as shown in Fig. 83. The maximum normal stress theory is applied. The tensile strength and the compression strength for the tungsten carbide are 344 MPa and 2.7 GPa, respectively.
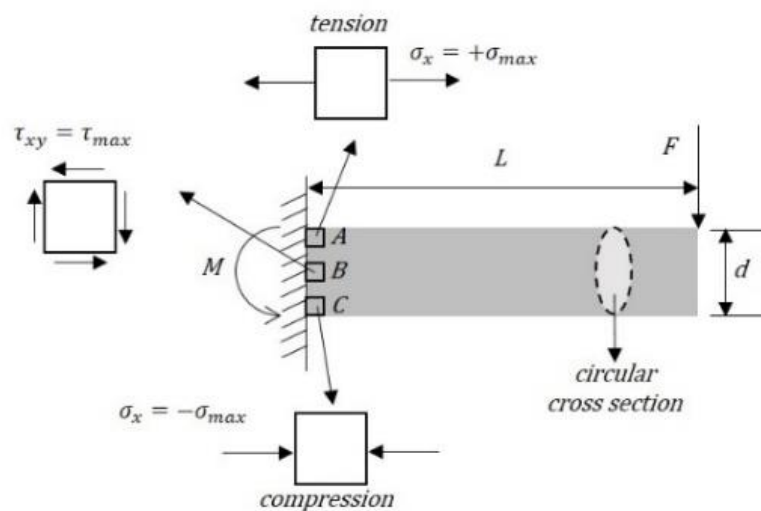
Figure 83. Maximum normal stress for tool tip

<table>
<tr><td>(a)</td><td>(b)</td><td>(c)</td></tr>
</table>
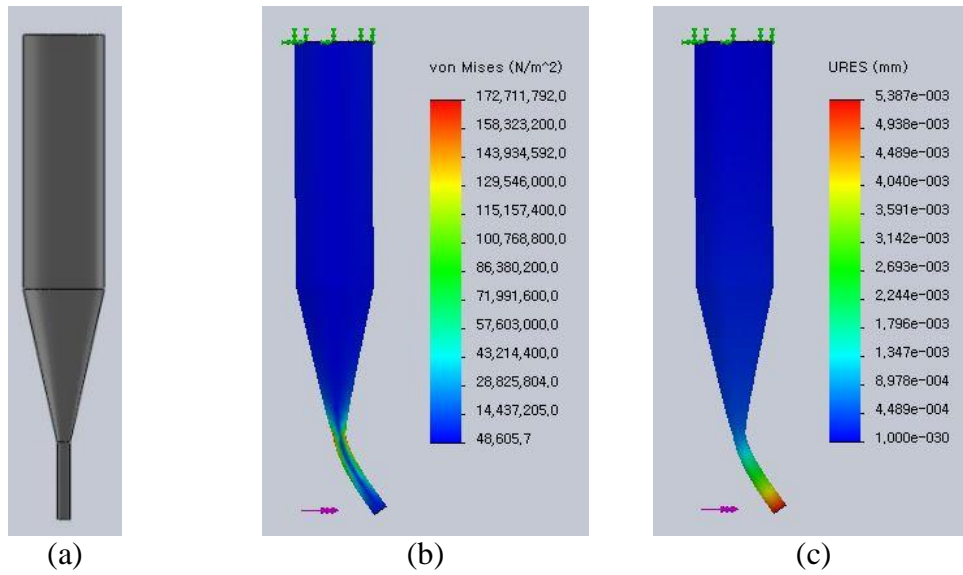
Figure 84. Stress and displacement analysis of tool tip(a)FEM model of the tool,(b) & (c) stress analysis and displacement of the tool in the static load of 0.72 N at the tip

Assuming that the tool tip can be regarded as a cantilever beam with a circular cross section, the maximum force can be obtained using the maximum and normal stresses as Eq. (28) where L is the length of the tool tip, d is the tool tip diameter, F is the applied force, $\sigma_{1,2}$ are the normal stresses, σ_x and σ_y is the normal stress in the x, y directions and τ_{xy} is the shear stress:

$$\sigma_{max} = \frac{4FL}{\pi \left(\frac{d}{2}\right)^3}, \qquad \tau_{max} = \frac{4F}{3\pi \left(\frac{d}{2}\right)^2}$$

$$\sigma_{1,2} = \frac{\sigma_x + \sigma_y}{2} \pm \sqrt{\left(\frac{\sigma_x - \sigma_y}{2}\right) + \tau_{xy}^2}$$

(28)

The maximum force allowed to the tool tip is 0.72 N based on the tool tip

135

geometry and the calculation of the maximum normal and shear stress at the different

locations A, B and C as shown in Fig. 83.

The stiffness of the tool tip with the overhang length of 10 mm is investigated

prior to the experiment by FEM simulation with Static Analysis in Solidworks

Simulation 2013 as shown in Fig. 84. The tool tip is modeled as a dummy rod. The

stiffness of the tool tip is predicted as 133.7 N/mm as shown in Fig. 84(c). And the

maximum stress of 172 MPa which is half of the yield stress due to the safety factor of

2 occurs at the location A.

In order to conduct the first experiment, an extended reach micro-endmill

installed on the spindle is translated until the tool tip makes contact with the load cell

to set the initial position. The tool tip is translated towards the loadcell to apply the

static force to the tool tip. The displacement is obtained from the position data displayed

on the milling machine and the force is measured by the load cell.

The stiffness measured from the first experiment (k_{ex1}) can be described as a

series connection of the stiffness of the translational joints(x&z direction or y&z

direction), the spindle, the loadcell, and the tool-tip ($k_{tool-tip}$). The total stiffness of all

the parts except the tool-tip is described as a stiffness of an assembly ($k_{assembly}$). The

relationship between these stiffness values is expressed as follows :

$$\frac{1}{k_{ex1}} = \frac{1}{k_{assembly}} + \frac{1}{k_{tool-tip}} \qquad (29)$$

In the second experiment, the spindle-holder is translated to the loadcell to

obtain the stiffness of the assembly except the tool-holder. The spindle-holder and the

spindle is assumed to be rigid. Therefore, the stiffness relationships can be expressed as following equation where k_{ex2} is the stiffness measured from the second experiment and $k_{tool-holder}$ is the stiffness of the spindle:

$$\frac{1}{k_{ex2}} = \frac{1}{k_{assembly}} - \frac{1}{k_{tool-holder}} \tag{30}$$

In the third experiment, the stiffness of the assembly is measured by translating the installed tool's shank to the loadcell. It can be expressed as Eq. (31) where k_{ex3} is the stiffness measured from the third experiment.

:

$$\frac{1}{k_{ex3}} = \frac{1}{k_{assembly}} \tag{31}$$

The stiffness of the tool-tip and the spindle can be calculated by substituting Eq. (31) into Eq. (30) and Eq. (29).

The stiffness values measured from the experiments are shown in Fig. 85. The stiffness values are linearized to a 1st order polynomial to simplify the calculation. The r-squared values from the curve fitting are above 98 % (Ex.1 : 99.5 %, Ex.2 : 98.6 %, Ex.3 : 98.1 %). The stiffness values show that if the applied force is less than 0.2 N, the nonlinearity increases with the incease of the r-squared values. Therefore, only the force data above 0.2 N is linearized.

137
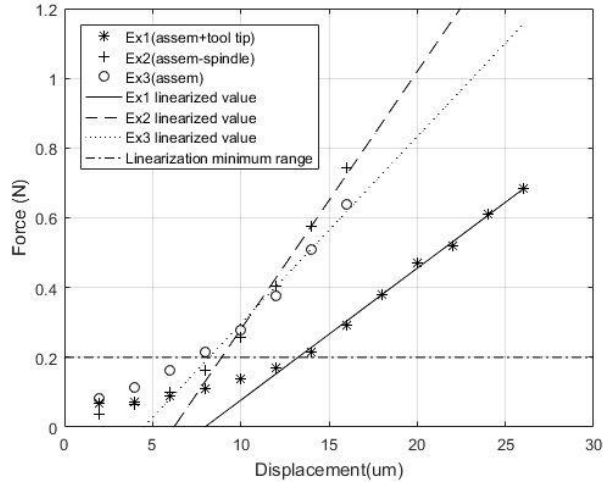
Figure 85. Stiffness experiment results

The stiffness values from the first, second and third experiment are 37.8 N/mm,
73.9 N/mm and 53.7 N/mm, respectively. The stiffness values for the tool tip and the
tool-holder are calculated as 128.1 N/mm and 195.7 N/mm. The stiffness of the tool-
tip from the experiment is 3.68 % different from the FEM result of 133 N/mm.

In our experiment, not all the parts in the assembly are taken into account. Since
the mass of the joint is extremely larger than the mass of the tool, the influence of the
dynamic behavior of the tool due to the periodic cutting force is not expected to reach
at the joint. Therefore, only the tool and the tool-holder is considered to develop a single
DOF mass-spring-damper system as shown in Fig. 86(a).

| (a) | (b) | (c) |
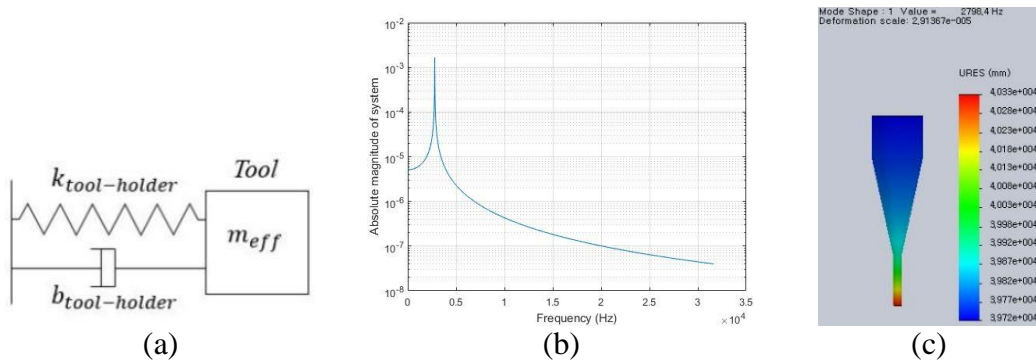
Figure 86. Frequency response experiment model(a)single DOF mass-spring-damper
model of the tool-holder, (b)FRF of the model, (c)FEM frequency analysis.

The stiffness is obtained from the stiffness experiment. The damping ratio and the 1st mode natural frequency are obtained from the impulse response experiment described in section 5. In the calculation, the effective mass of the tool should be used. For a single DOF mass-spring-damper system, the effective mass (m_{eff}) can be calculated as:

$$\omega_n = \sqrt{\frac{k}{m_{eff}}} \qquad (32)$$

The natural frequency and the damping ratio are obtained as 2787.4 Hz and 0.0342 from Section 6. The stiffness is measured as 195.7 N/mm. The effective mass is calculated as 0.6382 gram.

The FRF(Frequency Response Function) of this system is shown in Fig. 86(b). The effective mass is larger than the approximated mass of the tool tip of 0.01 grams but less than the approximated mass of the tool of 3.91 grams. From the FEM frequency analysis, the tool-tip, taper and the shank of the overhang length of 2.6 mm are included in the mass of 0.63 grams which has the 1st mode natural frequency of 2798.4 Hz.

The stiffness of the tool-holder in this experiment is much smaller than the stiffness values from the previous studies listed in Table 13. The stiffness values might vary from machine to machine, and thus a large variance can be seen.

However, most of the 1st mode natural frequency values exist between 2,000 and 4,000 Hz, which have less variance than the stiffness values. The natural frequency is influenced by the stiffness and the mass. But, the 1st mode natural frequency values in the table are the natural frequency of the assebled parts. It is different from the 1st

139

mode natural frequency of the tool which is about 15~16 kHz [120]. In order to understand the relationship between these values regarding this system, the mass of the assembled parts should be investigated. The stiffness might be proportional to the effective mass of the system since the natural frequency has much small variance. Therefore, the effective mass increases if the stiffness increases.

The stiffness and the damping ratio of the tool-holder, and the natural frequency are applied to generate the stability lobe in section 6.

Table 13
Stiffness, natural frequency, damping ratio of a tungsten carbide micro-endmill in the previous studies

Previous research	Dia. (μm)	1st mode natural freq. (Hz)	Stiffness (N/mm)	Damping ratio
[123]	500	4,035 (Tool-holder-spindle assembly)	3,200	0.0105
[121]	500	4,035 (Tool tip)	2,142.5	0.016
[124]	400	3,800 (Tool)	890	0.0362
[143]	500	3,722 (Tool tip)	80,100	0.009
[144]	500	2,189 (Tool tip)	-	0.012
[145]	500	710 (Tool tip)	3,200	0.007
[130]	500	3,633 (Tool tip)	586	0.075

Section 4. High speed camera and KLT point tracker

A high speed camera is used to measure the displacement of the tool tip in the frequency response experiment. From the recorded video frames, the displacement is measured by tracking the selected points on the tool tip using the Kanade-Lucas-Tomasi (KLT) point tracker algorithm from MATLAB R2016a.

In the frequency response experiment, the resolution and the frame rate are the main control parameters since the tool tip is small and it vibrates in the high frequency. Also, the light source significantly affects the performance of the point tracker algorithm. The light should be bright enough so that the reflected area can be clearly observed. The basic concept of KLT point tracker algorithm is to find the displacement vector between the two consecutive images I and J which minimizes the error described as Eq. (33) where t, τ and $x = (x, y)$ are the time variables and the space variables, respectively. And, $d = (\xi, \eta)$ is the displacement vector of the point x between time t and $t + \tau$ [146]:

$$J(x) = I(x, y, t + \tau)$$
$$I(x - d) = I(x - \xi, y - \eta, t)$$

$$(33)$$

The error between the images I and J can be obtained as :

$$J(x) = I(x - d) + \epsilon \qquad (34)$$

where, ϵ is the error described as Eq. (35) where W is a given window (selected area), and ω is a weighting function:

:

$$\epsilon = \int_W [I(x-d) - J(x)]^2 \omega dx \qquad (35)$$

In order to simplify the calculation of Eq. (35), $I(x-d)$ is linearized by Taylor series approximation assuming that the displacement is infinitesimal. Generally, the higher resolution results in the lower FPS. And, it increases the displacement in each frame and consequently reduces the performance of this algorithm due to the increased linearization error. Therefore, an available maximum FPS is recommended to obtain the highest performance.

The minimum eigenvalue algorithm is applied to the selected area on the tool tip where the light reflects. The points in the area of interest will be tracked well even after the impact as shown in Fig. 87 [147].

Section 5. Impulse response experiment

The 1st mode natural frequency and the damping ratio of the tool-holder-spindle assembly is measured by impacting the tool shank and the displacement of the tool tip is monitored by the high speed camera as shown in Fig. 87.

Based on the previous studies listed in Table 13, the 1st mode natural frequency for 400 µm and 500 µm tool-holder-spindle assembly is between 2,000 - 4,000 Hz. Therefore, the FPS of the high speed camera should be selected no less than 8,200 FPS in order to avoid the aliasing. In this experiment, the aliasing is minimized by choosing the highest FPS of 38,565 at 336×96 resolution.
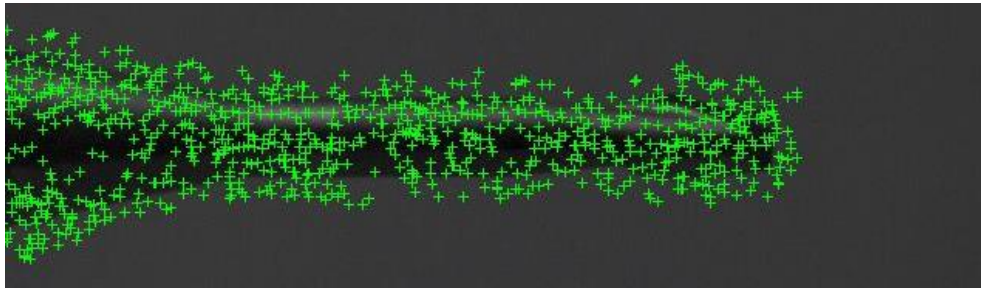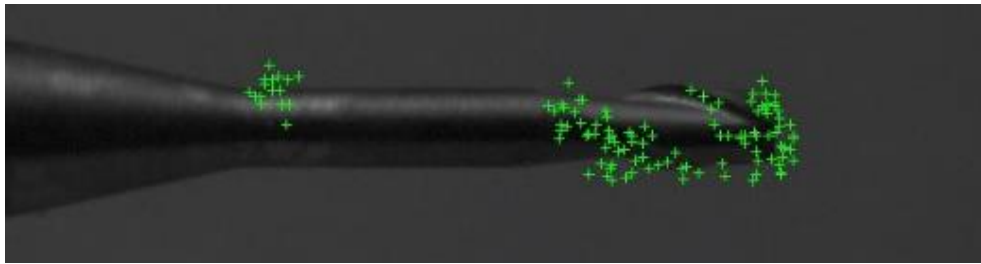
Figure 87. Point Selection by the minimum eigenvalue algorithm on 500 µm micro-endmill (a)original video frame with 640×360 high speed camera resolution, (b)video frame with selected points, (c)video frame after a small impact.

The points on the tool tip in the video are tracked by the point tracker to obtain the displacement. The damped natural frequency and the damping ratio can be calculated using the time preiod and the logarithmic decrement of two successive maximum values at time t_1 and t_2. The time period T and the damping ratio ζ can be obtained from Eq. (36) & (37) where y_1, y_2 are the successive maximum displacement values. And ω_d is the damped natural frequency:

$$t_2 - t_1 = T = \frac{2\pi}{\omega_d} \tag{36}$$

$$\zeta = \frac{\ln\left(\frac{y_1}{y_2}\right)/2\pi}{\sqrt{1 + \left(\ln\left(\frac{y_1}{y_2}\right)/2\pi\right)^2}} \tag{37}$$

The natural frequency ω_n can be calculated as :

$$\omega_n = \frac{\omega_d}{\sqrt{1 - \zeta^2}} \tag{38}$$

The displacement data is filtered by the high pass filter with the cutoff frequency 2,000 Hz to obtain only the 1st mode natrual frequency from the possible harmonic behavior of the tool. It is approximated by the exponential function with R-squared value of 97.2 %. The natural frequency of the tool-holder-spindle assembly and the damping ratio are 2,787.4 Hz and 0.0342, respectively as shown in Fig. 88(a) & (b).

In order to obtain the overhang length of the tool that agrees with the FEM simulation, the relationship between the natural frequency and the tool overhang length is investigated through the frequency response experiment with three different overhang length, 5 mm, 10 mm, and 15 mm. The natural frequency from the experiment differs only small amount compare to the simulation. Therefore, the overhang length of 10 mm is selected arbitrarily.
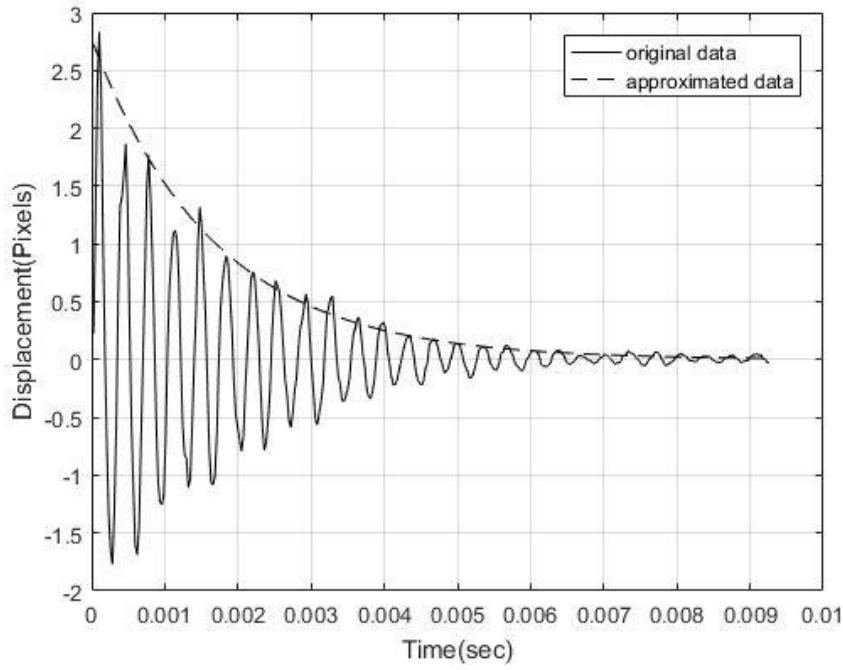
(a)

(b)

Figure 88. Impulse response experiment result(a)Displacement from the tool shank impact, (b)tracking the points on the tool (Camera resolution : 336×96, FPS : 38,565)

Table 14

Natural frequency in different overhang length of a 500 μm micro-endmill

Overhang length	Natural frequency (Hz)	
	Experiment	Simulation
5	2,787.4	3015.1
5	2,877.8	
10	2,730.8	2323.7
10	2,717.2	
15	2,737.4	1944.2
15	2,751.3	

Section 6. Chatter detection using microphone

Slot micro-endmilling is performed and a microphone is used to detect the chatter frequency in order to validate the stability lobe obtained from our proposed method.

The detection of chatter from the cutting test is conducted by collecting the audio signal using a microphone. And, the audio signal is analysed through the FFT (Fast Fourier Transform) plot to visulize the dominant frequencies. The microphone should be located more than 3 wavelengths away from the source to avoid the circulation of the sound wave in the near field. The distance farther than 3 wavelenghts is called the far field. If the microphone is in the far field, the sound source can be assumed as a point source which will not generate the sound circulation [148]. The wavelength of the chatter sound signal can be obtained from the 1st mode natural frequency of the micro-endmill. The chatter frequency of 508 µm tool is between 2,000-4,000 Hz. The wavelength λ can be calculated as Eq. (39) where, v is the speed of sound and f is the frequency:

$$\lambda = \frac{v}{f} \tag{39}$$

The speed of sound is 343 m/s at room temperature. The range of sound frequencies that are audible is 20 to 20 kHz. The chatter frequency is in the audible range and the wavelength is between 0.083-0.163 m. Therefore, the distance to the point where the far field starts is between 0.25-0.49 m. Since the chatter occurs around the natural frequency, the micrphone is located farther than 0.49 m to cover all possible

frequencies.
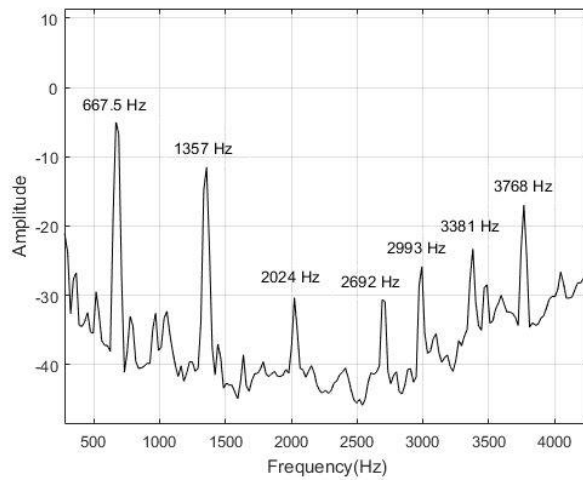
(a)
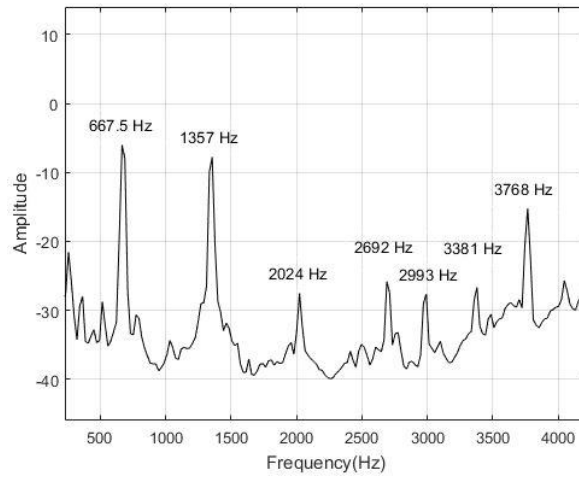
(b)
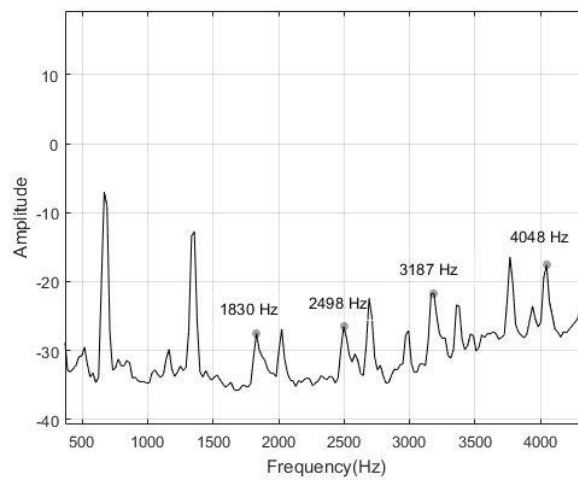
(c)

Figure 89. Chatter detection using microphone(a) FFT of the sound signal from the

microphone at 40,000 rpm idle, (b) 40,000 rpm with 50 µm depth of cut, (c) 40,000 rpm with 150 µm depth of cut

In order to test the microphone, the slot cutting tests are conducted using 1 mm end mill at 40,000 rpm with 8 mm/s feedrate. And the depth cuts are selected as 50 and 150 µm to compare the FFT of the sound signals from the stable and unstable cutting conditions. The multiples of the 667 Hz which is the spindle frequency with the background noise are shown in Fig. 89(a) at 40,000 rpm. In the stable condition with the depth of cut of 50 µm, the sound signal has almost same frequencies with the idle condition as shown in Fig. 89(b). In the unstable condition with the depth of cut of 150 µm, the sound signal has the frequecies generated from the chatter which are not the spindle frequencies or the back ground noise.

Section 7. Determinination of cutting force coefficient

In order to calculate the critical depth of cut and the spindle speed for the stability lobe, the cutting coefficients (K_t, K_r) are needed in Eq. (19) and (20). Those coefficients can only be obtained through the cutting experiments or slip-line field model or FEM cutting simulation. The coefficients are not influenced by the depth of cut, spindle speed, and feedrate, but by the workpiece material, UCT, and tool geometry such as the helix and the rake angle. But they are independent of the diameter of the tool [149].

In this experiment, the brass 260 is used as a workpiece and the tool has 30 deg. helix angle with 2~3µm cutting edge radius same as other research [150]. But the rake angle is not considered due to the unpredictable flank wear in micro-endmilling.

According to the other research, the cutting force coeffiencts can be described as Eq. (40) where h is the UCT, r is the cutting edge radius, and other parameters are

the constants from slip-line field model simulation shown listed in Table 15:

$$K_t(h,r) = \alpha_t h^{d_t} + \beta_t h^{p_t} r^{q_t}$$

$$K_r(h,r) = \alpha_r h^{d_r} + \beta_r h^{p_r} r^{q_r}$$

(40)

The constants from the slip-line field model are selected since it predicted the cutting force more accurate than the ones from the FEM simulation. The feed per tooth is set to 10 μm and the average UCT of 6.3662 μm is used to obtain the coefficients for the stability lobe [124]. And the cutting edge radius is selected as an average value of 2.5 μm assuming that the edge rounding and sharping may occur from the tool wear [151]. As a result, K_t is 917.19 MPa and K_r is 633.32 MPa.

Table 15
Constants for cutting force coefficients [150]

		α	d	β	p	q
Slip-line	K_t(MPa)	914.4	-0.0004	62.21	-0.814	0.230
	K_r(MPa)	629.4	-0.0002	78.24	-0.787	0.247

Section 8. Results

The feed per tooth for the cutting test should be selected larger then one third of the cutting edge radius to avoid the nonlinearity due to the ploughing effect. Also, the UCT has to be exist at all time within the start and exit engagement angle during the cutting test since regenerative chatter mechanism is based on the varying UCT.

The cutting edge radius of a 508 μm micro-endmill without any coating is approximately 2-3 μm from the previous research [25, 39, 40]. Therefore, the feed per tooth is set to be as 10 μm which is about 3 μm larger than the possible maximum run-out length to guarantee the shearing dominant cutting at all time.

The stiffness (195.7 N/mm), natural frequency (2787.4 Hz) and the damping (0.0342) of the tool-holder-spindle assembly obtained in the previous section are used to generate the stability lobe of the 2-DOF micro-endmilling system as shown in Fig. 90.
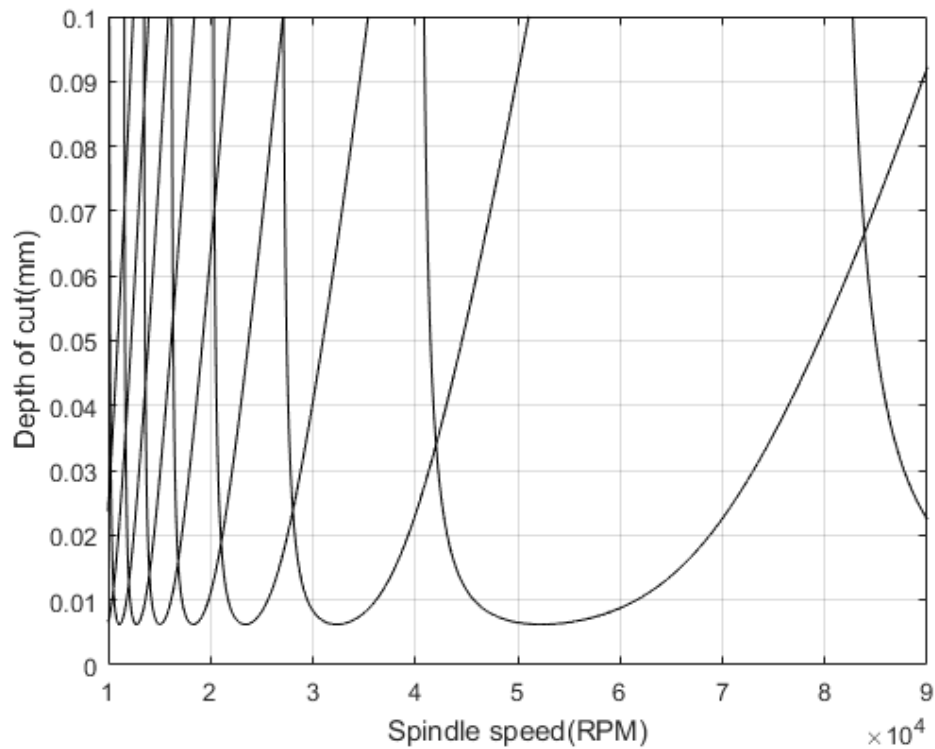
Figure 90. Stability lobe of tool-holder assembly of micro-endmilling system

Section 9. Summary

In order to avoid the chatter in micro-endmilling process, the chatter stability

150

lobe should be generated by investigating the structural dynamics of the machine system. In this chapter, the structural dynamics of a CNC machine is investigated by using a vision sensor and a load cell. The stiffness, natural frequency, and the damping ratio of the tool-holder assembly of the machine is obtained from the experiment. The chatter stability lobe is generated using those measurements.

In the future, the stability lobe should be validated through the microphone test with 500 μm micro-endmill.

CHAPTER 8

CONCLUSION AND FUTURE WORK

Section 1. Conclusion

This study introduces and evaluates a new method of tool wear estimation that can be performed online (without interrupting a cutting process) and is directly founded on the underlying physics of microscale chip formation. Unlike the conventional milling process, the tool wear has a major impact on micro-milling process due to the small size of the tool. Therefore, many studies have been conducted to develop the tool wear monitoring systems to investigate the tool wear. However, there are some disadvantages in the existing tool wear monitoring systems. To overcome these drawbacks, a new cutting edge wear estimator is developed in this research. Both the simulation and the experiment are conducted to evaluate the performance of the cutting edge wear estimator.

This study also investigates a new method of chatter modeling utilizing low-cost sensors (high-speed camera and loadcell) rather than the traditional instruments. When the cutting process is performed under unstable conditions, the regenerative chatter occurs. In unstable conditions, the cutting edge wear estimator cannot be used. Therefore, a stability lobe of the micro-endmmilling system is created by measuring the structural dynamic parameters of the system. To create a stability lobe, a transfer function of the system is needed. In order to create a transfer function, the stiffness, the natural frequency, and the damping ratio of the system are required. The conventional method of finding a transfer function was by analyzing the impulse response of the system from the impact applied to the system by an impact hammer. However, the price of the equipment needed for the conventional method is high. Therefore, the research

has been conducted to develop a new stability analysis method for micro-milling system. The following is a summary of the primary contributions of this work and the conclusions that have been drawn from the tool wear research and the chatter research.

1. A new method of modelling tool wear rate by measuring chip production rate in micromilling is introduced and analytically supported.

2. A chip production rate simulation for micromilling based on the MCT effect is developed and conducted.
    -   The simulation results show that the chip production rate decreases when the MCT becomes larger than the UCT.

Contribution and conclusions 1 and 2 have been published in:

J.-H. Lee and A. A. Sodemann, "Geometrical Simulation of Chip Production Rate in Micro-EndMilling," 46th SME North American Manufacturing Research Conference, NAMRC 46, Texas, USA, vol. 26, pp. 209–216, Jan. 2018.

3. An algorithm for measuring chip production rate from pictures of chips is developed and evaluated
    -   The chip counting algorithm using Locally Adaptive Threshold method can be applied to the image with less than 10 % of counting error.

Contribution and conclusions 3 have been published in:

J.-H. Lee and A. A. Sodemann, "Digital Image Processing for Counting Chips in Micro-End-Milling," in Proceedings of the 2nd International Conference on Vision, Image and Signal Processing   - ICVISP 2018, Las Vegas, NV, USA, 2018, pp. 1–6.

4. A machine for collecting chips and measuring the chip production rate is designed, built, and evaluated.

    -   The number of chips measured from the machine has less than 5% of covariance.

5. A complete set of experiments for relating the chip production rate to the cutting-edge radius is designed and performed.

    -   The experimental results are used to validate the chip-production-rate experiments.

    -   The experimental results show that detection of the transition zone could be possible by detecting the decrease in the chip product rate.

Contribution and conclusions 4 and 5 has been published in:

J.-H. Lee, A. A. Sodemann, and A. K. Bajaj, "Experimental Validation of Chip Production Rate as a Tool Wear Identification in Micro-EndMilling," International Journal of Advanced Manufacturing Technology

6. An evaluation of the reliability of the cutting edge wear estimator is conducted.

    -   The evaluation results show that the probability of correct estimation of the cutting edge radius is more than 80%.

Contribution and conclusions 6 has been published in:

J.-H. Lee and A. A. Sodemann, "Reliability of cutting edge radius estimator based on chip production rate for micro-endmilling," Journal of Manufacturing and Materials Processing.

7. A cutting edge wear rate model simulation based upon the chip production rate relationship is created and evaluated against an existing tool wear model.

- The simulation results show that the cutting edge wear estimator is applicable to the online system.

Contribution and conclusions 7 has been accepted to:

[Accepted]J.-H. Lee and A. A. Sodemann, "Simulation of Cutting Edge Wear Model based on Chip Production Rate in Micro-endmilling," Proceedings of the ASME 2019 14th International Manufacturing Science and Engineering Conference(MSEC2019). Erie, PA, USA

8. A new method of measuring the structural dynamic parameters is proposed and the experiments have been performed.

- A loadcell is used to measure the stiffness of the tool-holder assembly of the CNC machine. Then, a high speed camera with a microscope lens is used to measure the natural frequency and the damping ratio of the tool-holder assembly.
- The stability lobe of the system is created based on the measured dynamic parameters.
- This new method is more cost-effective than conventional methods.

9. The chatter detection experiment is performed using a microphone.

- The chatter frequency of the system is detected by analyzing the sound signal recorded using a microphone during the cutting process with a 1-mm endmill.

Section 2. Future work

The following points should be improved in the future.

① Future research is needed to reduce the difference between the number of chips expected from the calculation and the actual number of chips measured in the experiment.

- The chip collecting part has the pneumatic system. The pneumatic part uses the material conveying air pump to collect the chips through two suction nozzles. Two nozzles suck the chips from the left and right side of the tool. However, these nozzles are not able to suck all the chips. Therefore, a new suction nozzle that could suck more chips should be developed in the future.

- The chip collecting part has the adhesive tape part. The chips will be blown and attached on the tape. However, some chips can fly away through the gap between the exhaust of the air pump and the tape. Therefore, a new research should be conducted to make the chips stick on the tape as many as possible.

- The chip counting part is consisted of the image taking part and the image processing part. In the image taking part, the focus of the USB microscope should be fixed. However, the focus changes due to the flexible tape. If the focus changes, the size of the chips from the image can change. Therefore, the size filtering value could become an uncontrollable variable. Hence, further research is needed to fix the focus.

② The cutting edge wear estimator should be applied to an online system.

- In order to apply the cutting edge wear estimator to an online system, furthur study is needed to make the tape stop perfectly. When the USB microscope is taking images of the tape, the tape should be stopped. But, the tape moves even after the tape collecting motor stopped due to the flexibility of the tape. Therefore, more studies on the tape are needed to understand the behavior of the tape.

③ The resolution of the cutting edge wear estimator should be increased.
- In this research, the resolution of the cutting edge wear estimator is set to be 1mm/s. However, the resolution should be increased to improve the accuracy of the estimator.

④ The chatter detection test using a micro-endmill is needed.
- In this research, the chatter detection test is conducted using a 1 mm endmill. The chatter detection test is not conducted using a micro-endmill. The chatter experiment will be performed in the future.

⑤ The stiffness of the endmilling machine should be investigated in depth.
- The stiffness of the tool-holder assembly is measured using a loadcell in this research. However, the stiffness of the other parts of the machine such as the joints should be investigated to reduce the error.

REFERENCES

1. Alting L, Kimura F, Hansen HN, Bissacco G (2003) Micro Engineering. CIRP Annals 52:635–657. https://doi.org/10.1016/S0007-8506(07)60208-X

2. (2017) Future Market Insights: Global Microfluidics Sales to Exceed $11 Billion by 2026 End. Health & Beauty Close - Up; Jacksonville

3. Dhanorker A, Ozel T (2008) Meso/micro scale milling for micro-manufacturing. International Journal of Mechatronics and Manufacturing Systems 1:23–42

4. Chae J, Park SS, Freiheit T (2006) Investigation of micro-cutting operations. International Journal of Machine Tools and Manufacture 46:313–332

5. Liu X, DeVor RE, Kapoor SG, Ehmann KF (2004) The Mechanics of Machining at the Microscale: Assessment of the Current State of the Science. Journal of Manufacturing Science and Engineering 126:666. https://doi.org/10.1115/1.1813469

6. Chae J, Park SS, Freiheit T (2006) Investigation of micro-cutting operations. International Journal of Machine Tools and Manufacture 46:313–332. https://doi.org/10.1016/j.ijmachtools.2005.05.015

7. Kurada S, Bradley C (1997) A review of machine vision sensors for tool condition monitoring. Computers in Industry 34:55–72. https://doi.org/10.1016/S0166-3615(96)00075-9

8. Malekian M, Park SS, Jun MB (2009) Tool wear monitoring of micro-milling operations. Journal of Materials Processing Technology 209:4903–4914

9. Thepsonthi T, Özel T (2015) 3-D finite element process simulation of micro-end milling Ti-6Al-4V titanium alloy: experimental validations on chip flow and tool wear. Journal of Materials Processing Technology 221:128–145

10. Tansel I, Trujillo M, Nedbouyan A, et al (1998) Micro-end-milling—III. Wear estimation and tool breakage detection using acoustic emission signals. International Journal of Machine Tools and Manufacture 38:1449–1466

11. Zhu K, Yu X (2017) The monitoring of micro milling tool wear conditions by wear area estimation. Mechanical Systems and Signal Processing 93:80–91

12. Aramcharoen A, Mativenga PT (2009) Size effect and tool geometry in micromilling of tool steel. Precision Engineering 33:402–407. https://doi.org/10.1016/j.precisioneng.2008.11.002

13. Wang J, Gong Y, Abba G, et al (2009) Chip formation analysis in micromilling operation. The International Journal of Advanced Manufacturing Technology 45:430–447. https://doi.org/10.1007/s00170-009-1989-8

14. Ikawa N, Shimada S, Tanaka H (1992) Minimum thickness of cut in micromachining. Nanotechnology 3:6. https://doi.org/10.1088/0957-4484/3/1/002

15. Kim C-J, Mayor JR, Ni J (2005) A Static Model of Chip Formation in Microscale Milling. J Manuf Sci Eng 126:710–718. https://doi.org/10.1115/1.1813475

16. Davies MA, Chou Y, Evans CJ (1996) On Chip Morphology, Tool Wear and Cutting Mechanics in Finish Hard Turning. CIRP Annals - Manufacturing Technology 45:77–82. https://doi.org/10.1016/S0007-8506(07)63020-0

17. Yuan ZJ, Zhou M, Dong S (1996) Effect of diamond tool sharpness on minimum cutting thickness and cutting surface integrity in ultraprecision machining. Journal of Materials Processing Technology 62:327–330. https://doi.org/10.1016/S0924-0136(96)02429-6

18. Lee J-H, Sodemann AA (2018) Geometrical Simulation of Chip Production Rate in Micro-EndMilling. Procedia Manufacturing 26:209–216. https://doi.org/10.1016/j.promfg.2018.07.029

19. Elbestawi MA, Papazafiriou TA, Du RX (1991) In-process monitoring of tool wear in milling using cutting force signature. International Journal of Machine Tools and Manufacture 31:55–73. https://doi.org/10.1016/0890-6955(91)90051-4

20. Sarhan A, Sayed R, Nassr A., El-Zahry R. (2001) Interrelationships between cutting force variation and tool wear in end-milling. Journal of Materials Processing Technology 109:229–235. https://doi.org/10.1016/S0924-0136(00)00803-7

21. Alhadeff LL, Marshall MB, Curtis DT, Slatter T (2019) Protocol for tool wear measurement in micro-milling. Wear 420–421:54–67. https://doi.org/10.1016/j.wear.2018.11.018

22. Kerr D, Pengilley J, Garwood R (2006) Assessment and visualisation of machine tool wear using computer vision. The International Journal of Advanced Manufacturing Technology 28:781–791. https://doi.org/10.1007/s00170-004-2420-0

23. Hou Y, Zhang D, Wu B, Luo M (2015) Milling Force Modeling of Worn Tool and Tool Flank Wear Recognition in End Milling. IEEE/ASME Transactions on Mechatronics 20:1024–1035. https://doi.org/10.1109/TMECH.2014.2363166

24. Ai C, Sun Y, He G, et al (2012) The milling tool wear monitoring using the acoustic spectrum. International Journal of Advanced Manufacturing Technology 61:457–463. https://doi.org/10.1007/s00170-011-3738-z

25. Zhu K, San Wong Y, Hong GS (2009) Multi-category micro-milling tool wear monitoring with continuous hidden Markov models. Mechanical Systems and

Signal Processing 23:547–560

26. Lu X, Wang F, Jia Z, Liang SY (2018) The flank wear prediction in micro-milling Inconel 718. Ind Lubrication and Tribology 70:1374–1380. https://doi.org/10.1108/ILT-01-2018-0031

27. Jawahir IS, Van Luttervelt CA (1993) Recent developments in chip control research and applications. CIRP Annals-Manufacturing Technology 42:659–693

28. Devillez A, Lesko S, Mozer W (2004) Cutting tool crater wear measurement with white light interferometry. Wear 256:56–65. https://doi.org/10.1016/S0043-1648(03)00384-3

29. Melo ACA de, Milan JCG, Silva MB da, Machado ÁR (2006) Some observations on wear and damages in cemented carbide tools. Journal of the Brazilian Society of Mechanical Sciences and Engineering 28:269–277. https://doi.org/10.1590/S1678-58782006000300004

30. Enahoro HE, Oxley PLB (1966) Flow along Tool-Chip Interface in Orthogonal Metal Cutting. Journal of Mechanical Engineering Science 8:36–41. https://doi.org/10.1243/JMES_JOUR_1966_008_007_02

31. Malekian M, Mostofa MG, Park SS, Jun MBG (2012) Modeling of minimum uncut chip thickness in micro machining of aluminum. Journal of Materials Processing Technology 212:553–559

32. Thepsonthi T, Özel T (2013) Experimental and finite element simulation based investigations on micro-milling Ti-6Al-4V titanium alloy: Effects of cBN coating on tool wear. Journal of Materials Processing Technology 213:532–542. https://doi.org/10.1016/j.jmatprotec.2012.11.003

33. Ucun İ, Aslantas K, Bedir F (2013) An experimental investigation of the effect of coating material on tool wear in micro milling of Inconel 718 super alloy. Wear 300:8–19. https://doi.org/10.1016/j.wear.2013.01.103

34. Zhou L, Peng FY, Yan R, et al (2015) Analytical modeling and experimental validation of micro end-milling cutting forces considering edge radius and material strengthening effects. International Journal of Machine Tools and Manufacture 97:29–41. https://doi.org/10.1016/j.ijmachtools.2015.07.001

35. Tan G, Liu G, Li G (2009) Experimental study on adhesive wear of milling insert with complex groove. The International Journal of Advanced Manufacturing Technology 44:631–637. https://doi.org/10.1007/s00170-008-1856-z

36. Chuangwen X, Jianming D, Yuzhen C, et al (2018) The relationships between cutting parameters, tool wear, cutting force and vibration. Advances in Mechanical Engineering 10:1687814017750434. https://doi.org/10.1177/1687814017750434

37.   Li B (2012) A review of tool wear estimation using theoretical analysis and numerical simulation technologies. International Journal of Refractory Metals and Hard Materials 35:143–151. https://doi.org/10.1016/j.ijrmhm.2012.05.006

38.   Taylor FW (1906) On the Art of Cutting Metals... American society of mechanical engineers

39.   Shaw MC, Dirke SO (1956) On the wear of cutting tools. Microtechnic 10:187–193

40.   Taylor J (1962) The tool wear-time relationship in metal cutting. International Journal of Machine Tool Design and Research 2:119–152. https://doi.org/10.1016/0020-7357(62)90002-1

41.   Usui E, Shirakashi T, Kitagawa T (1984) Analytical prediction of cutting tool wear. Wear 100:129–151. https://doi.org/10.1016/0043-1648(84)90010-3

42.   Usui E, Shirakashi T, Kitagawa T (1984) Analytical prediction of cutting tool wear. Wear 100:129–151. https://doi.org/10.1016/0043-1648(84)90010-3

43.   Bhattacharyya A, Ham I (1969) Analysis of tool wear—part I: theoretical models of flank wear. Journal of Engineering for Industry 91:790–796

44.   Takeyama H, Murata R (1963) Basic Investigation of Tool Wear. J Eng Ind 85:33–37. https://doi.org/10.1115/1.3667575

45.   Kannatey-Asibu E (1985) A transport-diffusion equation in metal cutting and its application to analysis of the rate of flank wear. Journal of engineering for industry 107:81–89

46.   Jun MB, Devor RE, Kapoor SG, Englert F (2008) Experimental investigation of machinability and tool wear in micro-endmilling. In: Transactions of the North American Manufacturing Research Institution of SME

47.   Bao WY, Tansel IN (2000) Modeling micro-end-milling operations. Part III: influence of tool wear. International Journal of Machine Tools and Manufacture 40:2193–2211. https://doi.org/10.1016/S0890-6955(00)00056-0

48.   Keiji O, Katsundo H (1963) Flank Wear Progress and Variation of Tool Forces. Journal of the Japan Society of Precision Engineering 29:304–309. https://doi.org/10.2493/jjspe1933.29.304

49.   Iwata K (1977) An application of acoustic emission measurement to in-process sensing of tool wear. Annals of the CIRP 25:21–26

50.   Rao SB (1986) Tool wear monitoring through the dynamics of stable turning. J Eng Ind(Trans ASME) 108:183–190

51.   Diei EN, Dornfeld DA (1987) Acoustic Emission Sensing of Tool Wear in Face Milling. Journal of Engineering for Industry 109:234.

https://doi.org/10.1115/1.3187124

52. Jeon JU, Kim SW (1988) Optical flank wear monitoring of cutting tools by image processing. Wear 127:207–217

53. Rangwala S, Dornfeld D (1990) Sensor Integration Using Neural Networks for Intelligent Tool Condition Monitoring. J Eng Ind 112:219–228. https://doi.org/10.1115/1.2899578

54. Purushothaman S, Srinivasa YG (1994) A back-propagation algorithm applied to tool wear monitoring. International Journal of Machine Tools and Manufacture 34:625–631

55. Lim GH (1995) Tool-wear monitoring in machine turning. Journal of materials processing technology 51:25–36

56. Lin SC, Lin RJ (1996) Tool wear monitoring in face milling using force signals. Wear 198:136–142. https://doi.org/10.1016/0043-1648(96)06944-X

57. Xiaoli L, Zhejun Y (1998) Tool wear monitoring with wavelet packet transform—fuzzy clustering method. Wear 219:145–154

58. Li X, Djordjevich A, Venuvinod PK (2000) Current-sensor-based feed cutting force intelligent estimation and tool wear condition monitoring. IEEE Transactions on Industrial Electronics 47:697–702

59. Ertunc HM, Loparo KA, Ocak H (2001) Tool wear condition monitoring in drilling operations using hidden Markov models (HMMs). International Journal of Machine Tools and Manufacture 41:1363–1384

60. Moriwaki T, Shibasaka T, Tangjitsitcharoen S (2004) Development of in-Process Tool Wear Monitoring System for CNC Turning. JSME International Journal Series C Mechanical Systems, Machine Elements and Manufacturing 47:933–938. https://doi.org/10.1299/jsmec.47.933

61. Tansel I, Rodriguez O, Trujillo M, et al (1998) Micro-end-milling—I. Wear and breakage. International Journal of Machine Tools and Manufacture 38:1419–1436. https://doi.org/10.1016/S0890-6955(98)00015-7

62. Tansel IN, Bao WY, Reen NS, Kropas-Hughes CV (2005) Genetic tool monitor (GTM) for micro-end-milling operations. International Journal of Machine Tools and Manufacture 45:293–299. https://doi.org/10.1016/j.ijmachtools.2004.08.013

63. Jemielniak K, Arrazola PJ (2008) Application of AE and cutting force signals in tool condition monitoring in micro-milling. CIRP Journal of Manufacturing Science and Technology 1:97–102

64. Hsieh W-H, Lu M-C, Chiou S-J (2012) Application of backpropagation neural network for spindle vibration-based tool wear monitoring in micro-milling. The

International Journal of Advanced Manufacturing Technology 61:53–61

65. Ren Q, Balazinski M, Baron L, et al (2014) Type-2 fuzzy tool condition monitoring system based on acoustic emission in micromilling. Information Sciences 255:121–134

66. Zhu K, Mei T, Ye D (2015) Online Condition Monitoring in Micromilling: A Force Waveform Shape Analysis Approach. IEEE Transactions on Industrial Electronics 62:3806–3813. https://doi.org/10.1109/TIE.2015.2392713

67. Filiz S, Conley CM, Wasserman MB, Ozdoganlar OB (2007) An experimental investigation of micro-machinability of copper 101 using tungsten carbide micro-endmills. International Journal of Machine Tools and Manufacture 47:1088–1100. https://doi.org/10.1016/j.ijmachtools.2006.09.024

68. Liu X, DeVor RE, Kapoor SG (2006) An analytical model for the prediction of minimum chip thickness in micromachining. Journal of manufacturing science and engineering 128:474–481

69. Mian AJ, Driver N, Mativenga PT (2011) Estimation of minimum chip thickness in micro-milling using acoustic emission. Proceedings of the Institution of Mechanical Engineers, Part B: Journal of Engineering Manufacture 225:1535–1551

70. L'vov NP (1969) Determining the minimum possible chip thickness. Machines & Tooling 4:45

71. Vogler MP (2003) On the Modeling and Analysis of Machining Performance in Microendmilling. University of Illinois at Urbana-Champaign

72. Wyen C-F, Wegener K (2010) Influence of cutting edge radius on cutting forces in machining titanium. CIRP Annals-Manufacturing Technology 59:93–96

73. Piispanen V (1948) Theory of Formation of Metal Chips. Journal of Applied Physics 19:876–881. https://doi.org/10.1063/1.1697893

74. Piispanen V (1937) Theory of chip formation. Teknillinen Aikaauslenti 27:315–322

75. Merchant ME (1945) Mechanics of the Metal Cutting Process. I. Orthogonal Cutting and a Type 2 Chip. Journal of Applied Physics 16:267–275. https://doi.org/10.1063/1.1707586

76. Connolly R, Rubenstein C (1968) The mechanics of continuous chip formation in orthogonal cutting. International journal of machine tool design and research 8:159–187

77. Ramalingam S, Bell AC (1973) A Scanning Electron Microscope Stage for the Observation of Chip Formation. Review of Scientific Instruments 44:573–576. https://doi.org/10.1063/1.1686185

78. Doyle ED, Horne JG, Tabor D (1979) Frictional interactions between chip and rake face in continuous chip formation. Proc R Soc Lond A 366:173–183

79. Hastings WF, Mathew P, Oxley PLB (1980) A Machining Theory for Predicting Chip Geometry, Cutting Forces etc. From Work Material Properties and Cutting Conditions. Proceedings of the Royal Society of London Series A, Mathematical and Physical Sciences 371:569–587

80. Komanduri R, Brown RH (1981) On the Mechanics of Chip Segmentation In Machining. J Eng Ind 103:33–51. https://doi.org/10.1115/1.3184458

81. Lee D (1984) The Nature of Chip Formation in Orthogonal Machining. J Eng Mater Technol 106:9–15. https://doi.org/10.1115/1.3225683

82. Tay AO, Stevenson MG, De Vahl Davis G (1974) Using the Finite Element Method to Determine Temperature Distributions in Orthogonal Machining. Proceedings of the Institution of Mechanical Engineers 188:627–638. https://doi.org/10.1243/PIME_PROC_1974_188_074_02

83. Strenkowski JS, Carroll I JT (1985) A Finite Element Model of Orthogonal Metal Cutting. J Eng Ind 107:349–354. https://doi.org/10.1115/1.3186008

84. Strenkowski JS, Moon K-J (1990) Finite Element Prediction of Chip Geometry and Tool/Workpiece Temperature Distributions in Orthogonal Metal Cutting. J Eng Ind 112:313–318. https://doi.org/10.1115/1.2899593

85. Ceretti E, Fallböhmer P, Wu WT, Altan T (1996) Application of 2D FEM to chip formation in orthogonal cutting. Journal of Materials Processing Technology 59:169–180. https://doi.org/10.1016/0924-0136(96)02296-0

86. Kim C-J, Bono M, Ni J (2002) Experimental analysis of chip formation in micro-milling. TECHNICAL PAPERS-SOCIETY OF MANUFACTURING ENGINEERS-ALL SERIES-

87. Özel T, Liu X, Dhanorker A (2007) Modelling and simulation of micro-milling process. In: 4th International Conference and Exhibition on Design and Production of Machines and Dies/Molds. pp 21–23

88. Jin X, Altintas Y (2011) Slip-line field model of micro-cutting process with round tool edge effect. Journal of Materials Processing Technology 211:339–355

89. Balaji AK, Ghosh R, Fang XD, et al (2006) Performance-based predictive models and optimization methods for turning operations and applications: part 2—assessment of chip forms/chip breakability. Journal of manufacturing Processes 8:144–158

90. Spaans C (1971) The fundamentals of three-dimensional chip curl, chip breaking and chip control

91. Nakayama K, Ogawa M (1978) Basic Rules on the Form of Chip Metal Cutting.

CIRP Ann 27:17

92. Kharkevich A, Venuvinod PK (1999) Basic geometric analysis of 3-D chip forms in metal cutting.: Part 1: determining up-curl and side-curl radii. International Journal of Machine Tools and Manufacture 39:751–769

93. Ghosh R, Dillon Jr OW, Jawahir IS (1998) An investigation of 3-D curled chip in machining-Part 1: A mechanics-based analytical model. Machining Science and Technology 2:91–116

94. Fang XD, Fang YJ, Hamidnia S (1997) Computer Animation of 3-D Chip Formation in Oblique Machining. J Manuf Sci Eng 119:433–438. https://doi.org/10.1115/1.2831124

95. Nakayama K, Arai M (1992) Comprehensive chip form classification based on the cutting mechanism. CIRP Annals-Manufacturing Technology 41:71–74

96. de Oliveira FB, Rodrigues AR, Coelho RT, de Souza AF (2015) Size effect and minimum chip thickness in micromilling. International Journal of Machine Tools and Manufacture 89:39–54

97. Davoudinejad A, Parenti P, Annoni M (2017) 3D finite element prediction of chip flow, burr formation, and cutting forces in micro end-milling of aluminum 6061-T6. Frontiers of Mechanical Engineering 1–12

98. Davim JP (2017) Microfabrication and Precision Engineering: Research and Development. Woodhead Publishing

99. Vogler MP, DeVor RE, Kapoor SG (2003) Microstructure-Level Force Prediction Model for Micro-milling of Multi-Phase Materials. J Manuf Sci Eng 125:202–209. https://doi.org/10.1115/1.1556402

100. Tobias SA, Fishwick W (1958) Theory of regenerative machine tool chatter. The engineer 205:199–203

101. TLUSTY J (1963) The Stability of Machine Tools against Self-Excited Vibrations in Machining. International Research in Production Engineering

102. Merritt HE (1965) Theory of self-excited machine-tool chatter: contribution to machine-tool chatter research—. Journal of engineering for industry 87:447–454

103. Sridhar R, Hohn RE, Long GW (1968) A general formulation of the milling process equation: contribution to machine tool chatter research—5. Journal of Engineering for Industry 90:317–324

104. Sridhar R, Hohn RE, Long GW (1968) A stability algorithm for the general milling process: contribution to machine tool chatter research—7. Journal of Engineering for Industry 90:330–334

105. Hanna NH, Tobias SA (1974) A Theory of Nonlinear Regenerative Chatter. J

Eng Ind 96:247–255. https://doi.org/10.1115/1.3438305

106. Opitz H (1979) Investigation and Calculation of the Chatter Behavior of: Lathes and Milling Machines. Annals of the CIRP 18:335–342

107. Tlusty J, Ismail F (1981) Basic Non-Linearity in Machining Chatter. CIRP Annals 30:299–304. https://doi.org/10.1016/S0007-8506(07)60946-9

108. Tlusty J, Ismail F (1983) Special Aspects of Chatter in Milling. J Vib, Acoust, Stress, and Reliab 105:24–32. https://doi.org/10.1115/1.3269061

109. Tlusty J (1986) Dynamics of high-speed milling. Journal of Engineering for Industry 108:59–67

110. Minis I, Yanushevsky R, Tembo A, Hocken R (1990) Analysis of linear and nonlinear chatter in milling. CIRP Annals-Manufacturing Technology 39:459–462

111. Minis I, Yanushevsky R (1993) A new theoretical approach for the prediction of machine tool chatter in milling. Journal of Engineering for Industry 115:1–8

112. Altintaş Y, Budak E (1995) Analytical prediction of stability lobes in milling. CIRP Annals-Manufacturing Technology 44:357–362

113. Budak E, Altintas Y (1998) Analytical prediction of chatter stability in milling—part I: general formulation. Journal of Dynamic Systems, Measurement, and Control 120:22–30

114. Budak E, Altintas Y (1998) Analytical prediction of chatter stability in milling—part II: application of the general formulation to common milling systems. Journal of Dynamic Systems, Measurement, and Control 120:31–36

115. Altintas Y (2001) Analytical prediction of three dimensional chatter stability in milling. JSME International Journal Series C Mechanical Systems, Machine Elements and Manufacturing 44:717–723

116. Bayly PV, Mann BP, Schmitz TL, et al (2002) Effects of radial immersion and cutting direction on chatter instability in end-milling. In: ASME 2002 international mechanical engineering congress and exposition. American Society of Mechanical Engineers, pp 351–363

117. Faassen RPH, Van de Wouw N, Oosterling JAJ, Nijmeijer H (2003) Prediction of regenerative chatter by modelling and analysis of high-speed milling. International Journal of Machine Tools and Manufacture 43:1437–1446

118. Altintas Y, Stepan G, Merdol D, Dombovari Z (2008) Chatter stability of milling in frequency and discrete time domain. CIRP Journal of Manufacturing Science and Technology 1:35–44

119. Filiz S, Ozdoganlar OB (2008) Microendmill Dynamics Including the Actual

Fluted Geometry and Setup Errors—Part I: Model Development and Numerical Solution. J Manuf Sci Eng 130:031119-031119–10. https://doi.org/10.1115/1.2917321

120. Filiz S, Ozdoganlar OB (2008) Microendmill Dynamics Including the Actual Fluted Geometry and Setup Errors—Part II: Model Validation and Application. J Manuf Sci Eng 130:031120. https://doi.org/10.1115/1.2936379

121. Malekian M, Park SS, Jun MB (2009) Modeling of dynamic micro-milling cutting forces. International Journal of Machine Tools and Manufacture 49:586–598

122. Park SS, Rahnama R (2010) Robust chatter stability in micro-milling operations. CIRP Annals-Manufacturing Technology 59:391–394

123. Afazov SM, Ratchev SM, Segal J, Popov AA (2012) Chatter modelling in micro-milling by considering process nonlinearities. International Journal of Machine Tools and Manufacture 56:28–38

124. Jin X, Altintas Y (2013) Chatter stability model of micro-milling with process damping. Journal of manufacturing science and engineering 135:031011

125. Zhongqun L, Qiang L (2008) Solution and Analysis of Chatter Stability for End Milling in the Time-domain. Chinese Journal of Aeronautics 21:169–178. https://doi.org/10.1016/S1000-9361(08)60022-9

126. Mayor JR, Sodemann AA (2008) Intelligent tool-path segmentation for improved stability and reduced machining time in micromilling. Journal of manufacturing science and engineering 130:031121

127. Ziegert JC, Pathak JP, Jokiel B (2003) An Ultra-high Speed Spindle for Micro-milling. In: Proc. of ASPE. Portland, Oregon

128. Borisavljevic A, Kimman MH, Tsigkourakos P, et al (2009) Motor drive for a novel high-speed micro-milling spindle. In: Advanced Intelligent Mechatronics, 2009. AIM 2009. IEEE/ASME International Conference on. IEEE, pp 1492–1497

129. Lee J-H, Sodemann AA (2018) Digital Image Processing for Counting Chips in Micro-End-Milling. In: 2018 International Conference on Vision, Image and Signal Processing (ICVISP)

130. Singh KK, Kartik V, Singh R (2015) Modeling dynamic stability in high-speed micromilling of Ti–6Al–4V via velocity and chip load dependent cutting coefficients. International Journal of Machine Tools and Manufacture 96:56–66

131. Mauricio CR, Schneider FK, dos Santos LC (2010) Image-based red cell counting for wild animals blood. In: Engineering in Medicine and Biology Society (EMBC), 2010 Annual International Conference of the IEEE. IEEE, pp

438–441

132. Toh YH, Ng TM, Liew BK (2009) Automated fish counting using image processing. In: Computational Intelligence and Software Engineering, 2009. CiSE 2009. International Conference on. IEEE, pp 1–5

133. Otsu N (1979) A threshold selection method from gray-level histograms. IEEE transactions on systems, man, and cybernetics 9:62–66

134. Bradley D, Roth G (2007) Adaptive thresholding using the integral image. Journal of Graphics Tools 12:13–21

135. The Mathworks (Matlab R2016b) Morphological operations on binary images. https://www.mathworks.com/help/images/ref/bwmorph.html

136. The Mathworks (Matlab R2016b) Convert RGB image or colormap to grayscale. https://www.mathworks.com/help/matlab/ref/rgb2gray.html

137. The Mathworks (Matlab R2016b) Find connected components in binary image. https://www.mathworks.com/help/images/ref/bwconncomp.html

138. The Mathworks (Matlab R2016b) Adaptive image threshold using local first-order statistics. https://www.mathworks.com/help/images/ref/adaptthresh.html

139. Lee J-H, Sodemann AA, Bajaj AK Experimental Validation of Chip Production Rate as a Tool Wear Identification in Micro-EndMilling. Int J Adv Manuf Technology[Minor revision in-process]

140. Lee J-H, Sodemann AA (2018) Digital Image Processing for Counting Chips in Micro-End-Milling. In: Proceedings of the 2nd International Conference on Vision, Image and Signal Processing. ACM, p 9

141. Altintas Y (2012) Manufacturing automation: metal cutting mechanics, machine tool vibrations, and CNC design. Cambridge university press

142. Yuan ZJ, Zhou M, Dong S (1996) Effect of diamond tool sharpness on minimum cutting thickness and cutting surface integrity in ultraprecision machining. Journal of Materials Processing Technology 62:327–330

143. Graham E, Mehrpouya M, Nagamune R, Park SS (2014) Robust prediction of chatter stability in micro milling comparing edge theorem and LMI. CIRP Journal of Manufacturing Science and Technology 7:29–39. https://doi.org/10.1016/j.cirpj.2013.09.002

144. Cao Z, Li H (2015) Investigation of machining stability in micro milling considering the parameter uncertainty. Advances in Mechanical Engineering 7:1687814015575982. https://doi.org/10.1177/1687814015575982

145. Xuewei Z, Tianbiao Y, Wanshan W (2016) Chatter stability of micro end milling by considering process nonlinearities and process damping. International Journal

of Advanced Manufacturing Technology 87:2785–2796. https://doi.org/10.1007/s00170-016-8658-5

146. Tomasi C, Kanade T (1991) Detection and Tracking of Point Features. Computer Science Department, Carnegie Mellon University

147. Shi J, Tomasi C (1994) Good features to track. In: 1994 Proceedings of IEEE Conference on Computer Vision and Pattern Recognition. pp 593–600

148. Delio T, Tlusty J, Smith S (1992) Use of audio signals for chatter detection and control. Journal of engineering for industry 114:146–157

149. Lee HU, Cho D-W, Ehmann KF (2008) A Mechanistic Model of Cutting Forces in Micro-End-Milling With Cutting-Condition-Independent Cutting Force Coefficients. J Manuf Sci Eng 130:031102-031102–9. https://doi.org/10.1115/1.2917300

150. Jin X, Altintas Y (2012) Prediction of micro-milling forces with finite element method. Journal of Materials Processing Technology 212:542–552. https://doi.org/10.1016/j.jmatprotec.2011.05.020

151. Oliaei SNB, Karpat Y (2016) Influence of tool wear on machining forces and tool deflections during micro milling. The International Journal of Advanced Manufacturing Technology 84:1963–1980

152. Özel T, Thepsonthi T, Ulutan D, Kaftanoğlu B (2011) Experiments and finite element simulations on micro-milling of Ti–6Al–4V alloy with uncoated and cBN coated micro-tools. CIRP Annals-Manufacturing Technology 60:85–88

153. Zhang X, Yu T, Wang W (2018) Prediction of cutting forces and instantaneous tool deflection in micro end milling by considering tool run-out. International Journal of Mechanical Sciences 136:124–133

169

APPENDIX A

INSTRUCTION FOR CALIBRATION OF CUTTING EDGE WEAR ESTIMATOR

Following instruction explains how and when the calibration should be done in practice.

- Device setup

  ① Chip collecting part

  - Check the variance of the number of chips in the same cutting condition. (C.O.V<10%)

  - If the variance is large, check the chip suction part or the chip blowing part.

  ② Chip counting part

  - Check the images to make sure the focus of USB microscope is at the center of the tape.

  - Check the image processing to make sure the images are not blurry.

  ③ Tape collecting part

  - Tape speed should be constant.

  - Tape must keep a same distance from the exhaust nozzle of the air pump.

- Calibration process

  ① Select a micro-endmill and measure the cutting edge radius using a high performance microscope.

  ② Run the chip production simulation. Use the measured cutting edge radius data in the simulation. Find the optimum size filtering value for the simulation.

  ③ Depth of cut and spindle speed must be selected from the stable cutting condition.

④ Before starting the cutting operation, select the resolution of the cutting edge wear estimator. Ex) 0.5mm/s, 1mm/s

⑤ If the resolution is 1mm/s, then cut 6 slots with 6 different feedrates from 1 to 6 mm/s with 1 mm/s increment at each slot while collecting and counting the chips. If the resolution is 0.5 mm/s, then cut 12 slots with 12 different feedrates from 1 to 6 mm/s with 0.5 mm/s increment at each slot.

⑥ Conduct the linear fitting between the simulation and the experimental results.

⑦ Find the optimum size filtering values for the experiment by sweeping the experimental size filtering values from 0 to a certain value which gives zero r-square value from the linear fitting.

⑧ Find the optimum drop detection threshold which gives a maximum probability of correct estimation by sweeping the drop detection threshold from 0 to 50 %.

- The calibration must be conducted everytime the device setup has been changed.